MARCHENKO IMAGING FOR 2D AND 3D COMPLEX STRUCTURES —WITH FIELD APPLICATIONS TO SUB-SALT AND SUB-BASALT IMAGING

by

Xueyi (Alex) Jia

A thesis submitted to the Faculty and the Board of Trustees of the Colorado School of Mines in partial fulfillment of the requirements for the degree of Doctor of Philosophy (Geophysics).

Golden, Colorado

Date _____

Signed: _____
Xueyi (Alex) Jia

Signed: _____
Dr. Roel Snieder
Thesis Advisor

Golden, Colorado

Date _____

Signed: _____
Dr. Paul Sava
Professor and Head
Department of Geophysics

ABSTRACT

Seismic imaging is a geophysical technique that uses elastic waves to form images of geologic formations in the subsurface. Seismic imaging has become the most reliable diagnostic tool for modern hydrocarbon exploration and production. Conventional imaging methods, however, rely on the single-scattering assumption, which requires the recorded seismic data to not include multiples—waves that are reflected more than once in the subsurface before reaching the receivers. While the surface related multiples can be effectively suppressed with the Surface Related Multiples Elimination (SRME) method, the elimination of the internal multiples multiples that are not surface related—remains challenging with current seismic processing techniques. The traditional workflow to mitigate the artifacts associated with internal multiples involves 1) predicting internal multiples, and 2) subtracting them from the acquired seismic data. This workflow requires accurate horizons of the multiple generators and a labor-intensive adaptive subtraction, which is usually performed in a least-squares sense and may damage primary events when primaries and multiples interfere. The Marchenko framework used in this dissertation is based on inverse problems in quantum physics. This framework consists of two steps. The first step is *Marchenko redatuming*, which allows one to use surface seismic reflection data to retrieve seismic responses (Green's functions) between arbitrary points in the subsurface to the acquisition surface. The second step is *Marchenko imaging*, which utilizes the Green's functions retrieved by Marchenko redatuming for imaging. These two steps provide a solution for resolving the issues associated with internal multiples and producing multiple-free images, without requiring horizons of multiple generators or performing adaptive subtraction.

For my PhD research, I develop and investigate the 2D and 3D Marchenko framework for field data deployment and application. I elucidate the specific requirements for the two inputs of the Marchenko method: the seismic reflection data acquired on the earth surface

and a background velocity model for estimating first arrivals from subsurface locations to the surface. To make the standard surface seismic data (which can be sparsely sampled in practice) useful for Marchenko redatuming, I consider forward interpolation methods to convert sparse surface data to densely and uniformly sampled data that corresponds to an equal number of co-located sources and receivers at the acquisition surface. I show that the background velocity model does not need to be known in great detail since the first-arriving wave needed by the Marchenko method is mostly determined by its travel time. A smooth velocity model is sufficiently accurate for such estimations. I demonstrate that the combination of Marchenko redatuming and imaging is robust with respect to erroneous velocity models. I extend the Marchenko redatuming algorithm to 3D seismic data by reformulating the Marchenko-type equations in 3D Cartesian coordinate system and develop an efficient 3D numerical implementation, in which I resolve the associated computational optimization and memory issues. Despite the idealized assumptions and the specific requirements for the input data within the Marchenko framework, I obtained two successful field data applications of the Marchenko method for imaging complex subsurface areas and propose a practical and effective workflow for processing streamer field data. With a Gulf of Mexico field dataset, I show that discontinuities along true reflectors—resulting from the destructive interference between primaries and the internal multiples due to salt layers—is resolved by the Marchenko method, which produces a clean and continuous sub-salt image. With an offshore Brazil dataset, I show that the artificial or nonphysical interfaces—resulting from the internal multiples that are generated by volcanic intrusion layers in the overburden—are adequately eliminated by performing Marchenko imaging.

TABLE OF CONTENTS

LIST OF FIGURES

ACKNOWLEDGMENTS

Many years later, when he faced the committee at his PhD defense, Alex Jia was to remember that distant afternoon when his mother burst into tears as she saw him half-naked, purposely covering his face with his tank, not paying attention to his math teacher at all during the entire class. She made all the efforts to register him to that city's best kindergarten, which was one-hour biking from home everyday. My mother didn't have a clear idea what she wanted me to become, 25 years ago or today, but she is very clear that her son needs to be educated and she does everything she can to make sure I get the best educational resources. By comparison, as the first person ever to earn a Master's degree from his village, my father is pretty chill when it comes to education. My father urges his son to become a man of integrity, accountability and kindness. I ended up getting my Bachelor's degree in Physics from the best university in China, Peking University, and obtaining my PhD from a world-class research group for exploration geophysics, the Center for Wave Phenomena (CWP) at the Colorado School of Mines. It's considered wired in Chinese culture to thank one's parents, but I am only writing this PhD dissertation today because of the love, dedication, and support that my father and mother give to me.

Laozi, one of the most influential ancient Chinese philosophers, said it best, *"A leader is best when people barely know he exists, when his work is done, his aim fulfilled, they will say: we did it ourselves."* My PhD advisor, Dr. Roel Snieder is such a leader, who leads with tremendous patience and encourages with genuine compliments. At our first meeting, which was an interview for my PhD admission, Roel printed out the offer letter for me right away, so as to not keep me hanging, waiting for his decision. Since then, Roel has been more than a research advisor to me. Throughout the 4.5 years of my PhD, we have met individually for approximated 135 hours (one hour per week), chatting, 85% about research, 14% about past, future, life, family and love. Born in the same year as my father, Roel

became my "crazy uncle" and my away-from-home dad, showing me by examples how to do research, how to work with other people, and how to cope with the things that happen to and around us. He has only given up on me on one thing—telling jokes. He tried all of his jokes, even his funniest ones—the inappropriate ones on me, only to receive my "ET" face, until he eventually admitted his failure. While playing the roles of a pacer and a cheerleader for my PhD journey, Roel is also literally the pace-setter and leader at what we call the Mines running club. He is so passionate about running that he has been urging me to join the Wednesday running since day one. It took me three and half years to finally make up my mind and run with him, in the Spring of 2019—the lowest point of my adult life. It was so difficult to just keep up with these serious folks at Roel's running club at the beginning. But it did get easier every time. In that four month span, we covered a total of 75 miles. I lost 20 pounds, getting sixpacks of abs, and "running" out of that "local minimum" of my life eventually. I love working with Roel and I am sad to see it come to an end. But one thing I know for sure is that the "crazy uncle" will be always there for me "as a friend, a colleague and a adviser (not advisor)", to quote Nori Nataka, a former stduent of Roel.

"*If you are the smartest person in the room, then you are in the wrong room*, Confucius." I am happy to have had the opportunity to work with so many outstanding people in the field of exploration geophysics, being in the "right" room. I thank Paul Sava for teaching me Reverse Time Migration and Madagascar. I thank Ilya Tsvankin for teaching me Seismology I, II and III. Seismology II was one of my favorite courses and I enjoy the Ilya's sense of humor. I thank Jeffery Sharrage for bring new energy to CWP and being an inspiration to me with his book—*The spoke and wheel*. I thank Diane for being there for me, supporting and encouraging me. I thank Ken Larner for continuing coming back from his beautiful retirement life and helping me and other CWPers with our presentation skills. I thank Michelle, Pam, Shingo for making my life much easier logistically. I thank all my CWP peers for their excellence and outstanding achievements, which push me to be as good as them. I sincerely thank my committee members, Michael Wakin, Paul Martin, Yaoguo

Li, Paul Sava, and my advisor Roel Snieder for their constructive questions and insightful comments at my three comprehensive exams.

I thank the CWP sponsors for their financial support and their representatives for the constructive feedback on my research. I feel privileged to have had the chance to share my work with such brilliant scientists. I appreciate the great opportunities for internships provided by the sponsors companies of CWP. I thank Guoping Chang, Jon Sheiman, John Kimbro, Ken Matson, Xuefeng Shang for their support during my internship at Shell. I thank James Zhang, Yang Zhao and Hyoungsu Baek for their mentorship during my internship at Aramco. I thank Anatoly Baumstein, Eric Neumann, Rongrong Lu, Charlie Jing, Junzhe Sun for their guidance during my internship at ExxonMobil. I sincerely thank Jeremy Zimmerman and Yang Luo from Chevron, Yu Zhang from ConocoPhillips, Antoine Guitton, Paul Williamson, Huimin Guan from Total, and Mingqiu Luo from Sinopec for being interested in my research and providing opportunities for my career. Through the interactions with these outstanding geoscientists from the petroleum industry, I was able to get exposure to real world problems and eventually compete my PhD thesis, at the heart of which is applications with real seismic data.

Last but not least, I would like to acknowledge my family and friends. I thank Cong Cao, Ye Gao, Chunjia Liu, Ning Wang, Zixiao Guo, Yonglin Han for being my loyal friends since we were kids and showing continuous care to me across continents. I thank all the friends I made in the US, my basketball teammates, lunch buddies and clubbing junkies (won't mention the names, but you know who you are). I thank my head teachers, Qingshi Shao, Jingyi Fei, Chunxia Liu for having faith in me since elementary school and elevating me to someone more than I thought I could be. Finally, I want to thank all the remarkable alumni from Peking University for pioneering the road and showing me what it means to become pillars of the society.

To my parents

致我的父亲母亲

CHAPTER 1

GENERAL INTRODUCTION

Internal multiples pose one of the important yet unsolved problems in modern seismic processing and imaging. If not correctly handled, internal multiples contaminate the seismic images that are utilized in the geologic interpretation for subsurface hydrocarbon exploration and production.

Conventional seismic methods for imaging the earth's interior, such as Ray-based migration (e.g Kirchhoff migration): Beylkin (1985); Bleistein *et al.* (2001); Bleistein (1987); French (1975); Operto *et al.* (2000); Schneider (1978), one-way wave equation migration: Claerbout (1971); Hale (1991); Zhang *et al.* (2005), and two-way wave equation migration (Reverse Time Migration): Baysal *et al.* (1983); McMechan (1983); Whitmore (1983), rely on the single-scattering assumption, which means these methods require that the recorded seismic data do not include waves that are reflected more than once in the subsurface before reaching the receivers (for overviews of the conventional migration methods: Etgen *et al.* (2009); Sava & Hill (2009)). Geophysicists consider that the single-scattering assumption is valid for the majority of the seismic data. Yet, multiples - the waves that are reflected more than once in the subsurface—usually are present in seismic data. The elimination of one specific type of multiples, the surface related multiples—the waves that are reflected downwards only by the earth surface and are reflected twice or more inside the earth (blue dashed line in Figure 1.1(a))—can be resolved with 2D and 3D Surface Related Multiple Elimination (SRME) (Berkhout & Verschuur, 1997; Dragoset *et al.*, 2010; Matson & Abma, 2005; Verschuur, 1991). But internal multiples—the multiples that are not surface related (red dashed line in Figure 1.1(a))—remain a challenge with current seismic processing techniques.

Strong internal multiples can be generated in a variety of subsurface environments. Particularly, for marine seismic surveys, the water bottom or seabed is one of the strongest

interbed multiple generators due to the high velocity and density contrast between water and sediments. Generally, multiple-generating interfaces can be any interface with strong acoustic impedance, such as salt bodies, carbonates, volcanic intrusions, gas layers, etc. Part of the reason why the attenuation of the internal multiples is challenging is due to the complexity (structural shapes and various impedance along the interfaces) of the internal multiples generators and the similar behaviour of internal multiples and primaries in the seismic records. Conventional imaging methods (e.g. Reverse Time Migration, Kirchhoff migration) treat all input seismic events as primary reflections (black solid line in Figure 1.1(a)). If strong internal multiples exist, but are not properly handled, conventional methods map the internal multiples to a greater depth beneath strong multiple generators. Meanwhile, because the large impedance difference between the multiple generators and the surrounding sediments, hydrocarbons also tend to be trapped beneath the multiple generators. Therefore the internal multiples are often imaged onto the reservoir layers by the conventional methods, misleading the geologic interpretation for subsurface structure, lithology and fabric. This is illustrated in Figure 1.1(b) where an artificial structure (enclosed by red dashed line) resulting from internal multiples, interferes with a deeper hydrocarbon reservoir and contaminates the seismic image. Hence, a robust and effective method for handling the internal multiples is highly desired for for hydrocarbon exploration.

The traditional workflow to mitigate the artifacts associated with internal multiples involves, 1) predicting internal multiples, and 2) subtracting them from the acquired seismic data. Berkhout & Verschuur (1997) proposed an algorithm to remove internal multiples, which requires knowledge of the smooth velocity model between the surface and the upper boundary of the multiple generating layer. Jakubowicz (1998) developed an explicit internal multiple prediction method involving a two-trace convolution followed by a single-trace correlation. Current industrial internal multiple prediction tools are mostly based on this idea. These tools require accurate picking of subsurface horizons (either by geophysicists or automated computer algorithms) and inevitably rely upon an adaptive subtraction technique

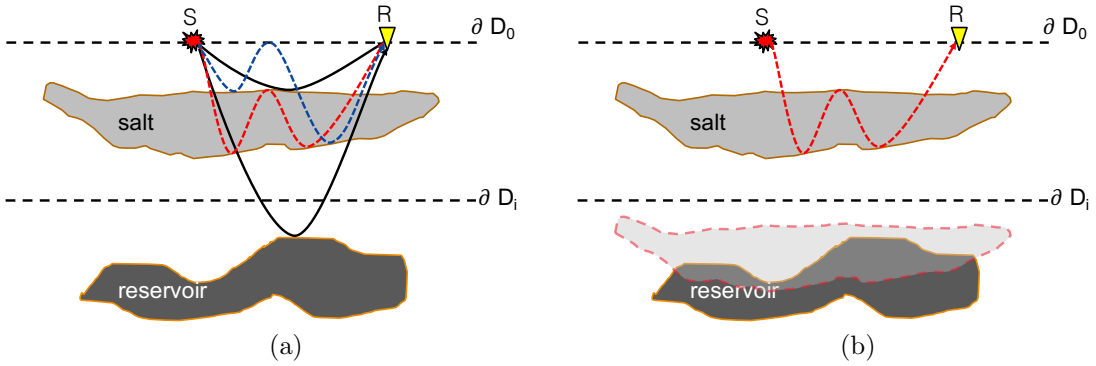

Figure 1.1: (a) Primary reflections (solid black lines), surface related multiples (blue dashed line), and internal multiples (red dashed line). (b) An artificial structure (enclosed by red dashed line) resulting from internal multiples by conventional seismic imaging, that interferes with a deeper hydrocarbon reservoir and contaminates the seismic image.

to mute the internal multiples from the seismic data. Both horizon picking and adaptive subtraction need human intervention and can be labor-intensive. Horizon picking suffers if the velocity model is not accurate. Adaptive subtraction, which is usually performed in a least-squares sense, may damage primary events at the location where primaries and multiples interfere.

Issues related to internal multiples can be potentially resolved with the Marchenko method, a novel technique for producing multiple-free seismic images using the surface seismic data and a background velocity model (Broggini *et al.*, 2012, 2014b; Wapenaar *et al.*, 2014b). It provides target-oriented images specifically for areas with complex structures that generate strong internal multiples. I outline the development of the Marchenko framework below.

Rose (2001) raised a simple yet interesting question: can one find an incident wave from one side of the medium such that the wavefield focuses at a pre-defined location and time, without knowing the detailed properties of the medium? He sought for the equation that determines such a focusing incident wave, and found that the equation he looked for was the Marchenko equation. Marchenko (1955) derived the equation of 1D inverse-scattering, which reconstructs the properties of the medium from reflected waves for several wave equations

(such as time-dependent Schrödinger equation and the plasma wave equation). Rose (2001) later showed that the Marchenko equation also leads to incident wavefields that focus at a specified point in an unkown medium. Hence, Marchenko is credited and a newly developed framework, which aims to retrieve the impulse response to a virtual source at a pre-defined location inside a medium, is named after him. This framework was first formulated by Broggini *et al.* (2012) for seismic applications, who demonstrated the Marchenko autofocusing method using the single-sided reflection response of a one-dimensional (1D) medium, and they showed that the focusing principles outlined by Rose (2001) could be extended to retrieve the Green's function for the unknown medium as well. Based on a decomposition of the wavefield into upgoing and downgoing waves, Wapenaar *et al.* (2014b) generalized the theory of Marchenko redatuming/Green's function retrieval to 2D and 3D, and proposed the framework to eventually produce a seismic image based on the up/down decomposition of the retrieved Green's functions. The retrieved Green's function is proven to accurately contain both primaries and multiples that propagate in the medium. Therefore, unlike conventional imaging approaches which are meaningful only for the primaries, Marchenko imaging provides an alternative approach for creating a seismic image which takes the internal multiples into account. More specifically, the artifacts caused by internal multiples can be eliminated in the seismic image produced by Marchenko imaging.

The Marchenko framework has since developed rapidly in various directions. The theory has been extended to elastic data for Marchenko redatuming and imaging (da Costa Filho *et al.*, 2014, 2015; Wapenaar, 2014) and free surface multiples have been incorporated within the Marchenko framework (Singh *et al.*, 2015a, 2016a). Dukalski & de Vos (2017) presented two alternative methods to solve the Marchenko equations with free surface multiples taken into account: LSQR (least squares) and a modified Levinson-type algorithm. To make the method model-free, Zhang & Staring (2018) proposed a modified data-driven Marchenko algorithm. Ravasi (2017) and Slob & Wapenaar (2017) proposed an approach to use dual-sensor data (e.g. pressure and vertical particle velocity) to solve the coupled

Marchenko equations that can handle band-limited seismic data with an unknown wavelet from a more flexible acquisition system—arbitrarily located sources above a line of regularly sampled receivers. Besides imaging, applications such as internal multiples prediction and removal, source wavelet estimation, time-lapse monitoring have been developed based on the Marchenko framework (Meles *et al.*, 2014; Mildner *et al.*, 2017; Wapenaar & Slob, 2017). Marchenko imaging has been successfully applied to several field datasets. Ravasi *et al.* (2016) applied Marchenko imaging to an ocean-bottom cable survey recorded over the Volve North Sea field. Staring *et al.* (2017) show an adaptive double-focusing Marchenko imaging with a Santos Basin field dataset. Jia *et al.* (2018) demonstrated a practical work flow to perform Marchenko imaging with marine streamer data for sub-salt imaging and showed that sub-salt image produced with the Marchenko method was cleaner and more continuous compared to the RTM image using a Gulf of Mexico field dataset. Krueger *et al.* (2018) presented their internal multiple attenuation workflow based on Marchenko internal multiple prediction and adaptive subtraction for four pre-salt fields in the Santos Basin, Brazil.

1.1 Thesis overview

The objective of this thesis is to make the Marchenko framework applicable to 2D and 3D field seismic data for producing multiple-free subsurface images.

In **Chapter 2**, I apply the Marchenko method to a Gulf of Mexico field dataset to resolve challenging sub-salt imaging problems. I purpose a practical work flow for processing marine streamer field data, and present a complete theoretical and practical framework to produce a target-oriented sub-salt image using the Marchenko method. I show the first successful field data application that exploits Marchenko imaging to eliminate the artifacts associated with internal multiples beneath salt bodies. While being consistent and comparable with the RTM image, Marchenko imaging achieves improvements in the smoothness and continuity of the imaged geological structures. In this field data example, internal multiples corrupt seismic images producing false negatives by destructively interfering with primaries. Later in **Chapter 5**, with an offshore Brazil field dataset, I demonstrate that the false positives

(focusing energy at nonphysical interfaces) associated with internal multiples can also be eliminated by the Marchenko method.

In **Chapters 3**, I investigate the specific requirements for the two inputs of the Marchenko algorithm: the surface seismic data and the background velocity model. I summarize the idealised scenario for which the required surface seismic data should be acquired. Since the field data acquisition rarely meets these requirements, data regularization, a process of putting the irregular and sparse data to a uniform and dense grid, needs to be performed. I investigate four forward interpolation methods for both 2D and 3D data regularization. The investigated interpolation methods are used in **Chapter 4** for the data regularization of 3D streamer type data. For the other input—the velocity model—I clarify that the background velocity model does not need to be detailed as it is merely used to estimate the first arriving waves, hence it only needs to be sufficiently accurate to predict the arrival time of the direct wave from the imaging point to the surface. With two synthetic examples and an offshore Brazil field data example, I show that the combination of Marchenko redatuming and imaging is robust with respect to erroneous velocity models.

In **Chapter 4**, I extend the Marchenko redatuming algorithm for seismic data in three dimensions. I reformulate the Marchenko equations in a three dimensional Cartesian coordinate system. I propose an approach to efficiently determine the aperture and the spatial sampling of the source/receiver pairs required for surface seismic surveys by 3D Marchenko redatuming. I validate the 3D Marchenko redatuming algorithm with a 3D trapezoidal and dipping model and a 2.5D Gulf of Mexico model. I also test the B-spline interpolation for resolving the sparsity of the cross-line spatial sampling for 3D streamer data with the 2.5D Gulf of Mexico model. I discuss the computational optimization I use for the 3D Marchenko algorithm for saving memory and CPU time and formulate a comparison between the surface-related multiple elimination (SRME) method and the Marchenko method.

In **Chapter 5**, I address another challenging scenario in which internal multiples generate artifacts in seismic images—sub-basalt imaging. Sub-basalt imaging for hydrocarbon explo-

ration is challenging because of multiple scattering, attenuation and mode-conversion when seismic waves encounter highly heterogeneous and rugose basalt layers (Ziolkowski *et al.*, 2003). With an offshore Brazil dataset, I demonstrate the capability of the Marchenko method for sub-basalt imaging. I show that the internal multiples, which are generated by the seabed and basalt layers and create significant nonphysical interfaces in the conventional image, are clearly eliminated by Marchenko imaging.

In **Chapter 6**, I present the general conclusions and final remarks of this dissertation and make recommendations for future research along the path of the field data deployment of the Marchenko framework.

CHAPTER 2

A PRACTICAL IMPLEMENTATION OF SUBSALT MARCHENKO IMAGING WITH A GULF OF MEXICO DATASET

Xueyi (Alex) Jia[1], Antoine Guitton[2], and Roel K. Snieder[1]

Published in *Geophysics*[3] .

2.1 Abstract

Marchenko redatuming allows one to use surface seismic reflection data to generate the seismic response from sources at the surface to any point in the subsurface. Without requiring much information about the earth's properties, the seismic response generated by Marchenko redatuming contains accurate estimates of not only the primaries, but also internal multiples. A target- oriented imaging method, referred to as Marchenko imaging, was implemented for imaging complex structures of the earth using the seismic response obtained through Marchenko redatuming. Taking account of the contribution of both primaries and internal multiples, Marchenko imaging produce images that contains less artifacts than the images obtained using conventional imaging methods (e.g. Reverse Time Migration) with the same input data. In this study, we applied Marchenko imaging to a field dataset acquired at the Gulf of Mexico to produce an image of a subsalt area. We investigated two important and practical aspects of the Marchenko framework: 1) the missing near offsets in marine shot records, and 2) the calibration of the reflection data. Finally, we suggested a work flow for processing the marine towed-streamer field dataset acquired at the Gulf of Mexico, and presented a complete theoretical and practical framework to produce a target-oriented subsalt image using the Marchenko methods. The images obtained from Marchenko

[1]Center for Wave Phenomena, Colorado School of Mines, 1500 Illinois St., Golden, CO 80401, USA
[2]Total CSTJF, EC465, AvenueLarribau, Pau, 64018 PAU Cedex, France
[3]Reprinted with permission of Geophysics, Volume 83, Issue 5 (Sep 2018), S409-S419, https://doi.org/10.1190/geo2017-0646.1

imaging are consistent and comparable, for the most part, with conventional migration methods. However, Marchenko imaging achieves improvements in the continuity of the geological structures and in suppressing the artifacts which are caused by internal multiples.

2.2 Introduction

Marchenko imaging is a technique to image the subsurface of the earth using both the primaries and multiples of seismic data, and aims to produce an image that is free of artifacts caused by multiple reflections. This imaging approach is based on the redatumed reflection response created by a method referred to as Marchenko redatuming, which virtually moves the surface seismic sources and receivers to a deeper depth, close to the targets in the medium. Significantly, the redatumed data contain only the reflection response below the redatuming depth, and the medium above is treated as reflection-free. Therefore, Marchenko imaging provides a target-oriented solution specifically for imaging the area below complex structures such as salt bodies (which can create strong multiples).

Marchenko redatuming (the core of the Marchenko frame work) contains two steps: receiver redatuming and source redatuming (Figure 2.1). Receiver redatuming aims to retrieve wavefields from sources at the surface to a virtual receiver in the medium using Marchenko-type equations. Classic redatuming methods (Berryhill, 1979, 1984; Kinneging *et al.*, 1989) do not account for internal multiple reflections; hence, spurious events can emerge when there is only single-sided illumination (Snieder *et al.*, 2006). With Marchenko redatuming, both the primaries and the multiples can be correctly estimated (Broggini *et al.*, 2012; Rose, 2002; Wapenaar *et al.*, 2014b), and the retrieved wavefields are naturally separated into up- and downgoing components. In the second step of source redatuming, these up- and downgoing wavefields can be utilized to move the sources to the redatuming level by approaches such as multidimensional deconvolution (van der Neut *et al.*, 2011). Unlike the wavefield retrieval method that uses seismic interferometry, which requires the data recorded at a physical receiver in the subsurface (Bakulin & Calvert, 2006), Marchenko redatuming requires only surface seismic data and a background velocity model as inputs, which are the

same requirements for many standard imaging techniques (e.g. Reverse Time Migration). A background velocity model, instead of being used to perform any wavefield propagation, is used to compute the traveltime of the first arrival from a subsurface point to the surface, In general, the Marchenko redatuming process does not require any more details of the medium parameters than conventional imaging schemes (Broggini *et al.*, 2014b).

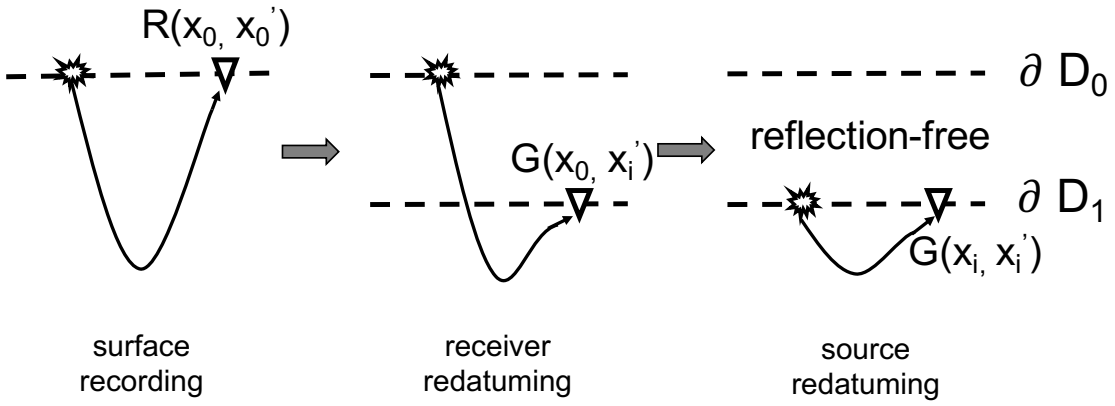

Figure 2.1: Illustration of the source and receiver levels for surface recording, after receiver redatuming and after source redatuming.

Broggini & Snieder (2012) first showed the scheme to use Marchenko equations to retrieve the Green's functions between an arbitrary virtual source position inside the 1D medium and a receiver at the surface with only the reflection response recorded at the surface of that medium. Wapenaar *et al.* (2014a,b) then derived the 3D Marchenko equations, which relate the single-sided reflection response of a 3D medium to a focusing wavefield, of which the focusing point is defined by estimating the traveltime from this point to the surface.

Marchenko redatuming has been extended to elastic media by using P- and S- wave measured potentials from P- and S- wave potential sources (Wapenaar, 2014) and by using velocity-stress recordings from force and deformation sources (da Costa Filho *et al.*, 2014). Based on the latter approach, an elastic Marchenko imaging method has been proposed (da Costa Filho *et al.*, 2015). All of the above redatuming methods are under the assumption that surface-related multiples are eliminated in the data. In order to bypass the need to

apply surface-related multiple elimination (SRME) to the data, Singh *et al.* (2015a) showed a method to directly handle the free surface multiples by adding an extra integral that represents the free surface effect in the Marchenko equations (Singh *et al.*, 2015a). Dukalski & de Vos (2017) showed that the convergence of algorithm proposed by Singh *et al.* (2015a) is not always guaranteed. They analytically derived the conditions where algorithm proposed by Singh *et al.* (2015a) diverges and presented two alternative methods to solve the Marchenko equation, LSQR (least squares) and a modified Levinson-type algorithm, which do not suffer from the divergence problems but require an increased computational cost. Provided dual-sensor (e.g. pressure and vertical particle velocity) data, Ravasi (2017) and Slob & Wapenaar (2017) proposed the methods to solve the couple Marchenko equations that can handle band-limited seismic date with an unknown wavelet from a more flexible acquisition system (arbitrarily located sources above a line of regularly sampled receivers), with free-surfaces multiples included. For field data applications, target-oriented Marchenko imaging has been applied to an ocean-bottom cable (OBC) survey recorded over the Volve North Sea field (Ravasi *et al.*, 2016), and an adaptive Marchenko imaging scheme has been applied to a marine streamer dataset (Staring *et al.*, 2017). The application to the Volve field dataset presents some encouraging results, as the image produced by Marchenko imaging is more continuous compared to a standard RTM image. Moreover, Marchenko imaging reveals some structural features that are not present in the surface RTM image.

In this paper, we will demonstrate a successful application of Marchenko redatuming and imaging to a marine streamer dataset acquired over a salt structure at the Gulf of Mexico. With a salt body, this dataset provides sufficient complexities to test the Marchenko redatuming and imaging methods. In a standard marine towed-streamer survey, the near-offset data cannot be recorded, and the data contain only one-sided offsets. Hence, we will first perform a set of synthetic experiments to investigate whether the data acquired with such geometry satisfy the requirement for the reflection response of Marchenko redatuming. Then we will present a work flow (starting from the processing of the raw field data) to produce a

subsalt Marchenko image. We will review all the steps in the working flow: processing the raw data, estimating the direct arrival, redatuming through Marchenko iteration scheme, and imaging using deconvolution imaging condition. Finally, we will analyze the subsalt Marchenko image and compare it to a standard RTM image created with the same input dataset, and discuss the improvements gained in the Marchenko image.

2.3 Methodology

In this section, we outline the methodology for the Marchenko framework, including receiver redatuming, source redatuming, and imaging. We focus on the implementation and physical interpretation of receiver redatuming, and briefly discuss the source redatuming and imaging algorithms used in our application. Readers who do not want the details of the mathematical derivations for receiver redatuming, can treat the Marchenko redatuming process as a black box. Given a background velocity model and the surface seismic reflection response, the black box accurately produces the seismic wavefield recorded at a pre-defined subsurface point (responding to the surface sources) with both primary and multiple reflections. In other words, the black box retrieves a virtual Vertical Seismic Profile (VSP) as if a virtual receiver was placed inside the medium, and recorded data due to sources at the surface. Moreover, the retrieved wavefield is decomposed into two components: the upgoing component, which contains the energy that is propagating upward when it arrives at the virtual receiver, and the downgoing component, which contains the energy that is propagating downward when it arrives at the virtual receiver.

2.3.1 Receiver redatuming

In this study, we use an iterative scheme for receiver redatuming which is adapted from the work of Broggini *et al.* (2014b) on the basis of the earlier theoretical Marchenko frameworks (Broggini *et al.*, 2012; Rose, 2002; Wapenaar *et al.*, 2014b). The heart of the Marchenko redatuming is the reciprocity theorem. The convolution- and correlation-type reciprocity theorems relate two wave states with different field, material, and source properties in het-

erogeneous media (de Hoop, 1988; Vasconcelos *et al.*, 2009; Wapenaar *et al.*, 2004). Source-receiver reciprocity, which states that the same waveform will be observed if the locations of the source and receiver are exchanged, is a special case of the reciprocity theorem.

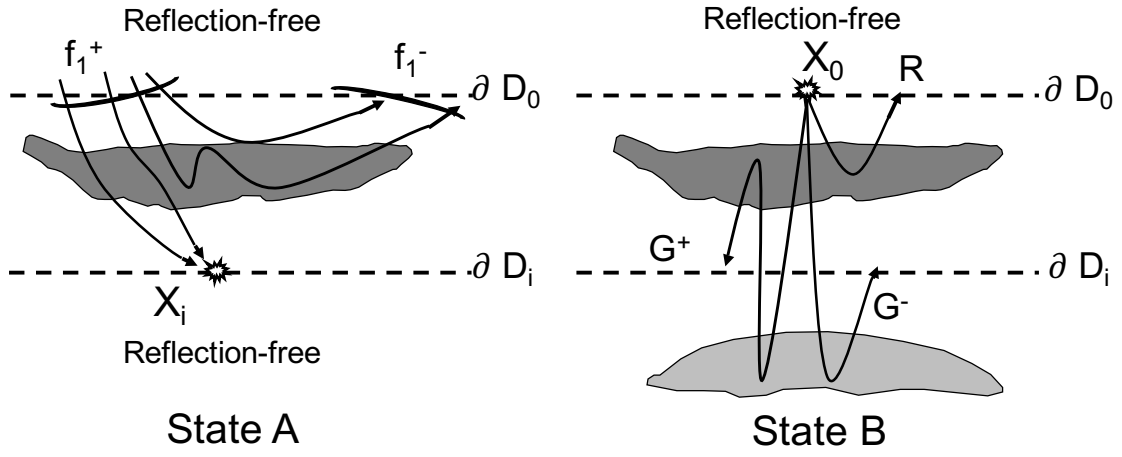

Figure 2.2: Illustration of the two wavefield states considered in Marchenko redatuming.

Figure 2.2 shows the two wave states we choose to relate by the reciprocity theorem in order to derive the Marchenko-type equations. State A is represented by the focusing functions (upgoing component f^- and downgoing component f^+) which are defined in a modified medium that is reflection-free below the focusing level ∂D_i. State B is represented by the actual wavefields in the subsurface (upgoing component G^- and downgoing component G^+). In the following discussion, we refer to these physical wavefields as the up- and downgoing Green's functions because the wavefields of state B represent the responses to impulsive point sources. In all our examples, the "Green's functions" shown in the figures are convolved with a Ricker wavelet (15 Hz) for display purposes.

According to the one-way reciprocity theorem, the Green's functions and the focusing functions are related by (van der Neut *et al.*, 2015a; Wapenaar *et al.*, 2014b)

$$G^-(x_i,x_0,\omega) = -f_1^-(x_0,x_i,\omega) + \int_{\partial D_0} R(x_0,x_0^{'},\omega) f_1^+(x_0^{'},x_i,\omega) dx_0^{'};$$
$$G^+(x_i,x_0,\omega) = [f_1^+(x_0,x_i,\omega)]^* - \int_{\partial D_0} R(x_0,x_0^{'},\omega)[f_1^-(x_0^{'},x_i,\omega)]^* dx_0^{'}. \tag{2.1}$$

Here $G^-(x_i,x_0,\omega)$ and $G^+(x_i,x_0,\omega)$ are the frequency-space domain up- and downgoing Green's functions, with a point source at x_0 at the acquisition surface and a receiver at x_i at a desired subsurface location. The focusing functions $f_1^-(x_0^{'},x_i,\omega)$ and $f_1^+(x_0^{'},x_i,\omega)$ are the up- and downgoing parts of the solution for a specified wave equation whose wavefield focuses at the subsurface location x_i. $R(x_0,x_0^{'},\omega)$ contain the earth's reflection response from a vertical dipole source at $x_0^{'}$ (recorded by a pressure receiver at x_0). The left multiplication is equivalent to convolution in the time-space domain, while * denotes complex conjugation.

We solve for $G^-(x_i,x_0,\omega)$ and $G^+(x_i,x_0,\omega)$ by decomposing equation 5.1 into two time windows: $t < t_d$ and $t > t_d$, where t_d is the direct arrival travel time from the focusing point x_i to the surface. In the time window when $t < t_d$, the Green's functions $G^+(x_0,x_i,\omega)$ and $G^-(x_0,x_i,\omega)$ are equal to zero. We first decompose f^+ into a direct wave T_d^{inv} and a following coda M^+:

$$f_1^+(x_0,x_i,\omega) = T_d^{inv}(x_0,x_i,\omega) + M^+(x_0,x_i,\omega), \tag{2.2}$$

and then substitute $f_1^+(x_0,x_i,\omega)$ in equation 5.1 with equation 5.2. Next, we compute the focusing functions by the following iterative scheme in the time window $t < t_d$:

$$\begin{aligned}
[M_k^+(x_0,x_i,\omega)]^* &= \int_{\partial D_0} R(x_0,x_0^{'},\omega)[f_{1,k}^-(x_0^{'},x_i,\omega)]^* dx_0^{'};\\
f_{1,k+1}^-(x_0,x_i,\omega) &= \int_{\partial D_0} R(x_0,x_0^{'},\omega) M_k^+(x_0^{'},x_i,\omega) dx_0^{'} + f_{1,0}^-(x_0,x_i,\omega),
\end{aligned} \tag{2.3}$$

with the initial value of f_1^- computed by

$$f_{1,0}^-(x_0,x_i,\omega) = \int_{\partial D_0} R(x_0,x_0^{'},\omega) T_d^{inv}(x_0^{'},x_i,\omega) dx_0^{'}; \tag{2.4}$$

where T_d^{inv} is the time-reversal of the direct arrival from the focusing point to the surface. Note that T_d^{inv} is also the initial value of f_1^+, and T_d^{inv} can be approximated with any approach that can calculate travel time between two points with a given background velocity model.

Finally, in the time window when $t < t_d$, $G^-(x_i, x_0, \omega)$ and $G^+(x_i, x_0, \omega)$ are obtained by substituting the $f_1^-(x_0^{'}, x_i, \omega)$ and $f_1^+(x_0^{'}, x_i, \omega)$ into equation 5.1.

2.3.2 Source redatuming

Once the up- and downgoing Green's functions are correctly retrieved, we use them to obtain the redatumed reflection response $\tilde{R}(x_i, x_i^{'}, \omega)$ that satisfies (Wapenaar *et al.*, 2014b),

$$G^+(x_0, x_i, \omega) = \int_{\partial D_i} \tilde{R}(x_i, x_i^{'}, \omega) G^-(x_0, x_i^{'}, \omega) dx_i^{'} \tag{2.5}$$

Here $\tilde{R}(x_i, x_i^{'}, \omega)$ can be interpreted as the redatumed reflection response as if both the sources and receivers are placed at depth level ∂D_i in a medium that is identical to the physical medium below ∂D_i and homogeneous above (as shown in the right part of Figure 2.1). Such redatumed data only contain the seismic reflection events resulting from the geological structures below ∂D_i. Significantly, any complex overburden between the acquisition depth ∂D_0 and redatumed depth ∂D_i (e.g. weathered layers or salt bodies) does not affect the redatumed data. In this study, we use the multidimensional deconvolution (MDD) approach proposed by van der Neut *et al.* (2011) and Wapenaar *et al.* (2014b) to solve equation 5.5 and obtain $\tilde{R}(x_i, x_i^{'}, \omega)$.

2.3.3 Imaging

The redatumed reflection response $\tilde{R}(x_i, x_i^{'}, \omega)$ can be used in different ways for imaging. One approach is to obtain the full reflection response by redatuming the sources and receivers at the same depth level, and then utilize the redatumed data to form a seismic image below the redatuming depth level using any established imaging algorithms (e.g. RTM). Note that a velocity model for the areas below the redatuming depth level is also needed in the imaging stage if one wants to perform RTM using the redatumed data in this way.

An alternative approach for imaging (which is the one we adopted in this paper) is that: for every image point inside a target zone, we extract the zero-offset and zero-time component $\tilde{R}(x_i, x_i, t = 0)$ from the redatumed reflection response $\tilde{R}(x_i, x_i', t)$, and construct an image of the zero-offset reflectivity using

$$I(x_i) = \tilde{R}(x_i, x_i, t = 0). \tag{2.6}$$

With this imaging condition, we can compute the reflectivity of every image point in a target zone. This approach for imaging is more robust in that it does not create the artifacts from the local internal multiples below the redatuming level, but it comes with an additional cost of performing Marchenko redatuming and MDD for each depth level.

2.4 Synthetic examples

We first demonstrate and interpret the up- and downgoing Green's function retrieved by Marchenko receiver redatuming with a synthetic example for a subsurface point in a 2D acoustic medium (which contains a salt body). We verify the retrieved Green's function by comparing it with the Green's function for the same subsurface point which is obtained through directly modeling using the finite difference method. Next we investigate the influence of the missing near offsets for practical consideration of marine streamer surveys. Finally, we illustrate the importance of calibration for the amplitudes of the data, and discuss how we calibrate the field dataset which we use in the following section.

2.4.1 Green's function obtained through Marchenko redatuming and finite-difference modeling

As a preparation for our field data application, we demonstrate and interpret the up- and downgoing Green's functions retrieved by Marchenko receiver redatuming with a synthetic example. The background velocity model (Figure 5.1a) is estimated from a GOM field dataset (the dataset that is used in our field data application). In the corresponding density model (Figure 5.1a and Figure 5.1b), we add four flat horizontal reflectors with the thickness of 100 m at the depth levels of 3 km, 4 km, 5 km, and 6 km. The density of these four

reflectors are 100 g/cm^3 smaller than the surrounding areas. We generate 1000 shot records with 361 receivers in each shot record using acoustic finite-difference modeling. The spacing between sources and receivers is set as 26.67 m. This synthetic dataset is simulated to match the field dataset for source and receiver locations.

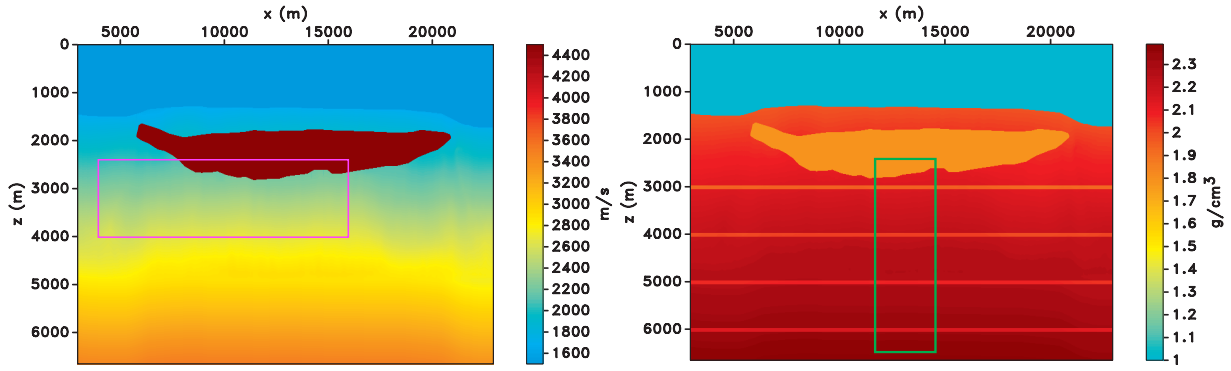

(a) (b)

Figure 2.3: Illustration of the velocity and density models used for the synthetic examples. (a) Velocity model. Red box encloses the target area for which we produce images using field data. (b) Density model. Green box encloses the target area for which we produce images using synthetic data.

Using Marchenko receiver redatuming, we retrieve the up- and downgoing Green's functions for a subsalt point at $x = 13,225\ m$ and $z = 3,500\ m$, which is referred to as the virtual receiver. The retrieved downgoing Green's function (Figure 2.4a) can be interpreted as the seismic wavefields that are excited by the surface sources and are propagating downward when they reach the virtual receiver. The first event (labeled with a) in the downgoing Green's function is the direct arrival from the surface sources to the virtual receiver. The downgoing Green's function contains internal multiples. For example, the hyperbola (labeled with b in Figure 2.4a) corresponds to the internal multiples that are reflected inside the salt body. The ray path of this event is drawn in Figure 2.4c, also labeled with b. The retrieved upgoing Green's function (Figure 2.4b) contains the wavefields that are propagating upwards when they reach the virtual receiver. These wavefields start downward propagating from the surface sources and are reflected upward by the structures below the virtual receiver. The

three major events in Figure 2.4b (labeled with 1, 2, and 3) correspond to the primary reflections from the three reflectors below the virtual receiver. Their ray paths are shown in Figure 2.4c.

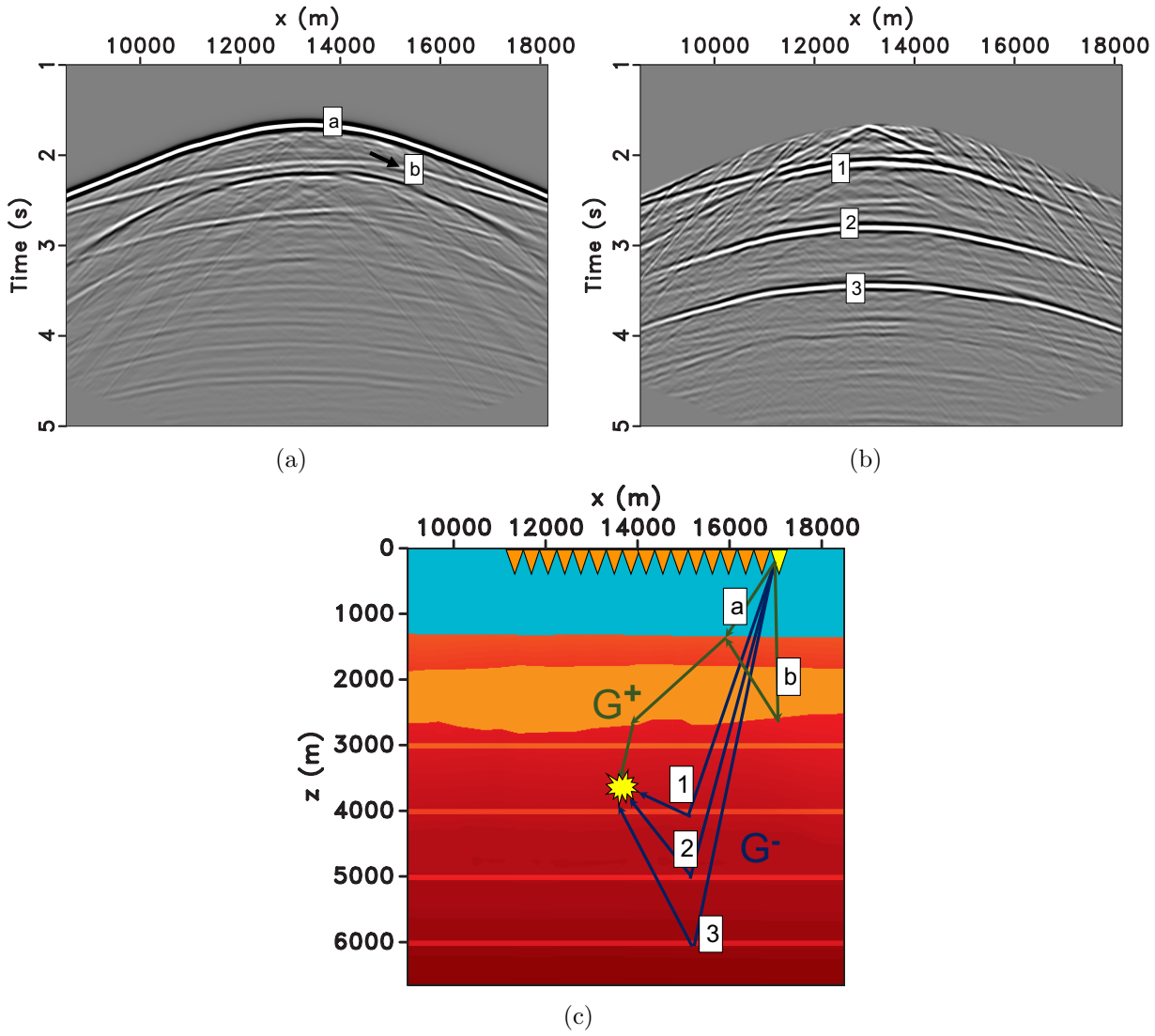

Figure 2.4: (a) Retrieved downgoing Green's function G^{+}. (b) Retrieved upgoing Green's function G^{-}. The linear dipping events appearing around 2 seconds are the artifacts caused by the limited aperture of the dataset used in this example. (c) Physical interpretation of G^{+} and G^{-}.

The sum of the up- and downgoing Green's functions is the total Green's function recorded at the virtual receiver (Figure 2.5a). In a numerical experiment to verify the total Green's function retrieved by the Marchenko scheme, we place a line of sources on the

surface and a receiver at the same location as the virtual receiver at $x = 13,335\ m$ and $z = 3,500\ m$ and then record the wavefield directly using finite-difference modeling. As shown in Figure 2.5, the wavefield retrieved by the Marchenko redatuming method matches very well with the directly modeled wavefield in the near-offset parts. The retrieved Green's function has some artifacts for far offsets because of the limited acquisition aperture. The inconsistencies in Figure 2.5 that appear near the direct wave are due to the use of the time reversed direct wave. As demonstrated by Vasconcelos *et al.* (2015) and Vasconcelos & van der Neut (2016), using a physics-driven estimate of the inverse transmission to obtain the direct arrivals may improve the amplitudes of events in the retrieved Green's functions.

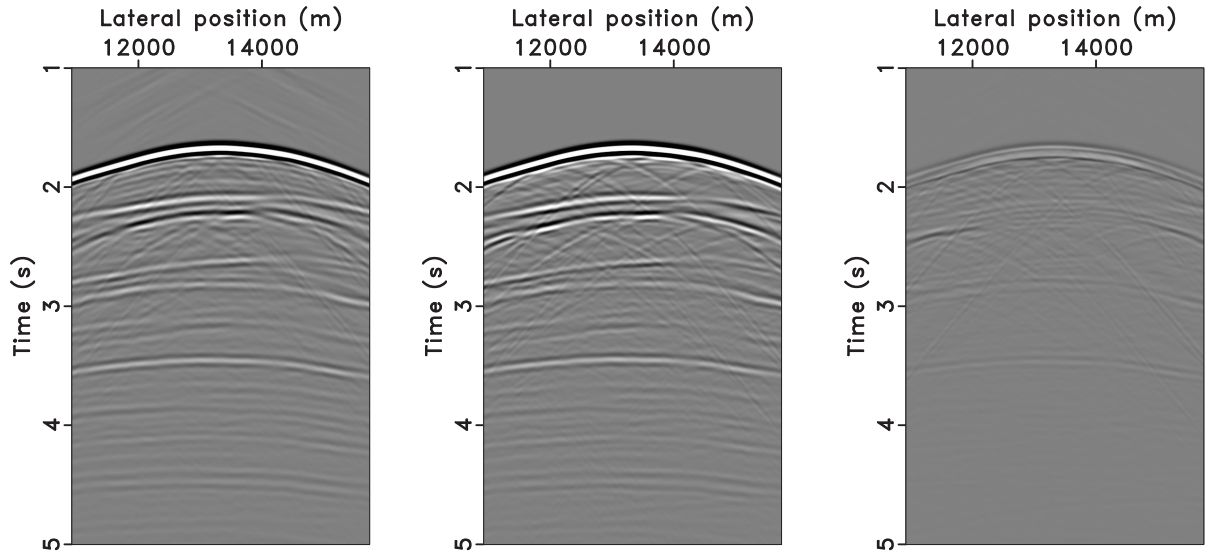

Figure 2.5: (a) The retrieved the Green's function for a virtual receiver at $x = 13,335\ m$ and $z = 3,500\ m$.The sum of up- and downgoing field of Figure 2.4. (b) The directly modeled Green's function for a virtual receiver at $x = 13,335\ m$ and $z = 3,500\ m$. (c) Difference between the retrieved Green's function in (a) and directly modeled Green's function in (b).

2.4.2 Requirements for acquisition geometry

Marchenko redatuming requires the surface reflection response R to be obtained by an evenly and densely sampled array of sources and receivers with a recording aperture as large as possible. van der Neut *et al.* (2015a) showed that the sources and receivers should be

placed at the corresponding stationary points to retrieve some particular up- or downgoing events, and sometimes stationary points cover the entire surface. The field dataset used in this study is acquired with the standard towed-streamer acquisition system, which contains traces on only one side of the source for each shot record. One can reconstruct the traces on the other side of each source using the source-receiver reciprocity theorem, forming a dataset with two-sided offsets (given the source line is much longer than the maximum offset). However, the near-offset data cannot be practically acquired for towed marine surveys. In the field dataset we use, offsets from $h = -107\ m$ to $h = 107\ m$ (7 traces) are missing. Therefore, we first investigate whether a dataset with missing near offsets in the shot records can be directly used for Marchenko redatuming.

For Marchenko redatuming, each trace in the retrieved Green's functions is constructed by first convolving a trace in the reflection response with a trace in the first arrival, where both traces correspond to the same location at the surface, and then summing over all the source locations (equation 5.1). In both our synthetic and field examples, there should be 361 traces in each shot record if the near-offsets (including zero offset) can be acquired. With the seven near-offset traces missing in each shot record, each trace in the retrieved Green's functions contains the contribution of the remaining 354 traces. We first consider the moveout time difference Δt between the apex of the hyperbola and the maximum missing near-offset in a shot gather to evaluate the influence of these seven missing traces. Under the assumption of horizontally layered earth, Δt is given by

$$\begin{aligned} \Delta t &= \sqrt{t_0^2 + \frac{h^2}{4v_{nmo}^2}} - t_0; \\ &\simeq \frac{h^2}{8v_{nmo}^2 t_0}, \end{aligned} \tag{2.7}$$

where t_0 is the two-way zero-offset travel time, h is the maximum missing near offset, and v_{nmo} is the normal moveout velocity. We make a first order approximation of the square root term to obtain the formula in equation 2.7. We are able to obtain a good retrieval of

the Green's function from the data with missing near-offsets when the variation of the travel time of the reflection in the missing trace Δt is much less than the dominant wave period of the wave of interest T, hence we require that

$$\Delta t \leq \frac{T}{8}. \tag{2.8}$$

Spetzler & Snieder (2004) showed that the denominator of the right hand side in equation 2.8 should be no less than 8/3 for 2D cases and no less than 2 for 3D cases (equation 4 in their paper). To be conservative, we use a stricter condition in this derivation and set the denominator of the right hand side in equation 2.8 to 8. Then the maximum missing near offset h should satisfy

$$\begin{aligned} h &\leq \sqrt{T v_{nmo}^2 t_0}; \\ &\leq \sqrt{2DT v_{nmo}}, \end{aligned} \tag{2.9}$$

where $D = v_{nmo}t_0/2$ is the depth of the first interface of interest. Obviously, with less missing inner traces (smaller h) we obtain a better retrieval of the Green's functions. Meanwhile, if D, T and v_nmo are larger, the Green's function retrieval is less disturbed by the missing near offsets. In a seismic survey, the dominant wave period can be estimated from the frequency spectrum of the data. Equation 2.9 tells us that the influence of the missing near offsets becomes smaller for deeper events (larger D and v_{nmo}).

To investigate the influence of the missing near offsets numerically, we generate two synthetic datasets using finite-difference modeling with the velocity and density models used above (Figure 5.1). The first dataset (a full dataset) contains 361 shot records, with 361 traces in each shot record. For the second dataset (a dataset with missing near offsets), we remove seven receivers near each source (one trace at the same location as the source position and three nearest traces on both sides), and obtain the double-sided dataset with the maximum missing offset of 214 m (identical to the field dataset we use). In this example, D is approximately 1,550 m, T is approximately 0.0285 s (as the dominate frequency of the data is approximately 35 Hz), and v_{nmo} is approximately 1,500 m/s, so according to

equation 2.9, h should be $\leq 258\ m$. Since the maximum missing offset ($214\ m$) satisfies the criterion (equation 2.9), we expect a good retrieval of the Green's functions using the dataset with missing near offsets. Note, we use a much stricter condition (8 instead of 8/3 in the denominator in equation 8) to account for the fact that the dominant period of the reflection response R can be larger than the data before source deconvolution. This is based on the assumption that the dominant frequency will not increase as many as three times before and after the source deconvolution. The total retrieved Green's functions with the full dataset (Figure 2.6a) and the dataset with missing near offsets (Figure 2.6b) are very close to each other. We show the difference panel of these two Green's functions in Figure 2.6c. The difference panel shows the effect of the missing near-offsets. Some shallow events at the near offset are not fully retrieved using the missing near offset data, which can be predicted by equation 2.9. In general, as the internal multiples generators in this example are relatively deep, our approach is not heavily affected by these seven near-offset traces in each shot record.

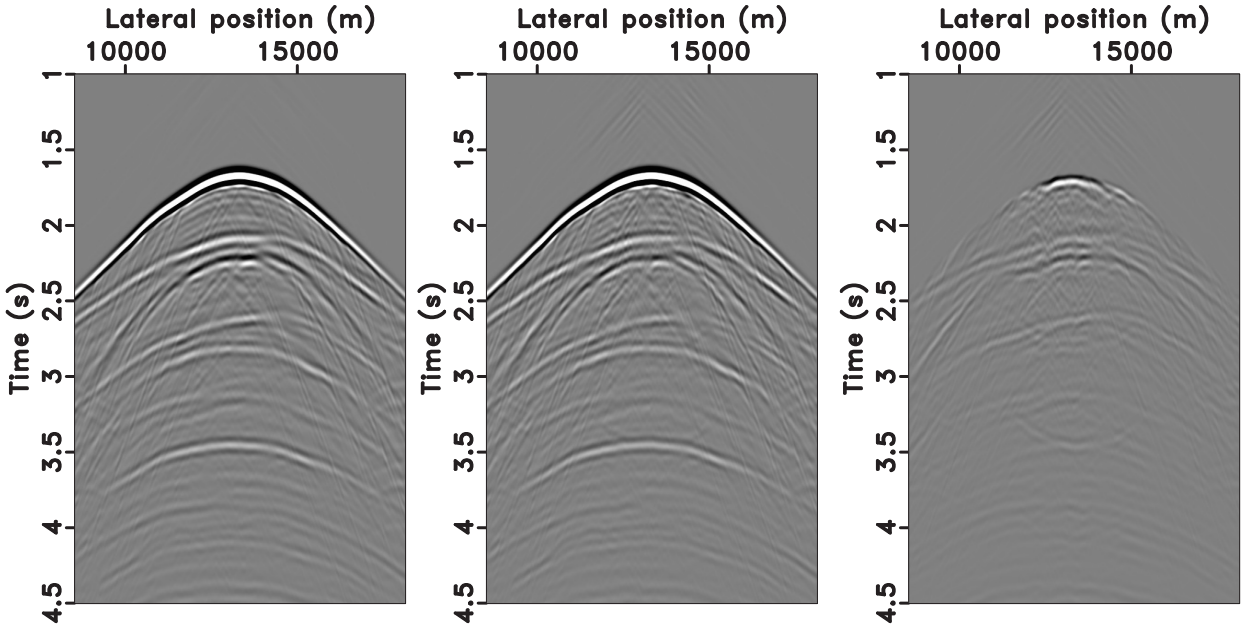

Figure 2.6: (a) Redatumed field retrieved from the data with full offsets. (b) Redatumed field retrieved from the data with missing near offsets. (c) Difference between (a) and (b).

We perform Marchenko imaging with the method discussed above for the same target zone (Green box in Figure 5.1b) using these two datasets and apply reverse time migration (RTM) with the full dataset. According to the density model, the final images should contain the salt bottom and four horizontal reflectors. The Marchenko image produced using the full dataset (Figure 2.7a) is very similar to the one produced using the dataset with missing near offsets (Figure 2.7b). Both contain all the expected reflections. Note that in the RTM image (Figure 2.7c) an additional reflection appears with a similar shape as the salt bottom. This additional reflection is an artifact introduced by a set of peg-leg internal multiples. This type of artifacts is completely removed in Figure 2.7a and largely suppressed in Figure 2.7b. To evaluate the artifact introduced by using the data with missing near offsets, we use the horizontal reflector at $z = 4,000\ m$ as a reference (the maximum amplitude of this reflector is set as 1 unit). The maximum amplitude of the artifact caused by internal multiples (at approximately $x = 13,335\ m$, $z = 3,300\ m$) in Figure 2.7b is 0.52 unit, and the maximum amplitude of the artifact caused by internal multiples (pointed by the black arrow) in Figure 2.7c is 1.79 unit. Hence, even the artifact is not completely removed when using the data with missing near offsets, the amplitude of the spurious event in the RTM image is approximately 3.5 times larger than that in the Marchenko image produced using the data with missing near offsets. The suppression of the internal multiple artifacts becomes less successful towards the right edge of the image. This may be associated to the fact that the overlaying salt bottom has a steeper dip on the right side of the image.

2.4.3 Data calibration

The initial step of the iterative scheme in Marchenko redatuming is to convolve the surface reflection response R with the time-reversal of first arrival T_d^{inv} (equation 5.4). The convolution result is subsequently substituted into equation 5.3. In the initial iteration of equation 5.3 ($k = 0$), the convolution result of R and T_d^{inv} is used to convolve with R once more to get M_0^+, and R will be used to convolve with the intermediate results repeatedly in the following iterations. Hence, the amplitudes of the surface reflection response R need to

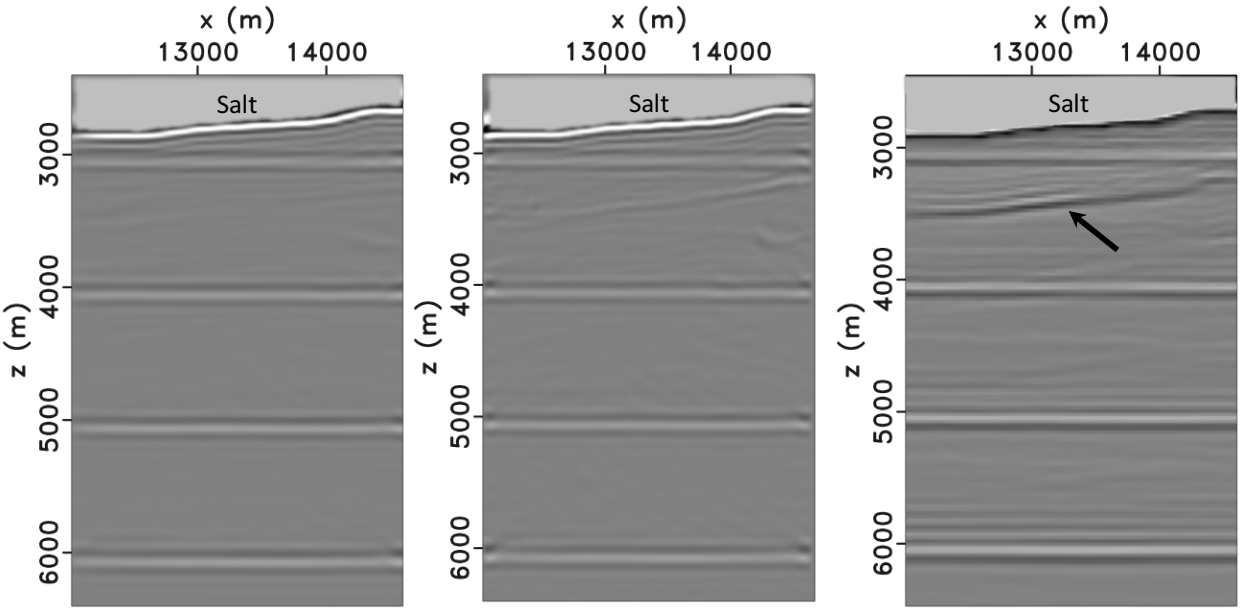

Figure 2.7: (a) Marchenko image using the data with full offsets. (b) Marchenko image using the data with missing near-offsets. (c) RTM image using the data with full offsets.

be properly calibrated such that R should be the response to a line of impulsive sources with unit amplitudes. Note, in this example, we obtain the first arrival from a subsurface point to the surface by: 1) computing the first arriving travel time (using a Eikonal solver), and 2) placing a Ricker wavelet (15 Hz) at the first arriving travel time. The maximum amplitude of the Ricker wavelet is not significant in the iterative process, as it puts a scaling factor on all the Green's functions and focusing functions accordingly (equation 5.3 and 5.4), and the scaling factor will drop out during the MDD process indicated by equation 5.5.

In practice, the first step to approximate the required R from the surface seismic data D is to estimate the source wavelet and deconvolve the source wavelet from D. We then need to calibrate the deconvolved data obtained from the first step by the following approach. In the synthetic examples, we are able to compute the exact scaling factor for data calibration as the source wavelet is known. As shown in Figure 2.8b. the upgoing Green's function (for a focus point at $x = 13,335\ m$ and $z = 3,200\ m$) retrieved with the correctly calibrated R is free of artifacts. In Figure 2.8a and FigureFigure 2.8c, we show that the retrieved Green's

functions are contaminated with artifacts if the data are not correctly calibrated. Figure 2.8a shows the upgoing Green's function retrieved using the surface reflection response R which is too small (scaled by a factor of 0.5 relative to the correctly calibrated R). The artifact caused by the incorrect data calibration is depicted in Figure 2.8a (arrow). When R is too large, the iteration scheme can not converge. In Figure 2.8c, we show that when the amplitudes of R are too large (where R is multiplied by a scaling factor of 1.5), the retrieved Green's function is dominated by artifacts. We produce three Marchenko images using the Green's functions retrieved from these three sets of surface reflection responses R: the over- calibrated (with a scaling factor equals to 0.5), the correctly-calibrated (with a scaling factor equals to 1), and the under-calibrated (with a scaling factor equals to 1.5). For the over-calibrated case, the artifacts in the Green's functions result in an artifact in the final image (Figure 2.9a). Note that this artifact shares the shape of the salt bottom and results from an incorrect handling of the internal multiples. For the under-calibrated case, the imaging result completely breaks down (Figure 2.9c) as the retrieved Green's functions are dominated by artifacts. Finally, in Figure 2.9b, with the Green's functions retrieved from the correctly calibrated R, we produce an image which is consistent with the velocity and density models and free of artifacts due to multiples.

In the field data application that follows, we obtain the time-reversal of the first arrival T_d^{inv} in a exact same way by using the same velocity model to compute the first arriving time and placing a same Ricker wavelet. However, given a surface seismic dataset, we do not have any information about the amplitude of the original source functions. In addition, we do not know what seismic processing steps (e.g. noise attenuation and gain function) the field dataset has gone through, hence the recorded amplitude differs in general from the true amplitude. Therefore, we calibrate the field dataset by comparing it with the synthetic dataset with missing near offsets (which is used in retrieving the Green's function in Figure 2.8b). At the same source location, we pick a shot record from the field dataset and a shot record from the synthetic dataset. By dividing the maximum amplitude of each shot

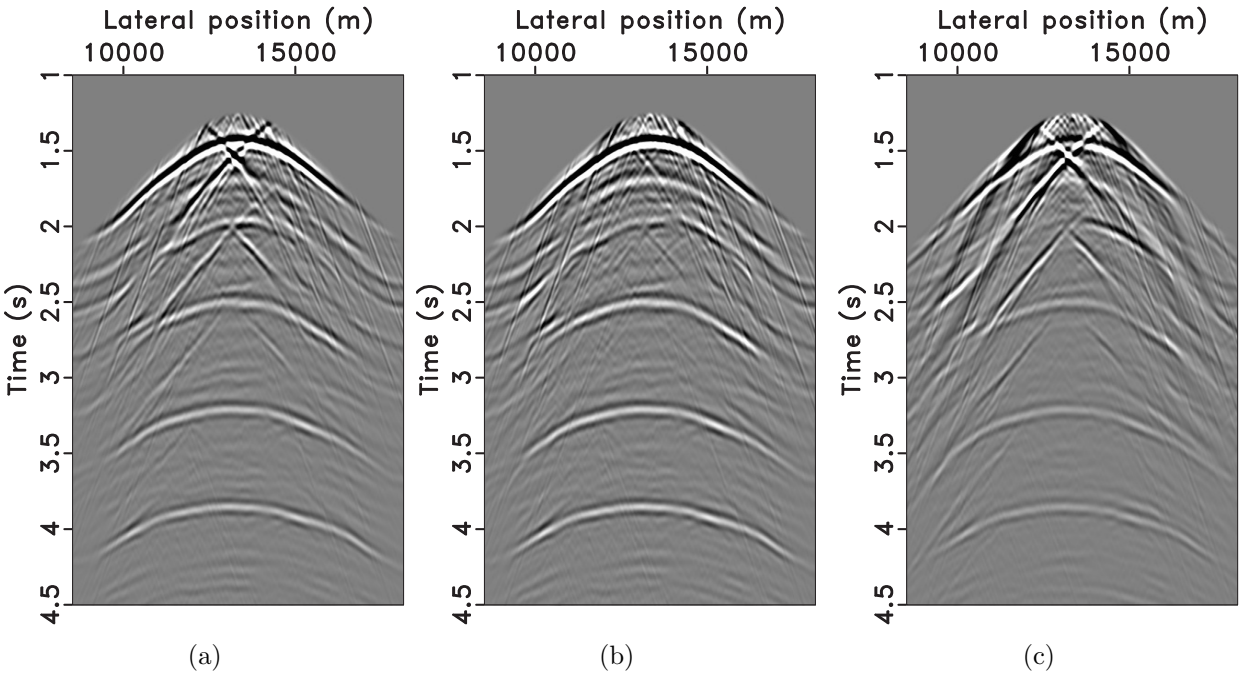

Figure 2.8: (a) The retrieved upgoing Green's function when the reflection response is scaled by a factor of 0.5. (b) The retrieved upgoing Green's function when the reflection response is scaled by a factor of 1.0. (c) The retrieved upgoing Green's function when the reflection response is scaled by a factor of 1.5.

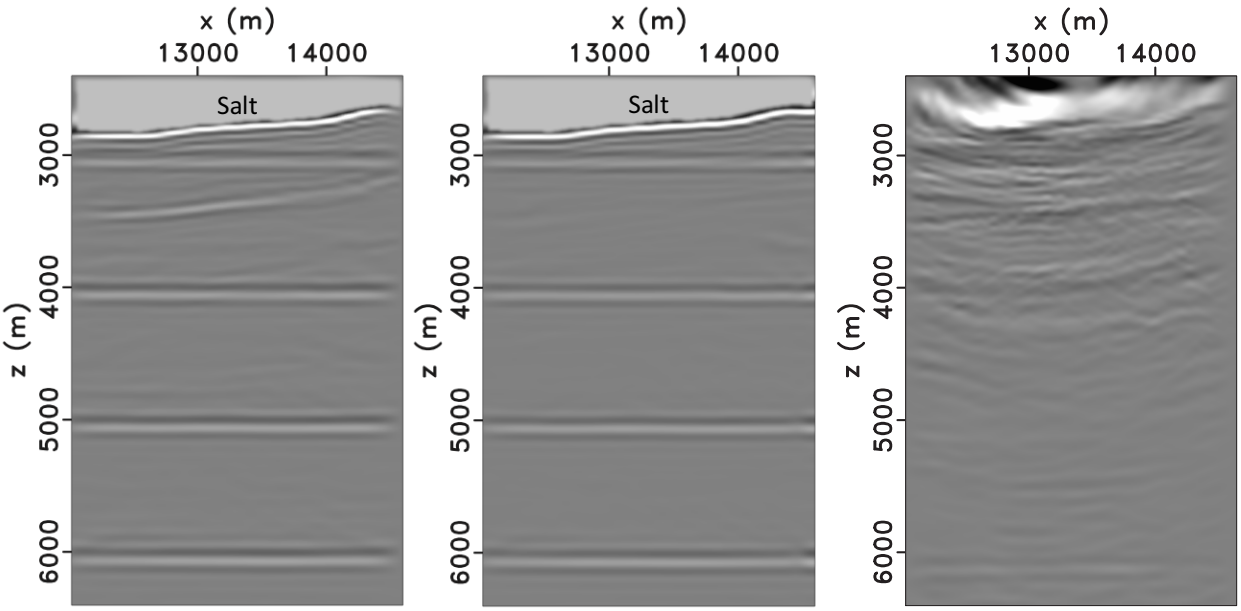

Figure 2.9: (a) The Marchenko image obtained from the Green's functions retrieved with the reflection response scaled by a factor of 0.5. (b) The Marchenko image obtained from the Green's functions retrieved with the reflection response scaled by a factor of 1.0. (c) The Marchenko image obtained from the Green's functions retrieved with the reflection response scaled by a factor of 1.5.

record, we can obtain the scaling factors for the calibration of each field shot record. Other from our method to do amplitude calibration, van der Neut *et al.* (2015b) used a different approach to estimate the scaling factors. They applied minimization of the energy norm of the up-going Green's function as a criterion to perform the data calibration.

2.5 Field data example: Mississippi canyon, Gulf of Mexico

The 2D marine field dataset we use was acquired over the Mississippi Canyon in the Gulf of Mexico. This area contains a shallow salt body in a deep water environment. A total of 1000 shots were fired along a 26 km source line with a shot spacing of 26.67 m.

2.5.1 Data Processing

In this study, we design a work flow to apply Marchenko imaging to the streamer dataset (Figure 5.10). With a background velocity model, we estimate the direct arrivals from all the subsurface points in the target zone to the surface by computing the travel time using an Eikonal solver using fast marching method (Fomel, 1997) and placing a Ricker wavelet at the direct arrival time. For the data processing, we 1) apply SRME to the surface seismic data for the suppression of the surface multiples; 2) deconvolve the source signature and the suppress its bubbles; 3) generate the data with two-sided offsets in the common shot gathers based on the data with one-sided offsets; and 4) calibrate the amplitudes of the data using the scaling factor estimated from the comparison with the numerically modeled shot records. Details for data preparation are discussed below.

For this dataset, the sources and receivers share the same the location along the 2D acquisition line. Note co- located sources and receivers are required by Marchenko redatuming, however, shot-based algorithms, such as RTM, do not have such requirements. This field dataset has been processed to correct for attenuation. If strong attenuation presents in the data, correction for attenuation is required before applying Marchenko receiver redatuming. Considering that convergence of the approach proposed by Singh *et al.* (2015a) is not always guaranteed, in this study, we start by applying SRME to suppress the free-surface

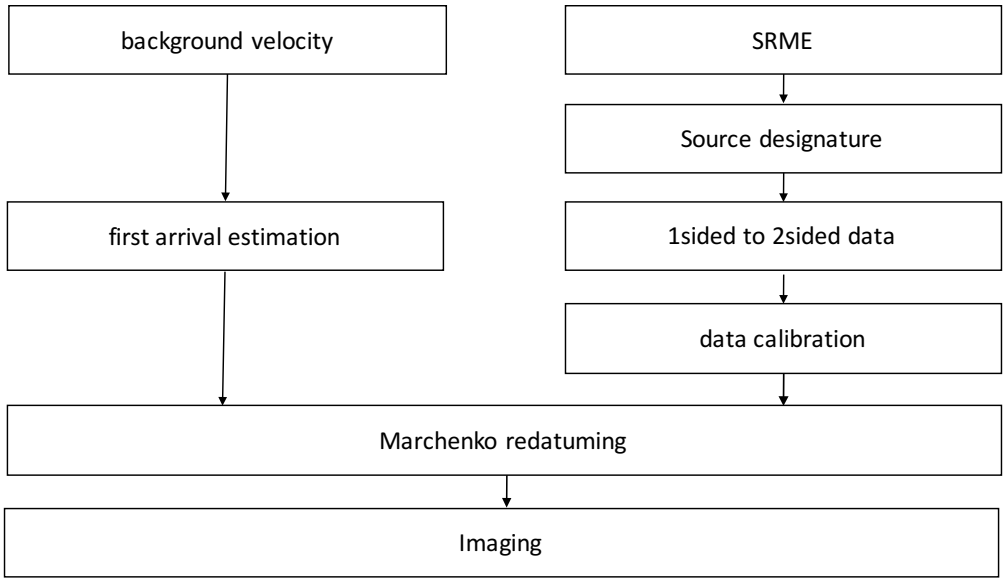

Figure 2.10: Workflow to apply Marchenko imaging to field data.

multiples before performing Marchenko redatuming. As shown in equation 5.3, in the frequency domain implementation of the algorithm, the reflection response $R(\omega)$ is required, not $R(\omega)S(\omega)$ (where the source wavelet is contained in the reflection response). Therefore, the Marchenko redatuming algorithm requires an accurate deconvolution of the source wavelet from the data. We remove the effect of the source signature from the data using the sparse log- domain deconvolution approach of Guitton & Claerbout (2015). Using the reciprocity theorem, we then generate the data with two-sided offsets from the data with one-sided offsets to increase the range of the aperture of the surface reflection response. Theoretically, Marchenko redatuming requires the reflection response to be obtained from dipole sources and pressure receivers (or monopole sources to particle velocity receivers). However, the dataset we have is obtained with pressure source and pressure receivers (standard marine streamer data) and we did not apply any monopole-to-dipole conversion. In this example, even though we discard the requirement for dipole sources and pressure receivers, we are still able to see that the artifacts caused by internal multiples are suppressed in the field Marchenko image (as shown in the section of "Field data Marchenko images"), however, the impact of this requirement needs further investigation. As discussed above, we do not

need to reconstruct the missing near offsets for this dataset. To approximate the physical earth's reflection response R_{real}, after processing the recorded surface data, we also need to calibrate R with a scaling factor s such that $R * s = R_{real}$. Here s is an unknown factor which depends on the acquisition methods and the processing chain. In this application, we find this scaling factor by comparing the maximum amplitude of a field shot record with a synthetic shot record, as we use both the same velocity model and approach to estimate the direct arrivals in both synthetic and field data examples. Figure 2.11 shows the comparison a field shot record and a synthetic shot record. As the first waves of both records (which are used to compute the scaling factor) match fairly well, it is reasonable to use the maximum amplitude of the first waves for amplitude calibration. Scaling factors are computed and applied shot by shot, however, in this example we find that the scaling factors for all shots do not significantly vary. The approach that we proposed to find the scaling factor is simple and robust, yet one obstacle of this approach is that as we obtain the scaling factor based on the first waves, the rest of the data may be scaled with artifacts. The adaptive Marchenko redatuming proposed by van der Neut *et al.* (2015b) is another valid method to overcome the unknown scaling factor issue in the reflection data. Figure 2.12 and Figure 2.13 show the comparison of a near-offset sections and a shot gather of the raw data and the data after source- designature and SRME.

subsectionField data Marchenko images For imaging, we retrieve the up- and downgoing Green's functions for all the subsurface imaging points inside the target zone (red box in Figure 5.1a, 4.0 km - 16.0 km horizontally and 2.4 km - 4.0 km vertically). We use 11 iterations in the Marchenko redatuming process. The virtual source (focusing points) sampling in x and z directions is 26.67 m, which is same as the source and receiver sampling on the surface. This target area contains the bottom and the left edge of the salt body, some sediment layers to the left of the salt body, and structures below the salt body. Following equation 5.5, we create the redatumed reflection response $\tilde{R}(x_i, x_i^{'}, \omega)$ at each depth level. We then produce the Marchenko image by extracting the zero-time zero-offset value

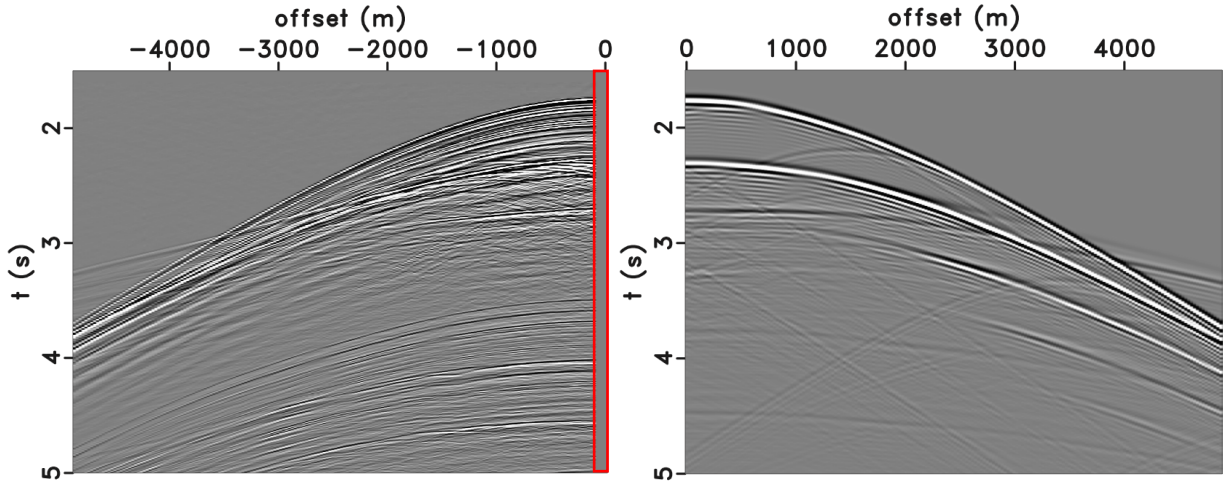

(a) (b)

Figure 2.11: Comparison of (a) field shot record and (b) synthetic shot record which are used to compute the scaling factor. The red box indicates the missing near offset traces in the field shot record. Note the events due to the three horizontal layers in Figure 5.1b are included in the synthetic shot record.

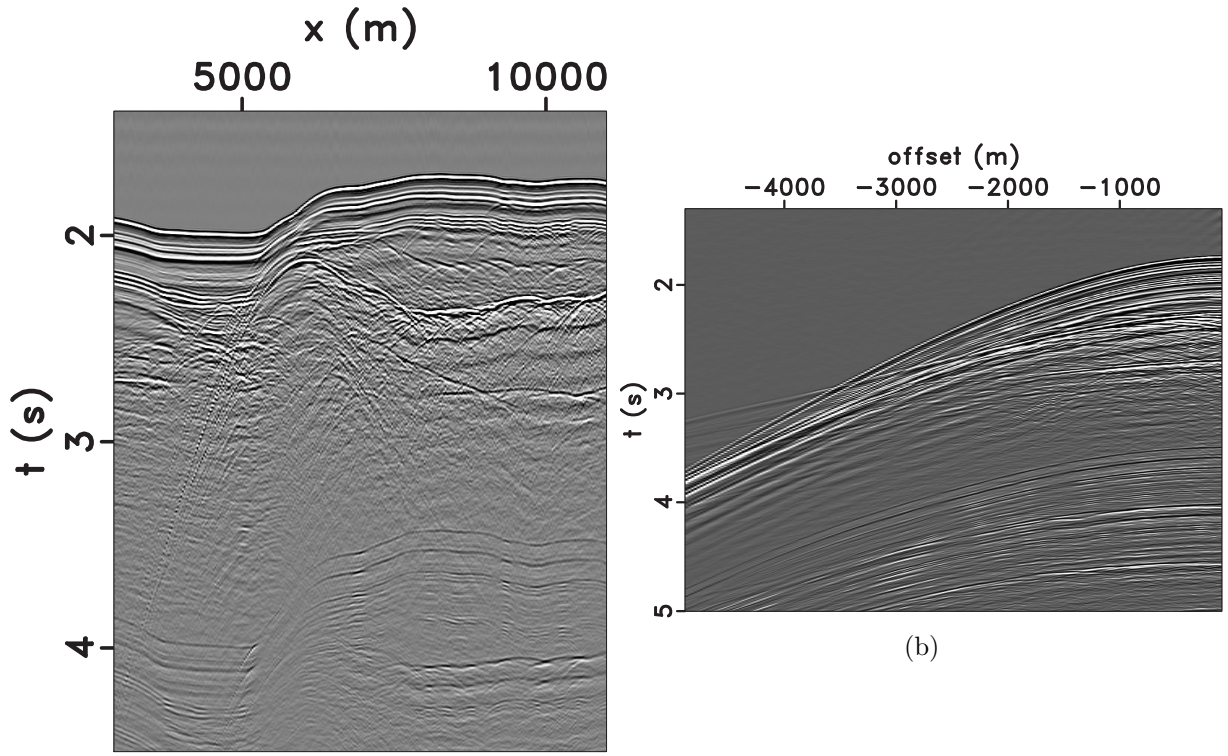

(a) (b)

Figure 2.12: (a) Raw field data: a near-offset section. (b) Raw field data: a shot record.

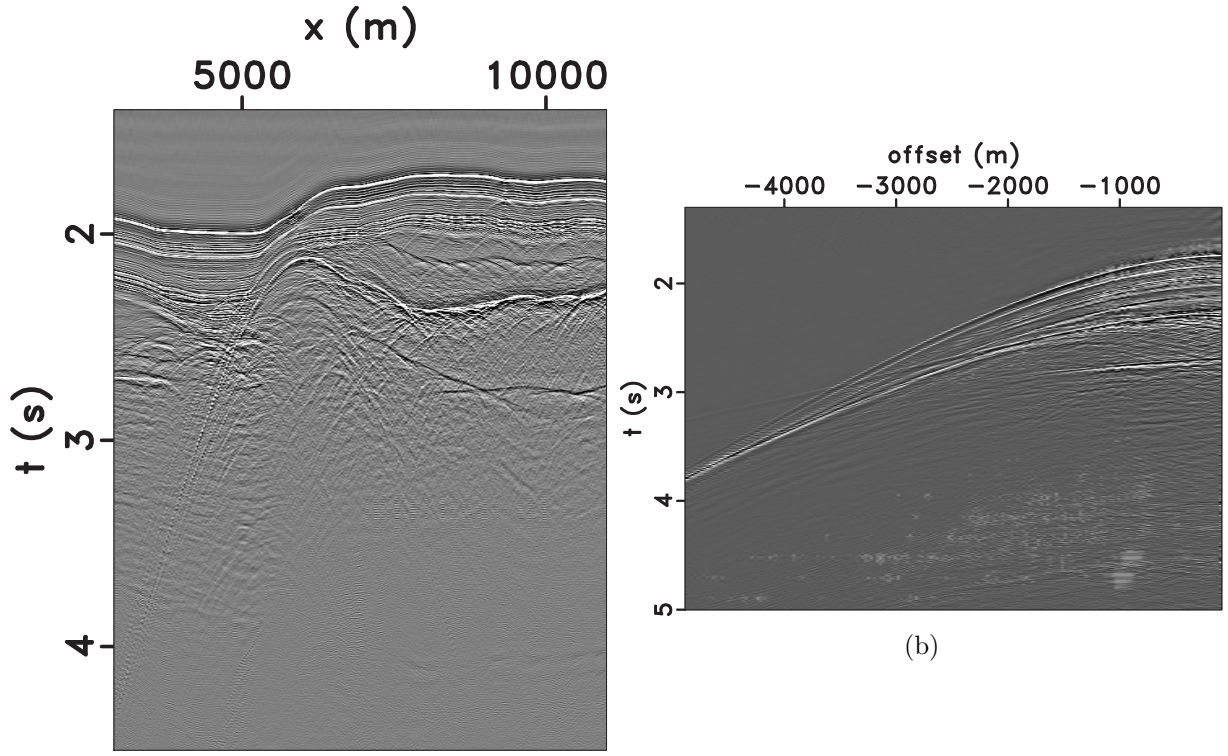

(a)

(b)

Figure 2.13: (a) Field data after source-designature and SRME: a near-offset section. (b) Field data after source-designature and SRME: a shot record.

$\tilde{R}(x_i, x_i, t = 0)$, as instructed in equation 5.6.

A comparison between the Marchenko image (Figure 2.14b) and the image produced using standard RTM (Figure 2.14a) shows that they are comparable for the most part: both present similar structures for the bottom of the salt body, the structures of the sediment layers to the left of the salt body, and the detailed structures of the subsalt area. Furthermore, we find significant improvements in the Marchenko image: 1) the reflectors are more continuous and smoother (green arrows in Figure 2.14a and Figure 2.14b); 2) the structures of the sediment layers to the left of the salt body are more clearly revealed (red arrows in Figure 2.14a and Figure 2.14b); 3) additional structural features are revealed (blue arrows in FigureFigure 2.14a and Figure 2.14b).

To better understand these improvements accomplished in the Marchenko image, we produce an RTM image for the same target area using the synthetic dataset generated using the models in Figure 5.1. In this RTM image (Figure 2.14c), we observe some artificial reflections who have a shape similar to the bottom of the salt (dashed green arrow in Figure 2.14c), which indicates the artifacts result from internal multiple reflections at the salt bottom. When these artificial structures interfere with the horizontal reflector at 3 km, the phases of the horizontal reflector are either added or subtracted, creating amplitude discontinuities (solid green arrows in Figure 2.14c). Hence, the discontinuities in the field data RTM image (Figure 2.14a) could also result from the interference between the multiple artifacts and real sedimentary layers. As the Marchenko imaging method correctly handles internal multiples, it is able to produce an image (Figure 2.14b) that is more continuous and free from the multiple artifacts. The layered structures to the left of the salt body (red arrows in Figure 2.14a and Figure 2.14b), revealed both in the RTM image and the Marchenko image, are sedimentary layers beneath the seabed. Note that the amplitudes of these sedimentary layers in the RTM image are suppressed, while the layers are more clearly revealed and more comprehensible in the Marchenko image (red arrows in Figure 2.14a and Figure 2.14b). This is because the imaging approach we adopted also removes all the artifacts caused by the

internal multiples that originate within the target zone (in contrast to the approach of using the MDD-redatumed reflection response as input for RTM). Moreover, Marchenko imaging reveals some structural features (blue arrows in Figure 2.14b) that are not presented in the RTM image.

2.6 Discussion

Internal multiples can play two completely different roles in seismic imaging: if the primaries are well recorded, internal multiples create artifacts in migration and therefore should be removed; if there is significant portion of primaries unrecorded, internal multiples have the potential to improve the illumination of the subsurface and should be utilized for imaging. In the synthetic and field examples presented in this study, we focus on the artifacts caused by the internal multiples related to salt bodies. In these examples, we assume that the primaries are well recorded and are sufficient for producing a subsalt image, however, the internal multiples in the data will introduce artifacts, which contaminate the image. Wapenaar *et al.* (2016) discussed the role of multiples in Marchenko imaging and presented a potential approach to use multiples (instead of remove) in Marchenko imaging. In our implementation of Marchenko deconvolution imaging, the effect of internal multiples are eliminated for a cleaner subsalt image.

About the value of the denominator on the right hand side in equation 2.8, it is set as 8 in this study, based on the assumption that the dominant frequency will not increase as many as three times before and after the source deconvolution. Theoretically, it should be larger than 8/3 for 2D cases and larger than 2 for 3D cases (Spetzler & Snieder, 2004). The reason that we use a much stricter value is that the dominant frequency of the reflection response can be larger than the dominant frequency of the original data (before source deconvolution), and a stricter condition will compensate this.

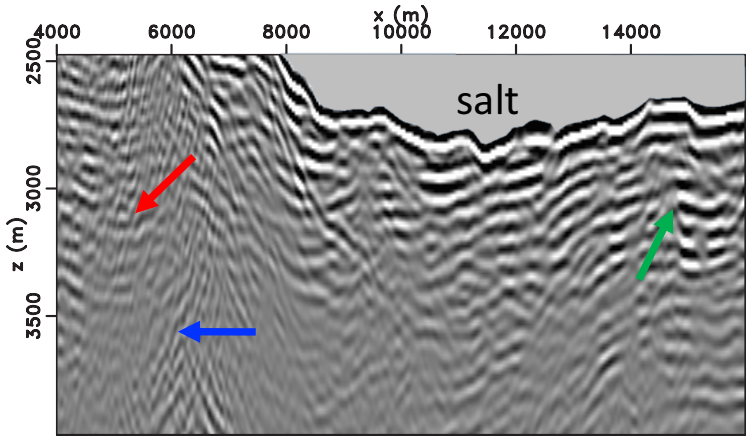

(a)

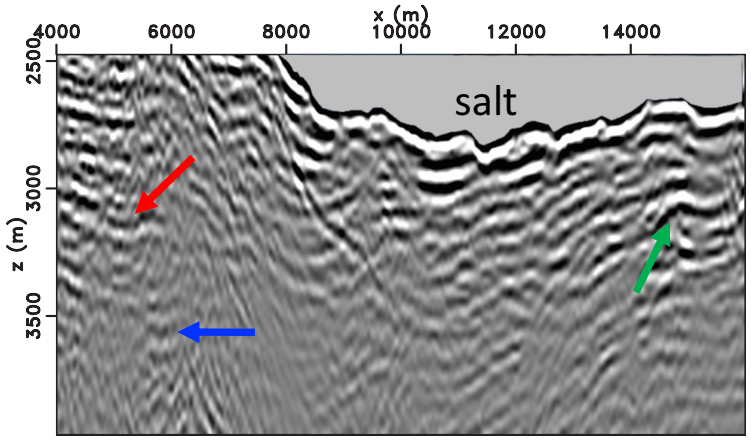

(b)

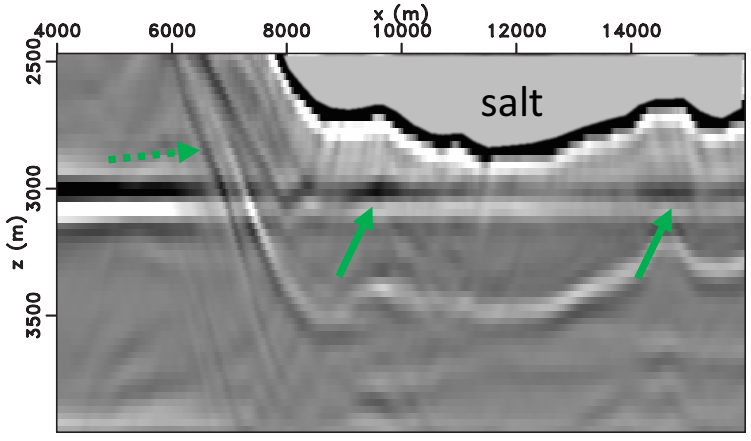

(c)

Figure 2.14: (a) RTM image with the field dataset. (b) Marchenko image with the field dataset. (c) RTM image with the synthetic dataset generated from velocity and density models in Figure 5.1.

2.7 Conclusions

We successfully apply subsalt Marchenko redatuming and imaging to a marine dataset from the Gulf of Mexico. With some numerical experiments, we investigate the effect of the missing near-offset traces, and conclude that the artifacts caused by multiples can be largely suppressed by directly using the missing near offset data. We show that calibration of the data need to be properly performed, and we calibrate the data based on the comparison with the numerically modeled dataset in this study.

We present that the image produced by Marchenko imaging is more continuous than the RTM image produced using the same dataset and velocity model. Furthermore, the Marchenko method seems able to reveal some structures that cannot be found in the RTM image. We use an RTM image produced with a synthetic dataset to demonstrate that the discontinuities in the RTM image are very likely caused by internal multiples. The improvements in the Marchenko image over the RTM image demonstrate that for field data, the Marchenko frame work is applicable and effective in suppressing the artifacts caused by internal multiples.

2.8 Acknowledgments

We appreciate the enlightening comments of Arthur Cheng, Joost van der Neut, Matteo Ravasi, Filippo Broggini, and an anonymous reviewer. We thank sponsors of the Center for Wave Phenomena, whose support made this research possible. The reproducible numeric examples in this paper use the Madagascar open-source software package (Fomel et al., 2013) freely available from http://www.ahay.org.

CHAPTER 3

ON THE TWO INPUTS FOR MARCHENKO REDATUMING: SURFACE SEISMIC DATA AND BACKGROUND VELOCITY MODEL

Xueyi (Alex) Jia[1], and Roel K. Snieder[1]

Prepared for submission to *Geophysics*.

3.1 Abstract

Marchenko redatuming and imaging requires two inputs: the seismic data acquired on the earth surface and a background velocity model, which is used to estimate first arrivals from subsurface locations to the surface. We investigate both inputs in order to elucidate the specific requirements for these inputs for field data applications. The input surface seismic data should be acquired in an idealised scenario where 1) equal numbers of seismic sources and receivers are used for acquisition 2) the depths and lateral positions of all sources and receivers are the same 3) both sources and receivers are placed on an uniform, regular and dense grid 4) the aperture of the sources and receivers is sufficiently large. A real field data acquisition rarely meets these requirements. We adopt the term "data regularization" to describe the process of placing the irregular and sparse data on a uniform and dense grid. Often, data interpolation is part of the data regularization for Marchenko redatuming. We investigate four forward interpolation methods: nearest neighbor interpolation, Lagrange interpolation, *Sinc* interpolation, and B-spline interpolation for both 2D and 3D data regularization. With a relatively simple trapezoidal structural model and a complex Gulf of Mexico synthetic model, we show that for 2D surface data with a realistic source and receiver spacing, even the nearest neighbor interpolation works sufficiently well for the integration over surface locations during Marchenko redatuming. These interpolation methods may produce errors at far offsets for complex models, but the errors are largely mitigated thanks to

[1]Center for Wave Phenomena, Colorado School of Mines, 1500 Illinois St., Golden, CO 80401, USA

the edge taper that is applied to far offsets at each iteration in the redatuming algorithm. For 3D data regularization, we show that the 8-point B-spline interpolation works fairly well for a relatively complex 2.5D Gulf of Mexico model while nearest neighbor interpolation produces significant errors. For the other input—the background velocity model, we clarify that it does not need to be known in great detail since the velocity model is merely used to estimate the first arriving waves. With two synthetic examples and an offshore Brazil field data example, we demonstrate that the combination of Marchenko redatuming and imaging is robust when an erroneous velocity model is used to estimate the first arrivals.

3.2 Introduction

The Marchenko redatuming algorithm (Broggini & Snieder, 2012; Broggini *et al.*, 2012; da Costa Filho *et al.*, 2014; Singh *et al.*, 2015a; Wapenaar *et al.*, 2014b) takes two inputs: the seismic reflection data that is recorded on the earth's surface and the first arrivals estimated from a background velocity. Both inputs need to satisfy certain criteria to be useful for Marchenko imaging. Practical questions, such as what kind of surface data the Marchenko method requires, how much detail the velocity model needs to include, and what happens if the velocity model is in error are relevant when applying Marchenko imaging to field data.

We first clarify the requirements for the surface data by the Marchenko redatuming algorithm. Unlike conventional imaging methods, which are quite compatible with data recorded in different acquisition geometries, the surface seismic data for the Marchenko redatuming algorithm need to be acquired in an idealised scenario. Modified from Ravasi (2019), we summarize the idealised scenario where the data satisfy the following criteria:

1) equal numbers of seismic sources and receivers are used for acquisition,

2) the depths and lateral positions of all sources and receivers are the same,

3) both sources and receivers are placed on a uniform, regular and dense grid,

4) the aperture of the sources and receivers i sufficiently large.

Such an ideal data acquisition scenario can be achieved in synthetic data simulations. In practice, however, seismic exploration data are often recorded with irregularly located

sources and receivers. The number of sources and receivers are not necessarily equal: for example, the number of receivers is usually three to four times larger than the number of sources for marine streamer data. Additionally, the source and receiver spacing is not necessarily dense: for 2D streamer data, the source spacing is sparser than the receiver spacing; and for 3D streamer data, the cross-line spacing is sparser than the in-line spacing. In this study, we adopt the term "data regularization" from Fomel (2000) to describe the process of making irregularly sampled seismic data to regular grids that meet the requirement for Marchenko redatuming. Seismic data regularization itself is a broad subject. Advanced algorithms, such as iterative model-space or data-space optimization, are used for 2D and 3D seismic data regularization (Fomel, 2000; Tikhonov *et al.*, 2013). Investigation of these sophisticated regularization techniques is beyond the scope of this study. We consider four forward interpolation approaches—nearest neighbor interpolation, Lagrange interpolation, *Sinc* interpolation and B-spline interpolation—for both 2D and 3D streamer type data. We then evaluate how the Marchenko redatuming works with the regularized data by these four interpolation methods. Although 3D seismic surveys, in which a designed grid layout of receivers and sources covering an area on the surface are used for acquisitions, have become standard for hydrocarbon exploration and production, regularization for 3D data remains a challenging topic. In this study, we investigate B-spline interpolation for the cross-line data reconstruction for a relative simply 3D acquisition scenario, where the in-line data sampling is dense and the cross-line data sampling is sparse. We first outline the formulation for the forward interpolation methods mentioned above. In the numerical experiments subsection, we compare and discuss the four interpolation methods using a simple 2D trapezoidal model and a complex 2D Gulf of Mexico model. We then test our 3D B-spline interpolation algorithm with a 2.5D Gulf of Mexico model.

We also address the questions around the velocity model required by the Marchenko method. The velocity model is used to estimate the first-arriving waves from the position where we want to create the virtual source to the acquisition surface. Since this first-arriving

wave is mostly determined by its travel time, only an estimate of the smooth velocity model is needed. Several field data examples (Jia *et al.*, 2017, 2018; Ravasi *et al.*, 2016; Staring *et al.*, 2017) have been published showing that a background or smooth velocity model, which is also needed for Reverse Time Migration, works sufficiently for Marchenko imaging. Yet, in practice it can be challenging to build an accurate smooth velocity model for complex areas, especially for deeper portions of the subsurface. When using an erroneous velocity, conventional imaging methods, such as Reverse Time Migration, map the reflections to shifted positions. Conventional imaging methods, such as RTM, still produce artifacts due to the internal multiples when an erroneous velocity model is used. Broggini *et al.* (2014b) demonstrated the robustness of the combination of Marchenko redatuming and imaging when using an erroneous velocity model with a synthetic example. In this study, we investigate this problem using a simple layered synthetic model and a complex Gulf of Mexico synthetic model. We also show a field data example where the Marchenko method eliminates the artifacts due to internal multiples despite the fact that deeper parts of the velocity model are inaccurate.

3.3 Forward interpolation methods

The equations for the Marchenko algorithm from Wapenaar *et al.* (2014b) in a three dimensional Cartesian coordinate system are solved iteratively and the iteration is given by,

$$M_k^+\big(\mathbf{r_0''},\mathbf{r}',-t\big) = \int_{\partial x_0}\int_{\partial y_0}\left(\int_{-t^d}^{t} R\big(\mathbf{r_0''},(x_0,y_0,0),t-t'\big)\cdot f_{1,k}^-\big((x_0,y_0,0),\mathbf{r}',-t'\big)dt'\right)dy_0dx_0, \quad (3.1)$$

and

$$f_{1,k+1}^-\big(\mathbf{r_0''},\mathbf{r}',t\big) = f_{1,0}^-\big(\mathbf{r_0''},\mathbf{r}',t\big)+ \int_{\partial x_0}\int_{\partial y_0}\left(\int_{-t^d}^{t} R\big(\mathbf{r_0''},(x_0,y_0,0),t-t'\big)\cdot M_k^+\big((x_0,y_0,0),\mathbf{r}',t'\big)dt'\right)dy_0dx_0, \quad (3.2)$$

with

$$f_{1,0}^{-}\big(\mathbf{r}_{\mathbf{0}}^{''},\mathbf{r}^{'},t\big) = \int_{\partial x_0}\int_{\partial y_0}\Big(\int_{-\infty}^{-t^d} R\big(\mathbf{r}_{\mathbf{0}}^{''},(x_0,y_0,0),t-t^{'}\big)\cdot T_d\big(\mathbf{r}^{'},(x_0,y_0,0),t^{'}\big)dt^{'}\Big)dy_0dx_0, \quad (3.3)$$

where k labels the iteration number, $\mathbf{r}_{\mathbf{0}}^{''} = (x_0^{''}, y_0^{''}, 0)$ represents a point located on the acquisition surface, and $\mathbf{r}^{'} = (x_i^{'}, y_i^{'}, z_i^{'})$ stands for a point located in the 3D earth model at the depth $z_i^{'}$. In these expressions R represents the seismic reflection response. Particularly, $R\big(\mathbf{r}_{\mathbf{0}}^{''},(x_0,y_0,0),t\big)$ represents the reflection response corresponding to a source at the surface location $\mathbf{r}_{\mathbf{0}}^{''}$ and a receiver at the surface location $(x_0, y_0, 0)$, at time t. The one-way travel time of the first arrival from a subsurface focusing location at $(x_i^{'}, y_i^{'}, z_i^{'})$ to a surface location $(x_0, y_0, 0)$ is represented by t^d. Using S to represent the source wavelet and D to represent the recorded surface data, the surface reflection response, deconvolved with the source wavelet, is given by $R = S^{-1} * D$, where $*$ represents temporal convolution. Readers are referred to Wapenaar *et al.* (2014b) for the detailed physical meaning of M_k^{+}, $f_{1,k}^{-}$, and T_d.

Since the 3D Marchenko equations involve spatial integrations along x and y axes, the surface data R should be sampled uniformly and densely. For modern 2D seismic surveys, the receiver spacing is usually dense (e.g. 12.5 m or 25.0 m), however, the source spacing can be sparse, typically threefold or fourfold of the receiver spacing (e.g. 37.5 m or 100.0 m). Thus, the gap in sources need to be interpolated. For 3D marine streamer seismic surveys, the source and receiver sampling along in-line direction is dense (e.g. 25.0 m), but the cross-line source sampling is sparse, approximately fourfold of the in-line spacing (e.g. 100.0 m). In order to make 3D marine data meet the requirements of 3D Marchenko imaging (in other words, to accurately evaluate the integrations in equations (3.1), (3.2), and (3.3) with a 3D streamer dataset), we need to conduct data interpolation along the cross-line direction.

The general form of a linear forward interpolation operator is

$$f(x) = \sum_{n\in N} W_n(x) f_n, \quad (3.4)$$

where n is a point on a given regular grid N, x is a point in the continuum, $f(x)$ is the reconstructed continuous function, and $W_n(x)$ is a linear weight. This form can be generalized to multi-dimensions.

One classic example of the interpolation weight $W(x, n)$ for data sampled at points $x_n = n$ is the Lagrange polynomial, which has the form

$$W_n(x) = \coprod_{i \neq n} \frac{x - i}{n - i}. \tag{3.5}$$

Lagrange interpolation provides a unique polynomial, which goes exactly through the data points $f(n)$. The local 1-point Lagrange interpolation is equivalent to the nearest-neighbor interpolation, defined by

$$W(x, n) = \begin{cases} 1, & \text{for} \quad n - 1/2 < x \leq n + 1/2 \\ 0, & \text{otherwise.} \end{cases} \tag{3.6}$$

Because of its simplicity, nearest-neighbor interpolation is easy to apply. Its accuracy is limited and may be inadequate for interpolating high-frequency signals. Its interpolant acts as low-pass filters, preventing the high-frequency energy from being correctly interpolated.

Lagrange interpolants of higher order correspond to more complicated polynomials. Another popular practical approach is cubic convolution (Keys, 1981). The cubic convolution interpolant is a local piece-wise cubic function:

$$W_n(x) = \begin{cases} 3/2|x - n|^3 - 5/2|x - n|^2 + 1, & \text{for} \quad 0 \leq |x - n| < 1 \\ -1/2|x - n|^3 + 5/2|x - n|^2 - 4|x - n| + 2, & \text{for} \quad 1 \leq |x - n| < 2 \\ 0, & \text{otherwise.} \end{cases} \tag{3.7}$$

We test 8-point cubic convolution interpolant in the following numerical examples. Note the cost of interpolation grows proportionally to the interpolant length.

A well-known interpolation method, the Shannon *Sinc* interpolation, consists of a weighting function

$$W_n(x) = \frac{sin[\pi(x - n)]}{\pi(x - n)}. \tag{3.8}$$

Shannon *Sinc* interpolation provides an optimal interpolation for band-limited signals (Kotel'nikov, 1933; Shannon, 1949), but the slow decay with (x -n) of its practical implementation results in expensive computation. This problem is solved in practice using the Kaiser window (Kaiser and Shafer, 1980), which has the form

$$W_n(x) = \begin{cases} \dfrac{sin[\pi(x-n)]}{\pi(x-n)} \dfrac{I_0(a\sqrt{1-(\frac{x-n}{N})^2})}{I_0(a)}, & \text{for} \quad n-N < x < n+N \\ 0, \quad \text{otherwise}, \end{cases} \tag{3.9}$$

where I_0 is the zero-order modified Bessel function of the first kind. The Kaiser-windowed *Sinc* interpolant in equation 3.9 has the adjustable parameter a, which controls the behavior of its spectrum.

One general approach to construct the weighting function in equation 3.4 is to select an appropriate basis to represent the function $f(x)$. The basis function expansion takes the form

$$f(x) = \sum_{k \in K} c_k \psi_k(x), \tag{3.10}$$

where $\psi_k(x)$ are basis function, and c_k are the corresponding coefficients. The interpolant $W_n(x)$ can be defined with the least-squares method, once an appropriate basis is selected.

For B-spline interpolation, we select a convolutional basis in such way that the B-spline $\beta^n(x)$ of an order n is defined by a repetitive spatial convolution of the zeroth-order spline $\beta^n(x)$ (the boxcar function) with itself:

$$\beta^n(x) = \beta^0(x) * ... * \beta^0(x). \tag{3.11}$$

Hence, the B-spline basis satisfies equation

$$\psi_k(x) = \beta(x-k). \tag{3.12}$$

Substituting equation 3.12 into equation 3.10 yields

$$f(x) = \sum_{k \in K} c_k \beta(x-k). \tag{3.13}$$

Evaluating the function $f(x)$ in equation 3.13 at a sampling point n yields,

$$f_n = \sum_{k \in K} c_k \beta(n-k), \tag{3.14}$$

which leads to the exact form of a discrete convolution. We can invert equation 3.14 to obtain the coefficients c_k from $f(n)$ by means of deconvolution. With the B-spline convolutional basis, forward interpolation becomes a two-step procedure: (1) obtain the basis coefficients c_k by deconvolving the sampled function $f(n)$ with the factorized filter $\beta(n)$ based on equation 3.14, and (2) reconstructs function $f(x)$ according to equation 3.13.

The explicit expression of the B-spline basis is (Fomel, 2000)

$$\beta^n(x) = \frac{1}{n!} \sum_{k=0}^{n+1} C_k^{n+1} (-1)^k (x + \frac{n+1}{2} - k)_+^n, \tag{3.15}$$

where C_k^{n+1} are the binomial coefficients and the function x_+ is defined as: for $x > 0$, $x_+ = x$, otherwise $x_+ = 0$. The B-spline interpolation method is proven to be accurate and efficient for interpolating regularly spaced data, and B-spline interpolation leads to a faster convergence in under-determined problems and a more accurate result in over-determined problem in comparison with other linear interpolation methods, such as the nearest neighbor interpolation and *Sinc* interpolant (Fomel, 2000).

3.4 Data regularization: 2D and 3D numerical examples

In this section, we investigate the data interpolation methods for Marchenko redatuming with two 2D synthetic examples with 1) a trapezoidal model and 2) a Gulf of Mexico model. We demonstrate that for 2D cases and for the used sampling intervals Marchenko redatuming is robust with these forward interpolation methods. We then test B-spline interpolation for 3D data regularization with a 2.5D Gulf of Mexico model.

3.4.1 2D Trapezoidal model

We show the velocity and density model of the trapezoidal model in Figure 3.6a and Figure 3.6b, respectively. The grid for the model is 10 m in x-direction and 10 m in z-

direction. We use 101 shots at depth $z = 0\ m$ and the same number of receivers to generate the ideal surface dataset. A shot gather with a source located at $x = 0\ m$ and $z = 0\ m$ is shown in Figure 3.2a. The direct arrival is removed from the shot gather and a free surface boundary condition is not adopted when simulating the data; therefore, the first two hyperbolic events are primaries reflected from the two interfaces and the following hyperbolic events are internal multiples. To mimic a sparse and practical surface data acquisition, we sub-samped the source/receiver spacing to 40 m. A surface shot gather recorded with such a sparse acquisition geometry is shown in Figure 3.2b.

We use the following four 2D forward interpolation methods for data interpolation for each shot gather: nearest neighbor interpolation, the 8-point Lagrange interpolation, the 8-point *Sinc* interpolation, and B-spline interpolation. We show the comparison of an interpolated surface shot record using these four interpolation methods for this trapezoidal model in Figure 3.3. We show the interpolated surface shot gathers in Figure 3.3a, Figure 3.3c, Figure 3.3e, and Figure 3.3g, and the difference between the interpolated shot gather and the reference shot gather in Figure 3.3b, Figure 3.3d, Figure 3.3f, and Figure 3.3h, respectively. Nearest neighbor interpolation generates relatively large residuals. The other three methods work fairly well and B-spline interpolation generates least amount of residuals and is the most computationally effective.

We first perform Marchenko redatuming with the densely sampled surface data (Figure 3.2) and a background velocity model. The virtual source is located at $x = 0\ m$ and $z = 800\ m$. The retrieved Green's function is shown in Figure 3.4b, which should be equivalent to a shot gather with source at $x = 0\ m$ and $z = 800\ m$ and receivers on the surface at $z = 0\ m$. For this trapezoidal synthetic model, we simulate such a shot gather directly with finite-difference modeling (Figure 3.4a). The retrieved Green's function matches well with the direct simulation.

In order to check how the interpolation methods work for Marchenko redatuming, with the interpolated surface shot data obtained by the four interpolation methods and a back-

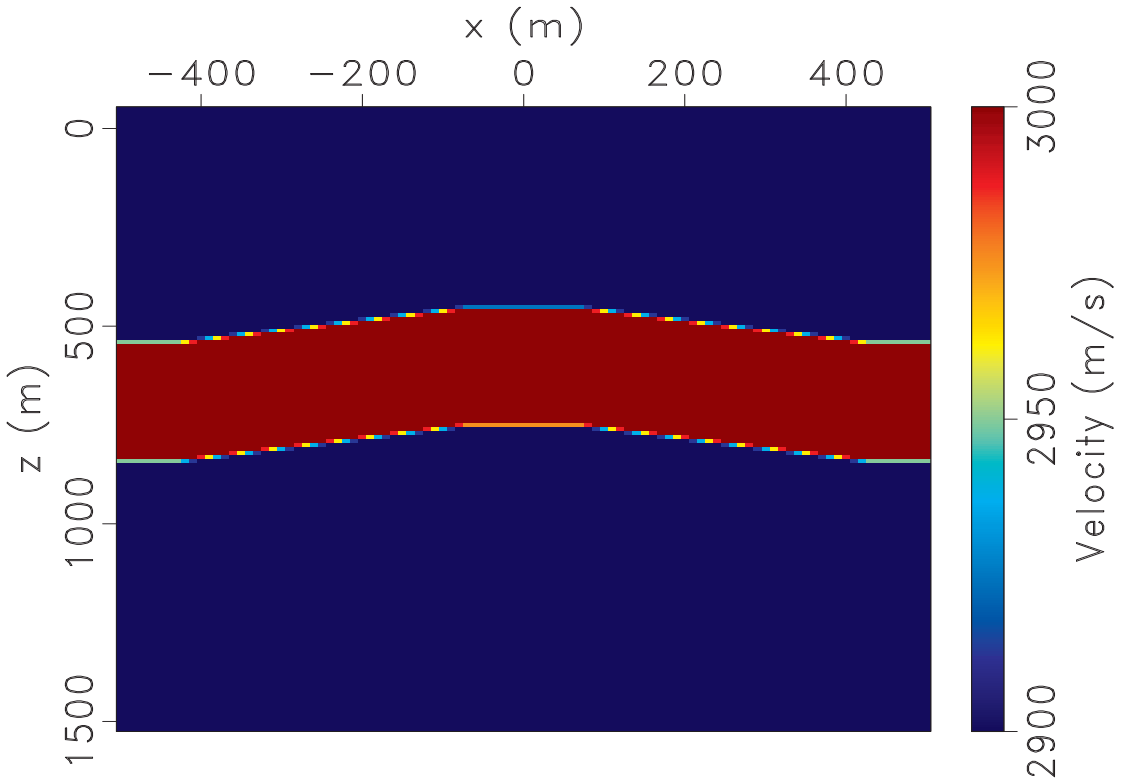

(a)

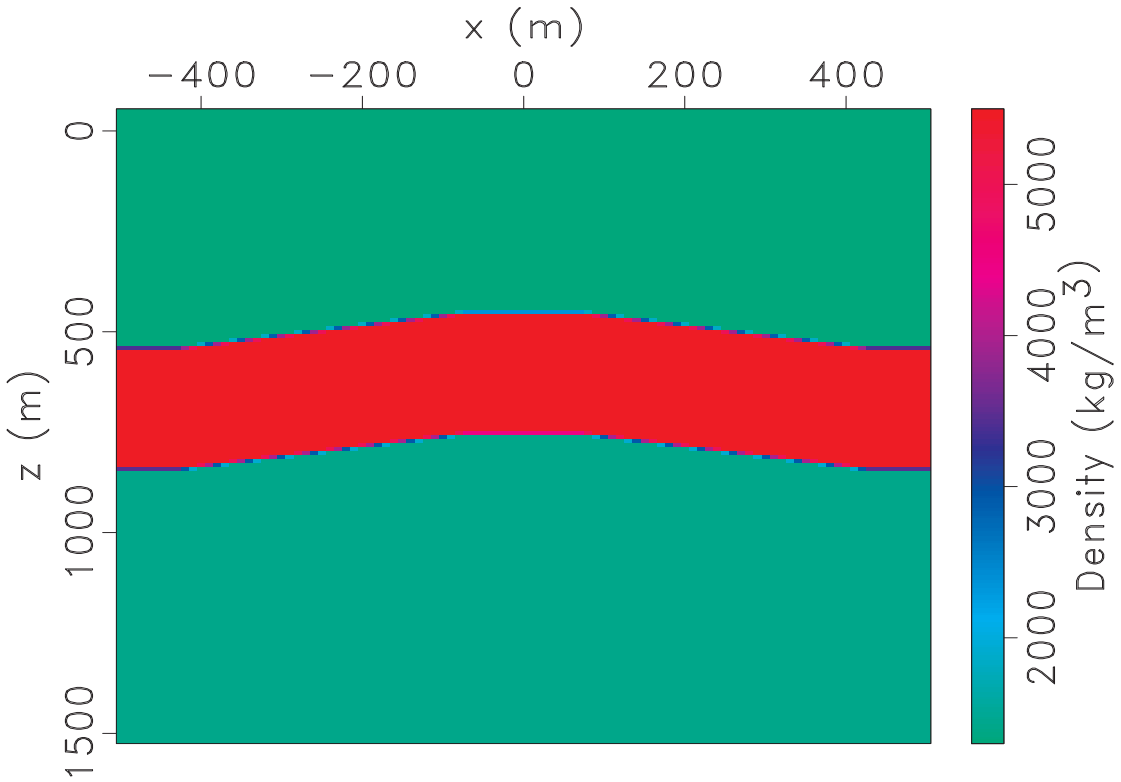

(b)

Figure 3.1: The velocity (panel a) and density (panel b) of the trapezoidal synthetic model.

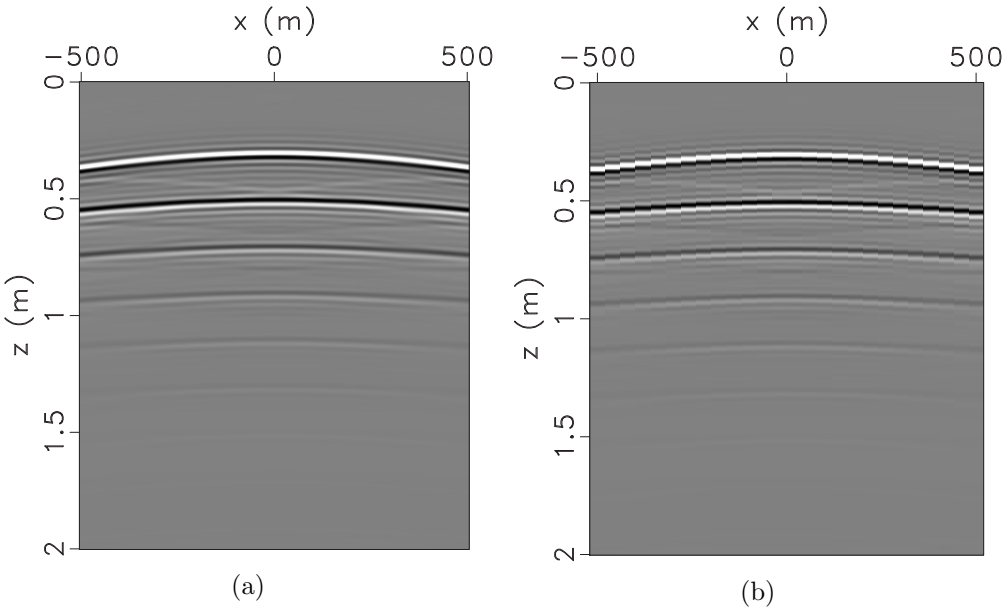

Figure 3.2: A surface shot gather simulated with the trapezoidal model for a dense sampling of 10 m (panel a), and a sparse sampling of 40 m (panel b).

ground velocity model, we perform the Marchenko Green's function retrieval and compare the results with the reference Green's function, which is the Green's function retrieved with the densely sampled surface data (Figure 3.4b). We show the retrieved Green's function from a virtual source at $x = 0\ m$ and $z = 800\ m$ to the surface with the surface data reconstructed with the four methods in Figure 3.5a, Figure 3.5c, Figure 3.5e, and Figure 3.5g, and the difference between them and the reference Green's function in Figure 3.5b, Figure 3.5d, Figure 3.5f, and Figure 3.5h, respectively. For this relatively simple synthetic model, all methods work well and generate negligible residuals or errors. Even nearest neighbor interpolation produces an accurate Green's function. This is because the Marchenko algorithm involves the process of surface integration, and the associated averaging supresses the interpolation errors. Moreover, during the calculation of the surface integration, a edge taper is applied resulting in the elimination of the interpolation errors at large offsets.

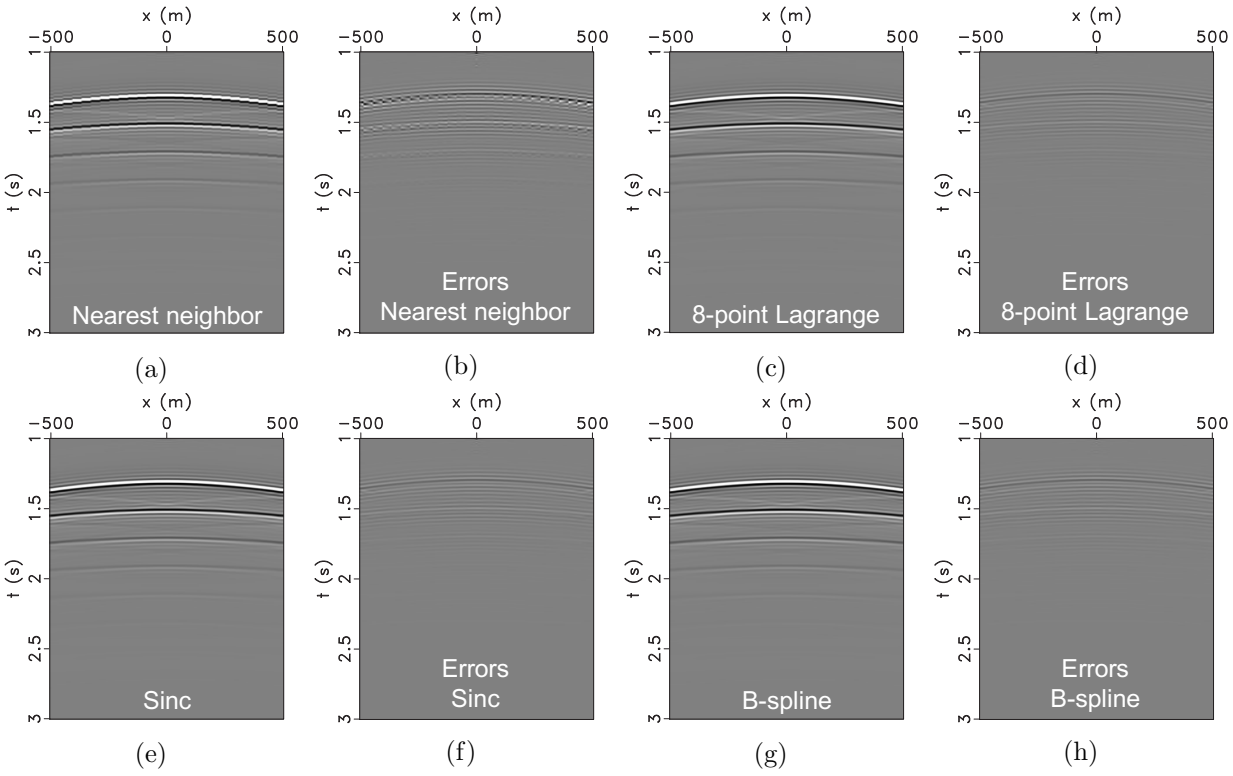

(a) (b) (c) (d)

(e) (f) (g) (h)

Figure 3.3: A comparison of an interpolated surface shot record using different interpolation methods for the trapezoidal model: (a) nearest neighbor interpolation, (b) The difference between (a) and the reference surface shot record, (c) 8-point Lagrange interpolation, (d) The difference between (c) and the reference surface shot record. (e) 8-point *Sinc* interpolation, (f) The difference between (e) and the reference surface shot record, (g) 8-point B-spline interpolation, (h) The difference between (g) and the reference surface shot record.

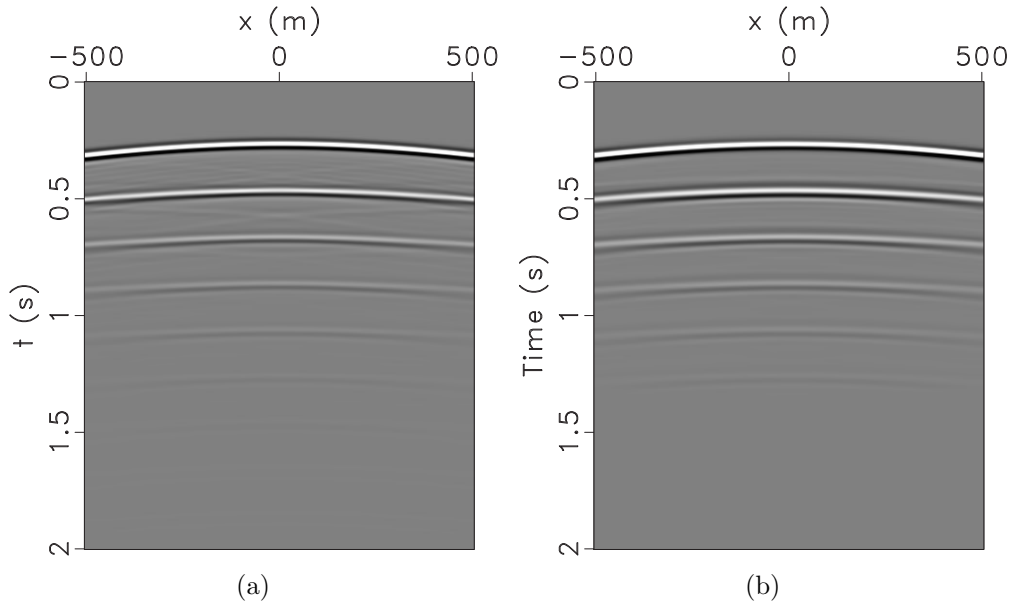

(a) (b)

Figure 3.4: (a) Directly simulated Green's function from a subsurface location at $x = 0$ m and $z = 800$ m to surface receivers. (b) Green's function retrieved with Marchenko redatuming using regular and dense surface data.

3.4.2 2D Gulf of Mexico model

In this synthetic experiment, we test the four interpolation methods with a more complex model, which is inspired by a Gulf of Mexico dataset. This model contains a salt body in the sallow parts with rugose interfaces, and a number of horizontal subsalt targets in the density. Severe internal multiples are generated by the water bottom and the salt body. We show the velocity and density of the Gulf of Mexico model in Figure 3.6a and Figure 3.6b, respectively. The grid for the model is 4 m in x-direction and 4 m in z-direction. We use 262 shots at depth $z = 0$ m and the same number of receivers to generate the ideal surface dataset. A shot gather with source located at $x = 1500$ m and $z = 0$ m is shown in Figure 3.7a. For a sparse data acquisition where the source/receiver sampling is 40 m, a surface shot gather is shown in Figure 3.7b.

We perform data interpolation with four forward interpolation methods used in the previous example. We show the comparison of an interpolated surface shot record using these four interpolation methods for the Gulf of Mexico model in Figure 3.8. The interpolated

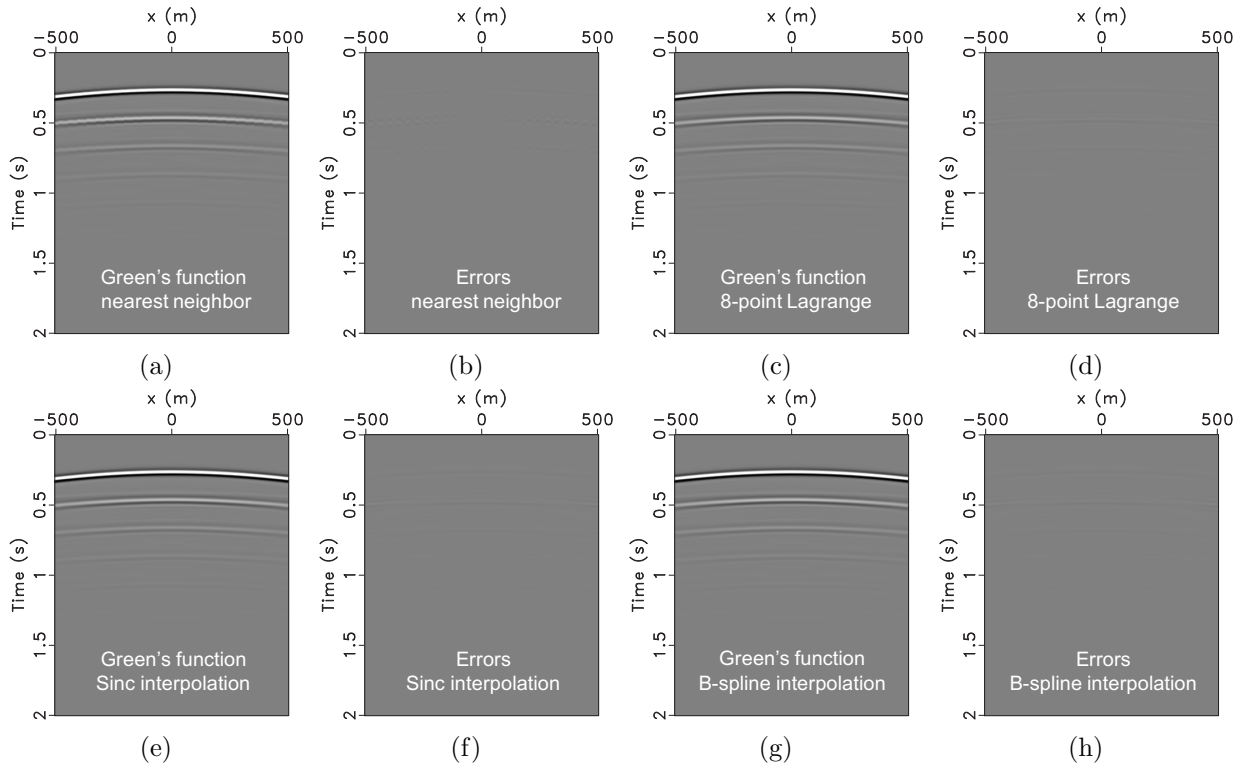

Figure 3.5: A comparison of the Green's function retrieved by different interpolation methods for the trapezoidal model: (a) Green's function retrieved with the interpolated surface data by nearest neighbor interpolation for a virtual source at $x = 0\ m$ and $z = 800\ m$, (b) The difference between (a) and the reference Green's function, (c) Green's function retrieved with the interpolated surface data by 8-point Lagrange interpolation, (d) The difference between (c) and the reference Green's function, (e) Green's function retrieved with the interpolated surface data by 8-point *Sinc* interpolation, (f) The difference between (e) and the reference Green's function, (g) Green's function retrieved with the interpolated surface data by 8-point B-spline interpolation, (h) The difference between (g) and the reference Green's function.

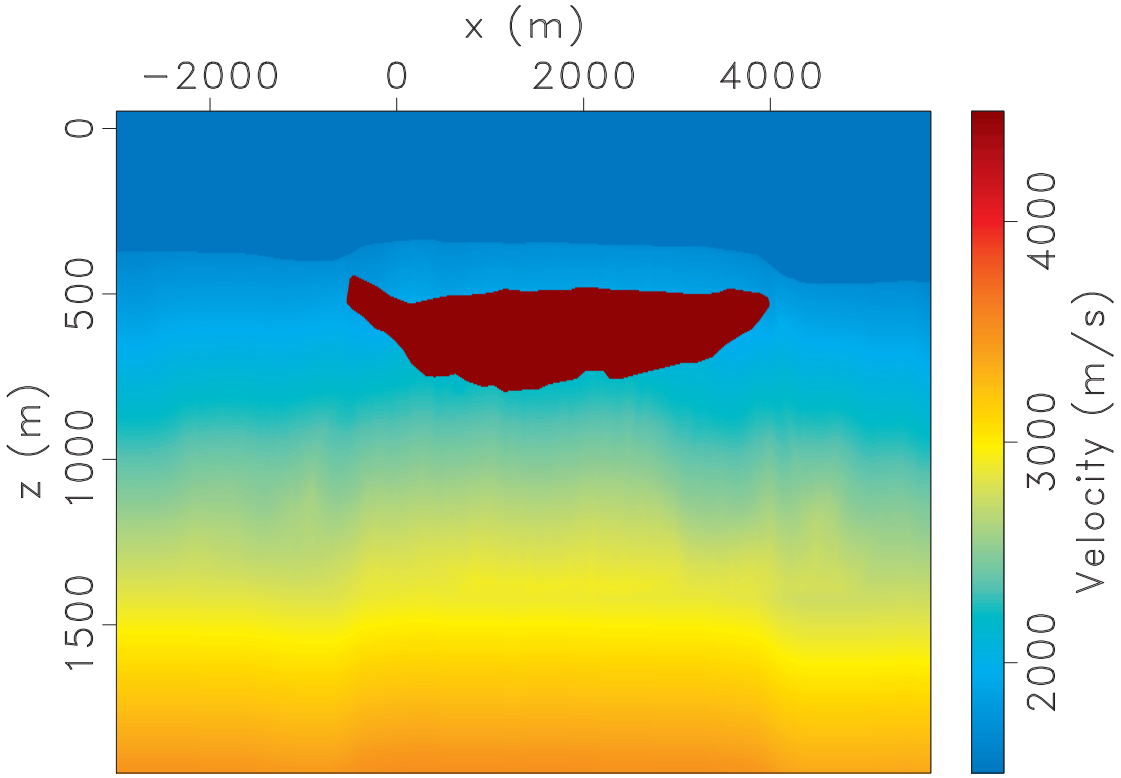

(a)

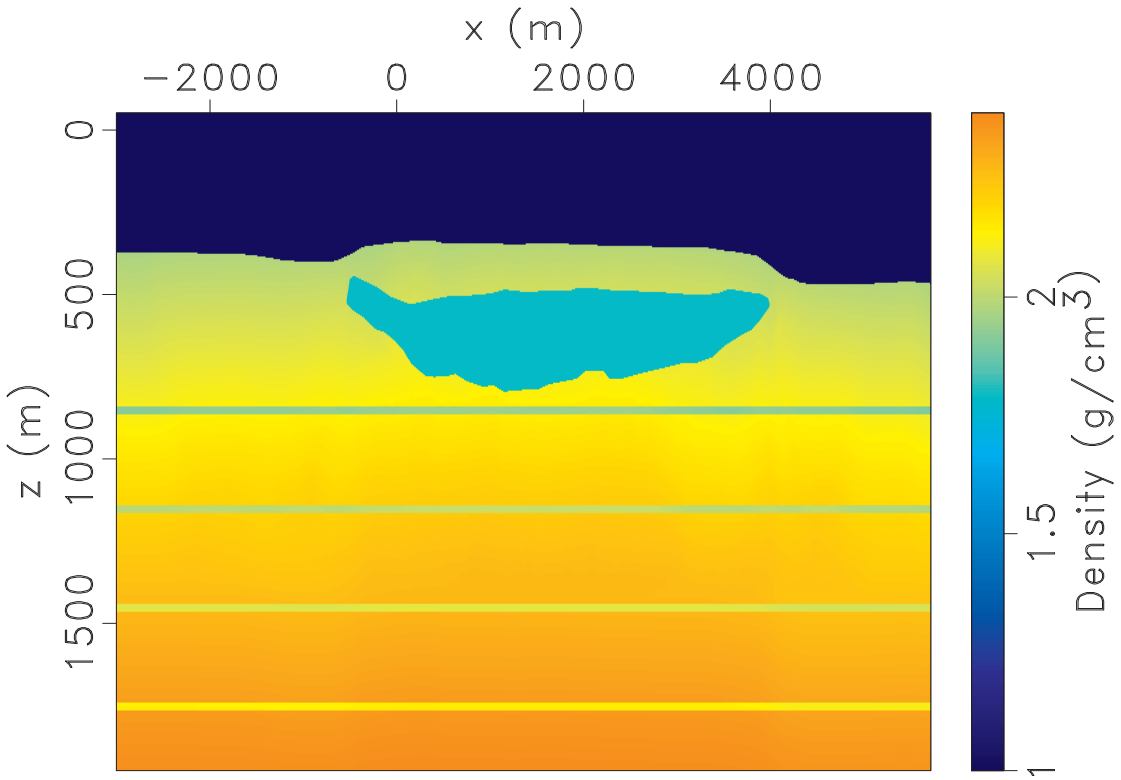

(b)

Figure 3.6: The velocity (panel a) and density (panel b) of the Gulf of Mexico synthetic model.

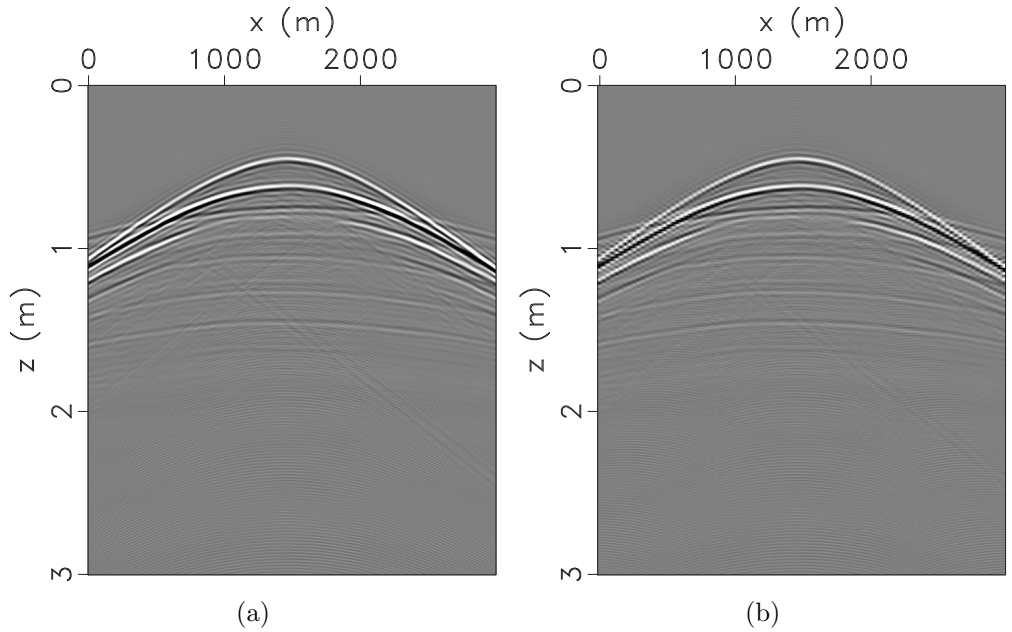

Figure 3.7: A surface shot gather simulated with the Gulf of Mexico model for a dense sampling of 10 m (panel a), and a sparse sampling of 40 m (panel b).

surface shot gathers are shown in Figure 3.8a, Figure 3.8c, Figure 3.8e, and Figure 3.8g, and the difference between the interpolated shot gathers and the reference shot gather are shown in Figure 3.8b, Figure 3.8d, Figure 3.8f, and Figure 3.8h, respectively. The nearest neighbor interpolation method generates relatively large residuals. The other three methods work fairly well but more residuals are generated at far offsets for all the interpolation methods, because of the larger dip of the hyperbolas at far offsets. Again, B-spline interpolation generates the least amount of residuals and is the most computationally effective.

We apply Marchenko redatuming with the densely sampled dataset and the interpolated datasets by the four methods. First we show a comparison of the directly simulated Green's function from a subsurface location at $x = 1500\ m$ and $z = 1600\ m$ to surface receivers from $x = 0\ m$ to $x = 3000\ m$ (Figure 3.9a) with the Green's function retrieved with Marchenko redatuming using the densely sampled dataset (Figure 3.9b). The Green's function retrieved with the densely sampled dataset matches well with the direct simulated Green's function.

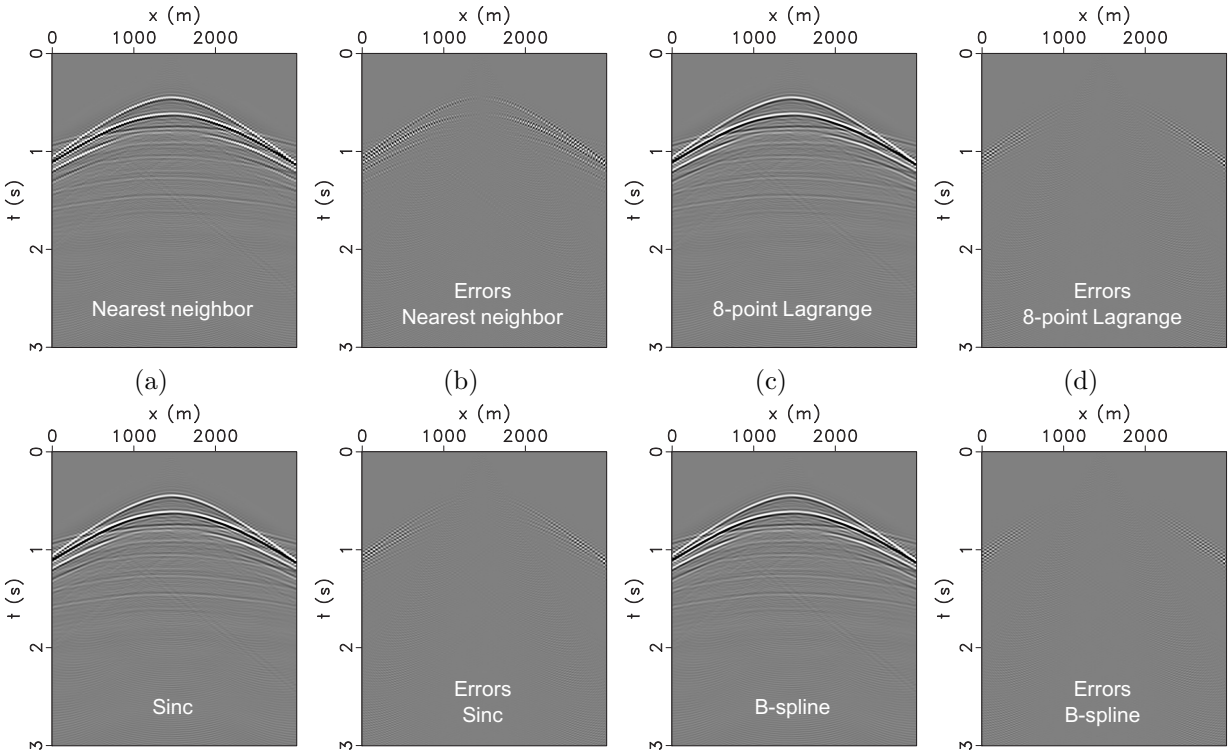

Figure 3.8: A comparison of an interpolated surface shot record using different interpolation methods for the Gulf of Mexico model: (a) nearest neighbor interpolation, (b) The difference between (a) and the reference surface shot record, (c) 8-point Lagrange interpolation, (d) The difference between (c) and the reference surface shot record. (e) 8-point *Sinc* interpolation, (f) The difference between (e) and the reference surface shot record, (g) 8-point B-spline interpolation, (h) The difference between (g) and the reference surface shot record.

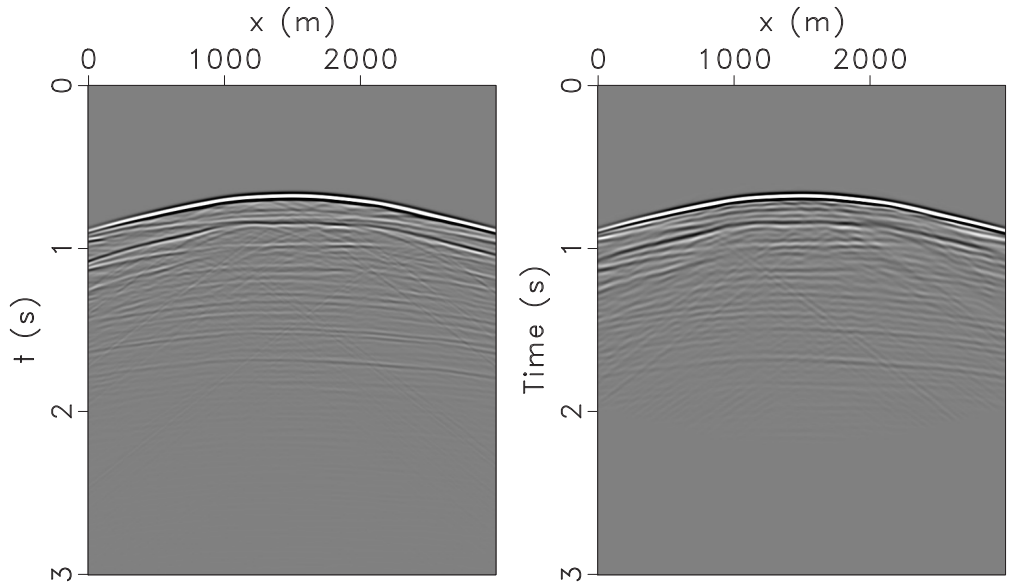

(a) (b)

Figure 3.9: (a) Directly simulated Green's function from a subsurface location at $x = 1500$ m and $z = 1600$ m to surface receivers from $x = 0$ m to $x = 3000$ m. (b) Green's function retrieved with Marchenko redatuming using regular and dense surface data.

We show the Green's functions retrieved with the interpolated datasets from the virtual source at $x = 1500$ m and $z = 1600$ m to the surface in Figure 3.10a, Figure 3.10c, Figure 3.10e, and Figure 3.10g, and the difference between them and the reference Green's function in Figure 3.10b, Figure 3.10d, Figure 3.10f, and Figure 3.10h, respectively. For this relatively complex model, all methods still work well and generate small residuals. Because of the edge taper that is applied during the calculation of the surface integration in the Marchenko algorithm, the large offset errors in the interpolated surface shot gathers are largely mitigated.

3.4.3 2.5D Gulf of Mexico Model

In this numerical experiment, we test our 3D Marchenko algorithm and 3D data interpolation algorithm with a 2.5D Gulf of Mexico model. Figure 4.7a and Figure 4.7b show the velocity and the density of the 2.5D Gulf of Mexico model. This model is referred to as a 2.5D model as it is created by extending a 2D Gulf of Mexico model along another

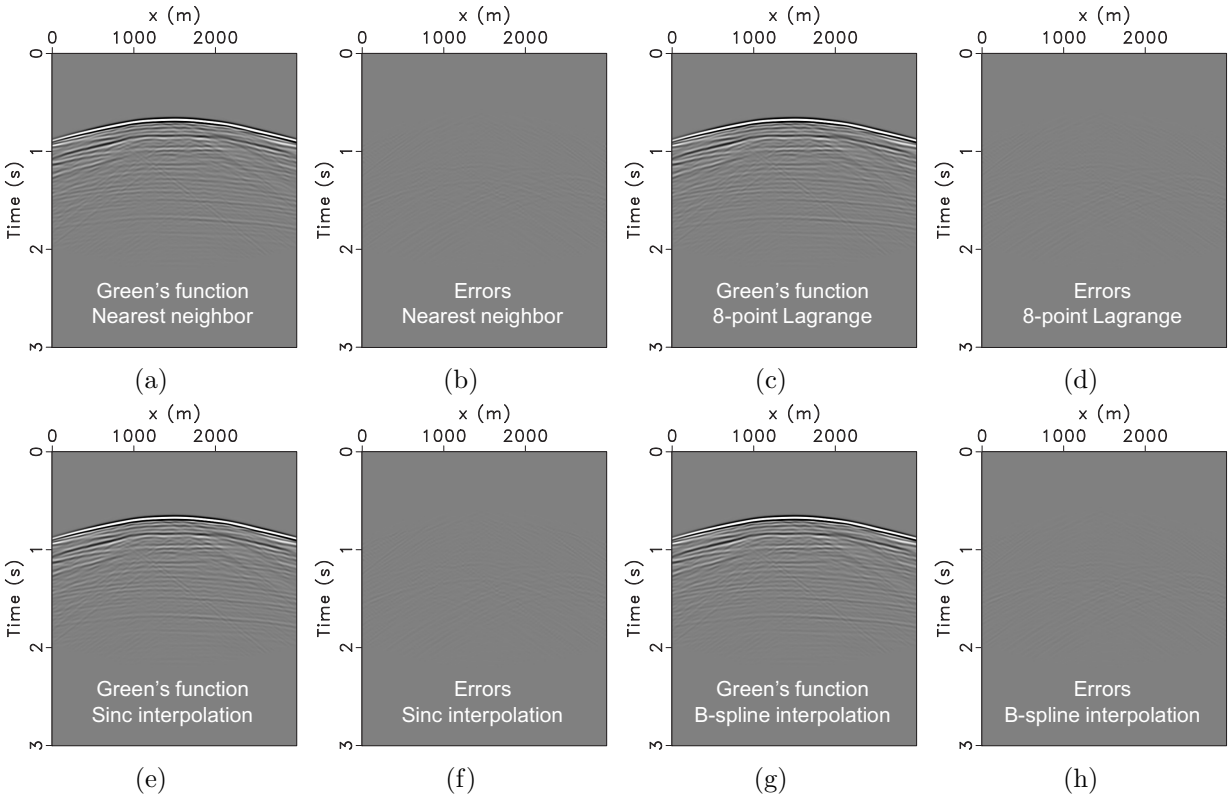

Figure 3.10: A comparison of the Green's function retrieved by different interpolation methods for the Gulf of Mexico model: (a) Green's function retrieved with the interpolated surface data by nearest neighbor interpolation for a virtual source at $x = 1500\ m$ and $z = 1600\ m$, (b) The difference between (a) and the reference Green's function, (c) Green's function retrieved with the interpolated surface data by 8-point Lagrange interpolation, (d) The difference between (c) and the reference Green's function, (e) Green's function retrieved with the interpolated surface data by 8-point *Sinc*, (f) The difference between (e) and the reference Green's function, (g) Green's function retrieved with the interpolated surface data by 8-point B-spline interpolation, (h) The difference between (g) and the reference Green's function.

horizontal axis - the y-axis. We use this model as a proof of concept and we benefit from the 2.5D geometry for the following reasons: 1) The reduction of the computational costs for data generation—we can create all the 3D shot gathers over a large surface area by generating the 3D surface shot records along one line (for example, the line $y = 0\ m$) and use transnational invariance in the y-direction to create all other surface 3D shot gathers. 2) The simplicity of analyzing and interpreting the reconstructed Green's function results as there are no out-of-plane reflections. The grid of the model is 10 m by 10 m by 10 m along x (in-line), y (cross-line), and z (depth). For the surface data simulation, the spacing between neighboring sources/receivers is set to 20 m along both cross-line and in-line directions. We aim to retrieve the Green's function between a subsurface point at ($x = 0\ m$, $y = 0\ m$, and $z = 1500\ m$) and the earth's surface.

For operability and cost considerations, 3D seismic data are rarely acquired with fully, densely and regularly sampled surveys. Three typical seismic data acquisition patterns, marine towed-steamer data, land data, and ocean-bottom data, have different acquisition characteristics. In this study, we choose to apply our 3D Marchenko algorithm with marine 3D towed-streamer type of seismic data. In a marine 3D towed-streamer seismic survey, data are acquired by survey vessels that traverse an area of the ocean following a series of parallel lines, trailing air gun arrays and hydrophone streamers as long as tens of kilometers (Figure 4.8). We assume that the dataset acquired from a modern 3D marine survey contains, 1) long offsets along the in-line directions, and 2) dense spatial sampling along the in-line direction (e.g. 12.5 m). However, the spacing of hydrophones along the cross-line direction is usually sparse (fourfold or more of the in-line spacing). As shown in equations 3.1 and 3.2, the 3D Marchenko algorithm involves the integration over an aperture of temporal convolutions and temporal cross-correlations of pairs of traces; therefore, both the in-line and cross-line sampling density should be sufficiently fine to avoid aliased energy contaminating the stacked trace. The desired sampling of the recorded data is determined by the aliasing condition: having at least four samples for the smallest wavelength. Therefore, interpolation is needed

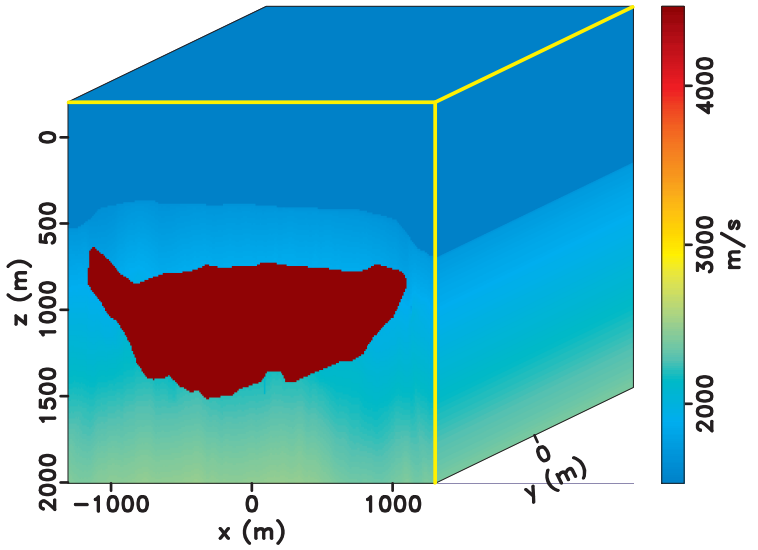

(a)

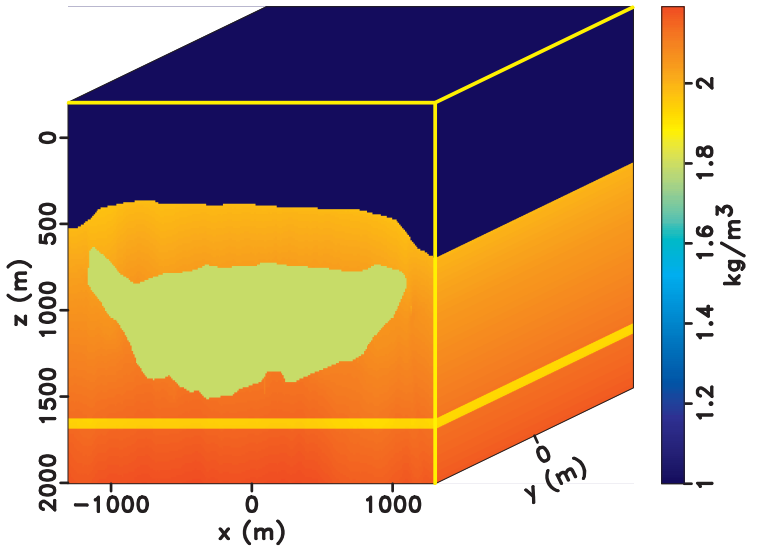

(b)

Figure 3.11: The 2.5D Gulf of Mexico velocity model (panel a) and density model (panel b).

to overcome the sparse spatial sampling in the cross-line direction. In this study, we use B-spline forward interpolation to obtain densely sampled shot gathers from sparse surface data. For comparison we also use nearest neighbor interpolation. We apply 2D nearest neighbor interpolation and 8-point B-spline interpolation at each time section.

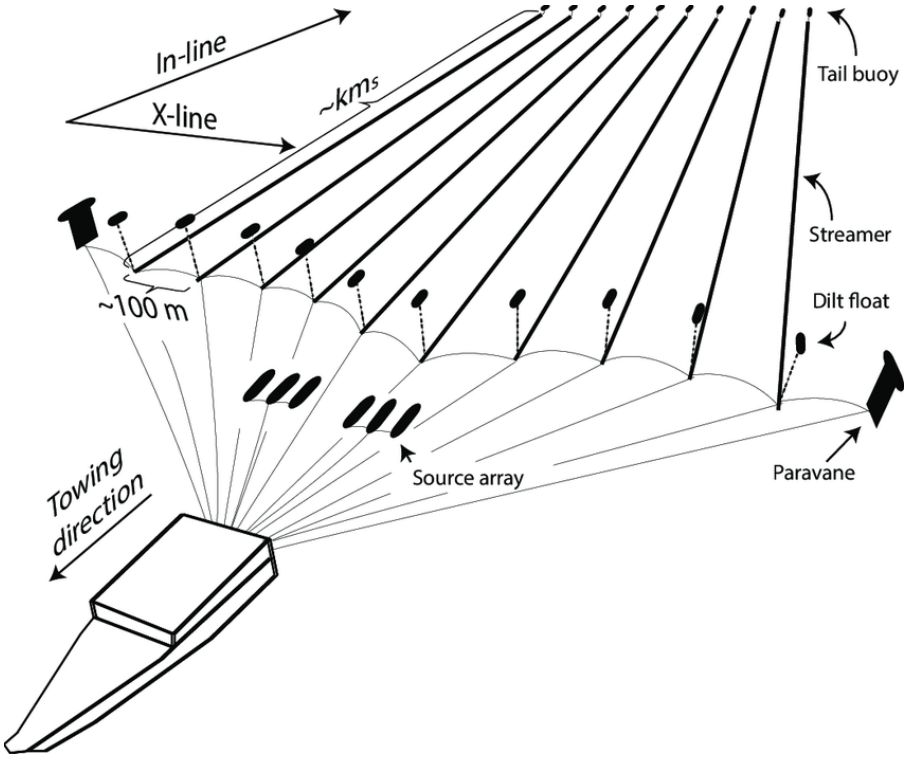

Figure 3.12: Geometry of a standard towed streamer survey.

Figure 4.9a shows a 3D surface shot gather with densely sampled receivers along both in-line and cross-line directions (10 m by 10 m). We sub-sample the reference surface shot gather in both the in-line and cross-line directions to obtain a sparse shot gather shown in Figure 4.9b. As a preliminary test for our interpolation algorithm for 3D surface data, we make both in-line and cross-line sampling sparse. We show the interpolated 3D surface shot gathers by nearest neighbor interpolation and 8-point B-spline interpolation in Figure 4.9c and Figure 4.9d, respectively. To evaluate how the interpolation algorithms work, we show time slices of the 3D shot cubes. Figure 3.14 shows that nearest neighbor interpolation produces a considerable amount of errors for the data regularization of a 3D shot gather.

We compare three time slices at t=0.52 s, 0.68 s, and 1.00 s between the original densely-sampled shot gather and the interpolated shot gather by nearest neighbor interpolation. The error panels for t=0.52 s, 0.68 s, and 1.00 s due to interpolation are shown in Figure 3.14d, Figure 3.14h, and Figure 3.14l, respectively.

We show the interpolation results of B-spline interpolation in Figure 4.10. Similar to Figure 3.14, the three panels in the last column (Figure 4.10d, Figure 4.10h, and Figure 4.10l) depict the errors generated by B-spline interpolation at t=0.52 s, 0.68 s, and 1.00 s, respectively. These three panels indicate that interpolation errors from B-spline interpolation are considerably less compared to nearest neighbor interpolation and most residuals appear at far offsets. As discussed earlier, far offset errors can be further suppressed by the edge taper applied at the Green's function retrieval stage.

We retrieve the Green's function from a virtual source at $x = 0\ m$, $y = 0\ m$, and $z = 1500\ m$ to all the surface grid points. For this 2.5D model, the salt structure appears only along the x-direction and the layers are flat in the y-direction. We use a 2D slice of the 3D Green's function in the plane $y = 0\ m$ to demonstrate the signature of the 3D Green's function. Figure 4.11a shows the in-line Green's function section simulated with 3D finite difference modeling with a source at $x = 0\ m$, $y = 0\ m$, and $z = 1500\ m$ and receivers along $y = 0\ m$. Figure 4.11b shows the Green's function retrieved by 3D Marchenko redatuming algorithm with the densely sampled surface data and a background velocity model. Figure 4.11c shows the Green's function retrieved by the 3D Marchenko redatuming algorithm with the sub-sampled surface data. With the sparsely sampled data as input, 3D Marchenko redatuming produces the Green's function that is severely aliased.

Figure 3.17a shows the in-line section of the 3D Green's function retrieved by Marchenko redatuming with the 3D surface dataset interpolated by nearest neighbor interpolation. The difference between Figure 3.17a and the reference Green's function Figure 4.11b is shown in Figure 3.17b. Since nearest neighbor interpolation produce large errors in the interpolated surface data, the retrieved 3D Green's function also contains significant errors with respect

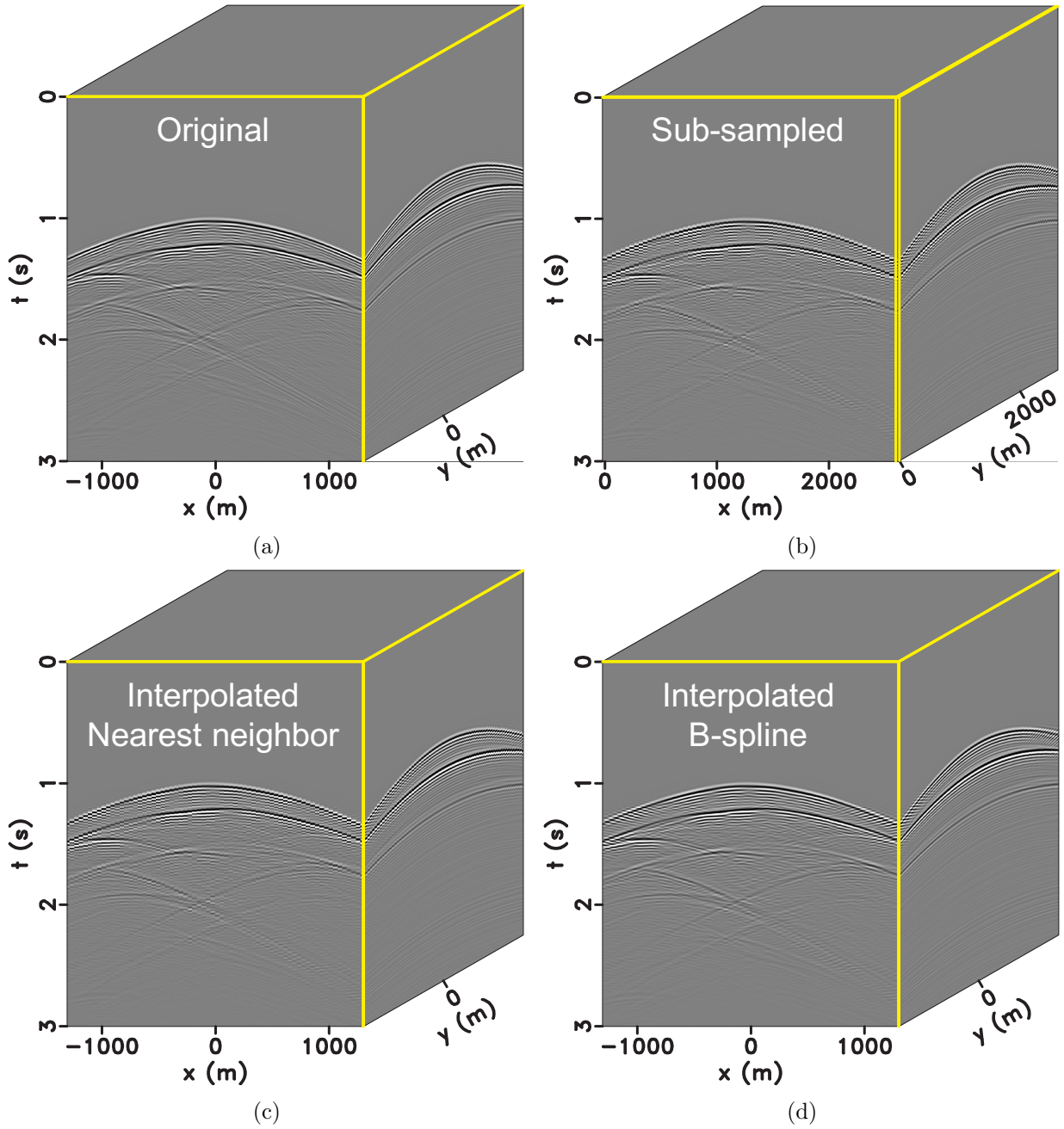

Figure 3.13: (a) A 3D surface shot gather with dense in-line and cross-line sampling. (b) Sub-sampled surface shot gather with sparse in-line and cross-line sampling. (c) Interpolated surface shot gather using nearest neighbor interpolation. (d) Interpolated surface shot gather using 8-point B-spline interpolation.

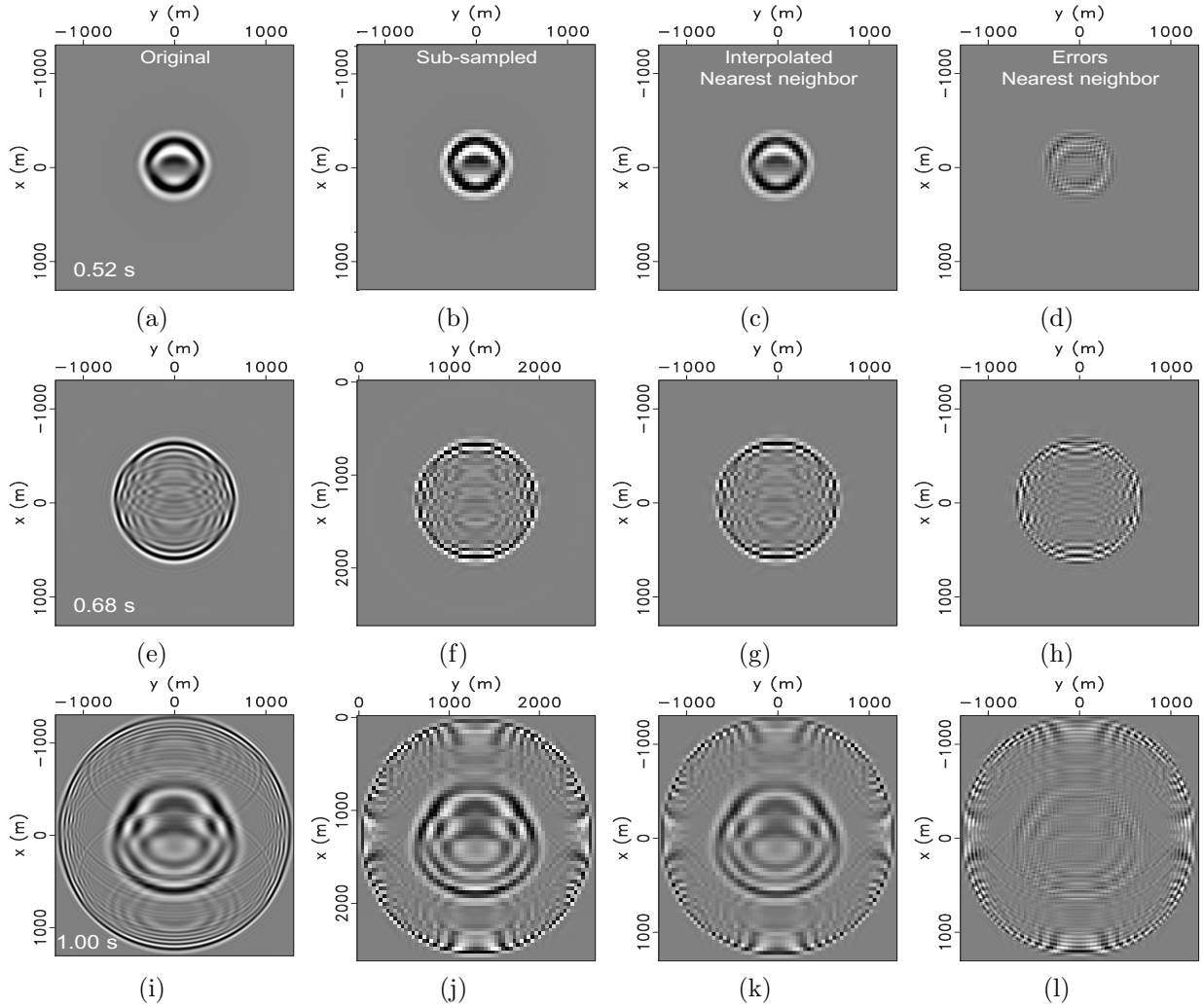

Figure 3.14: Nearest neighbor interpolation: Panels a, e, and i show the time slices of the directly simulated surface gather for 0.52 s, 0.68 s, and 1.00 s, respectively. Panels b, f, and j show the time slices of the sparse surface gather for 0.52 s, 0.68 s, and 1.00 s, respectively. Panels c, g, and k show the time slices of the interpolated surface gather by nearest neighbor interpolation for 0.52 s, 0.68 s, and 1.00 s, respectively. Panels d, h, and l depict the differences between the interpolated surface gather and the direct simulated surface gather at 0.52 s, 0.68 s, and 1.00 s, respectively.

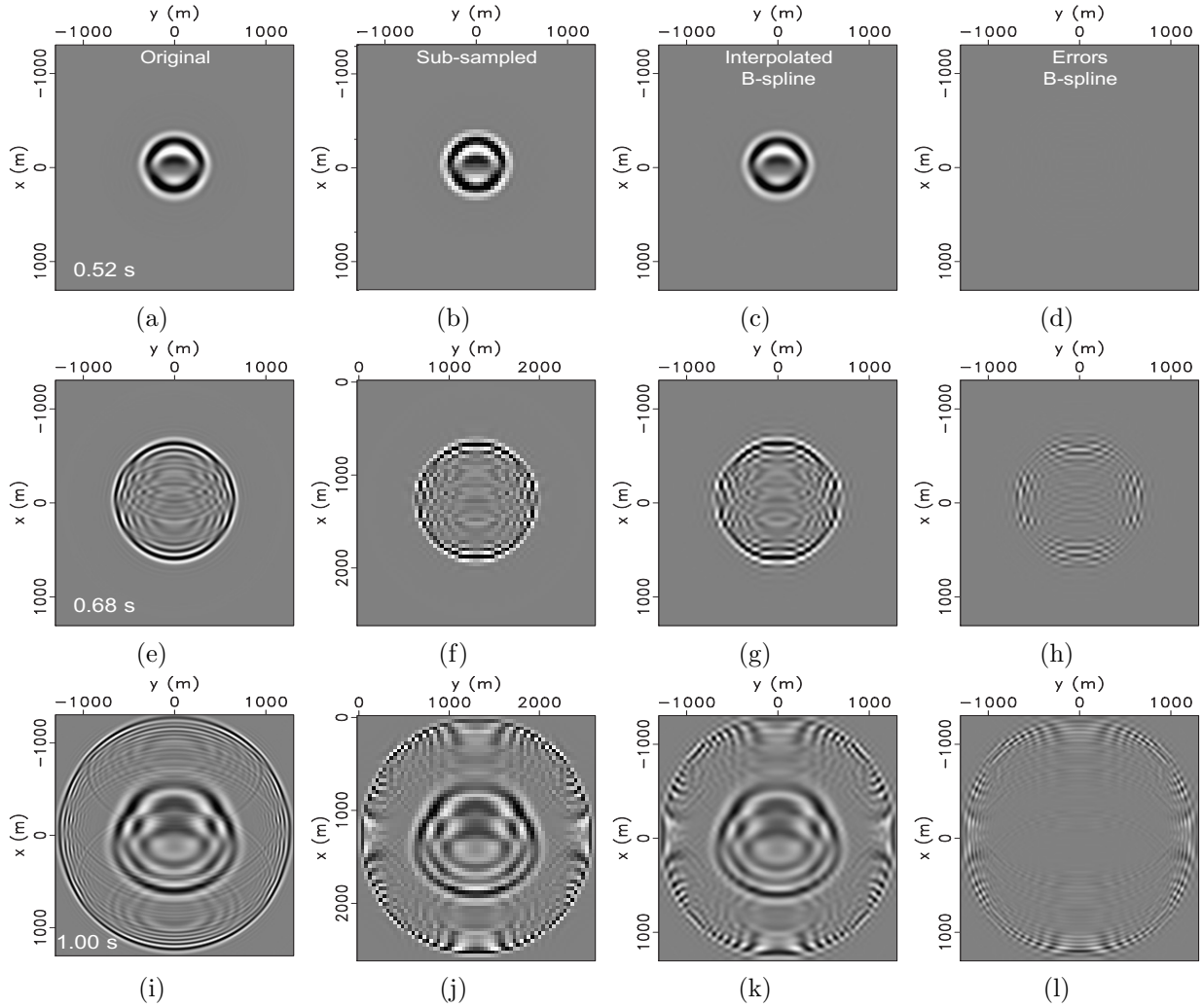

Figure 3.15: B-spline interpolation: Panels a, e, and i show the time slices of the directly simulated surface gather for 0.52 s, 0.68 s, and 1.00 s, respectively. Panels b, f, and j show the time slices of the sparse surface gather for 0.52 s, 0.68 s, and 1.00 s, respectively. Panels c, g, and k show the time slices of the interpolated surface gather by B-spline interpolation for 0.52 s, 0.68 s, and 1.00 s, respectively. Panels d, h, and l depict the differences between the interpolated surface gather and the direct simulated surface gather at 0.52 s, 0.68 s, and 1.00 s, respectively.

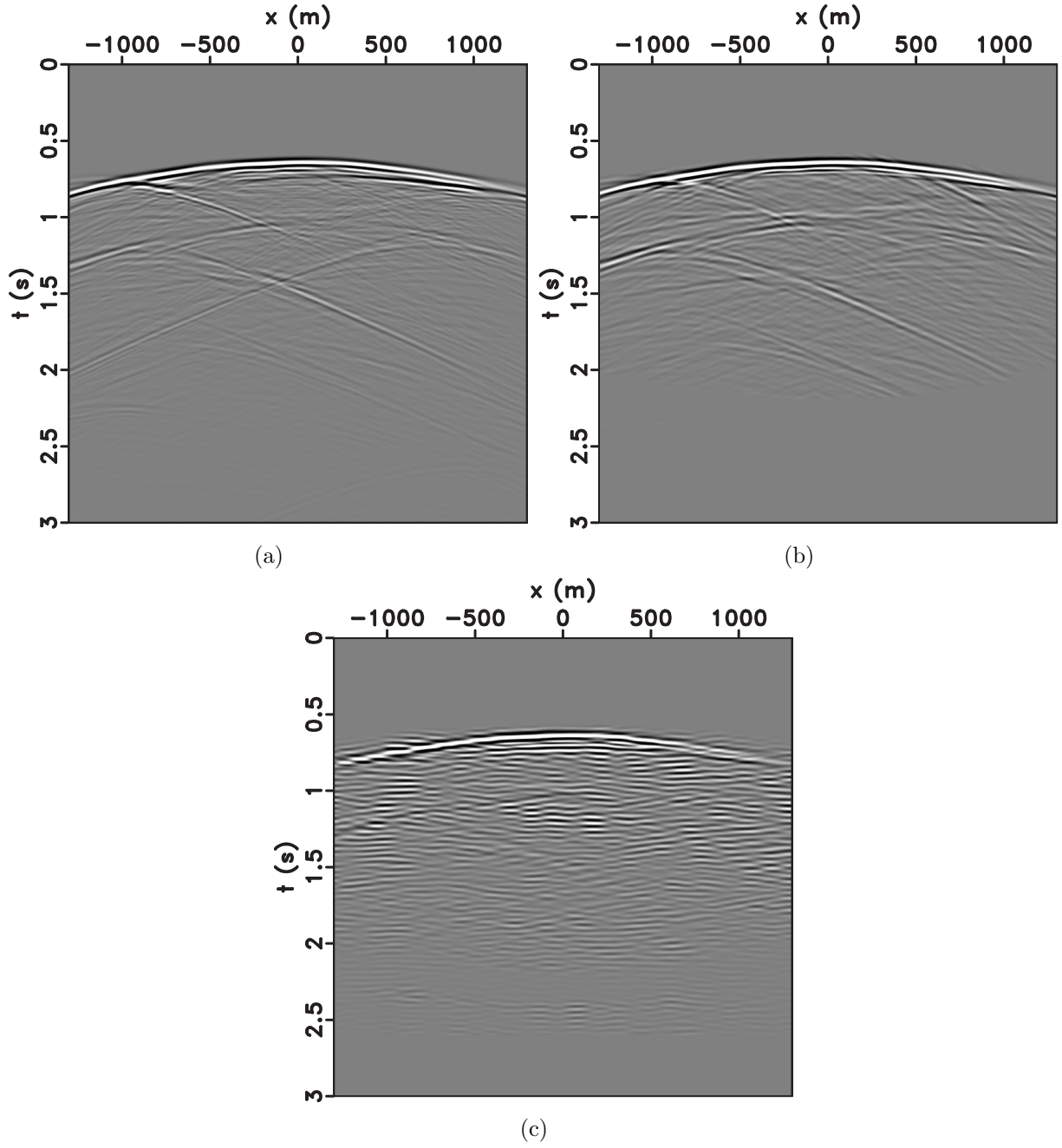

Figure 3.16: (a) In-line section of the 3D Green's function for a source at $x = 0\ m$, $y = 0\ m$, and $z = 1500\ m$ to receivers along $y = 0\ m$, simulated using 3D finite-difference modeling. (b) In-line section of the 3D Green's function retrieved by 3D Marchenko redatuming with densely sampled surface data. (c) In-line section of the 3D Green's function retrieved by 3D Marchenko redatuming with sparsely sampled surface data.

to the reference Green's function. We show the in-line section of the 3D Green's function retrieved by Marchenko redatuming with the 3D surface dataset interpolated by the 8-point B-spline in Figure 4.12a and the difference between Figure 4.12a and the reference Green's function Figure 4.11b in Figure 4.12b. Figure 4.12b shows negligible residuals, indicating that B-spline interpolation works well for 3D Marchenko redatuming. Sophisticated interpolation methods need to be investigated in the future for 3D data that are severely irregular and sparse, as in the case for example when ocean bottom nodes are used.

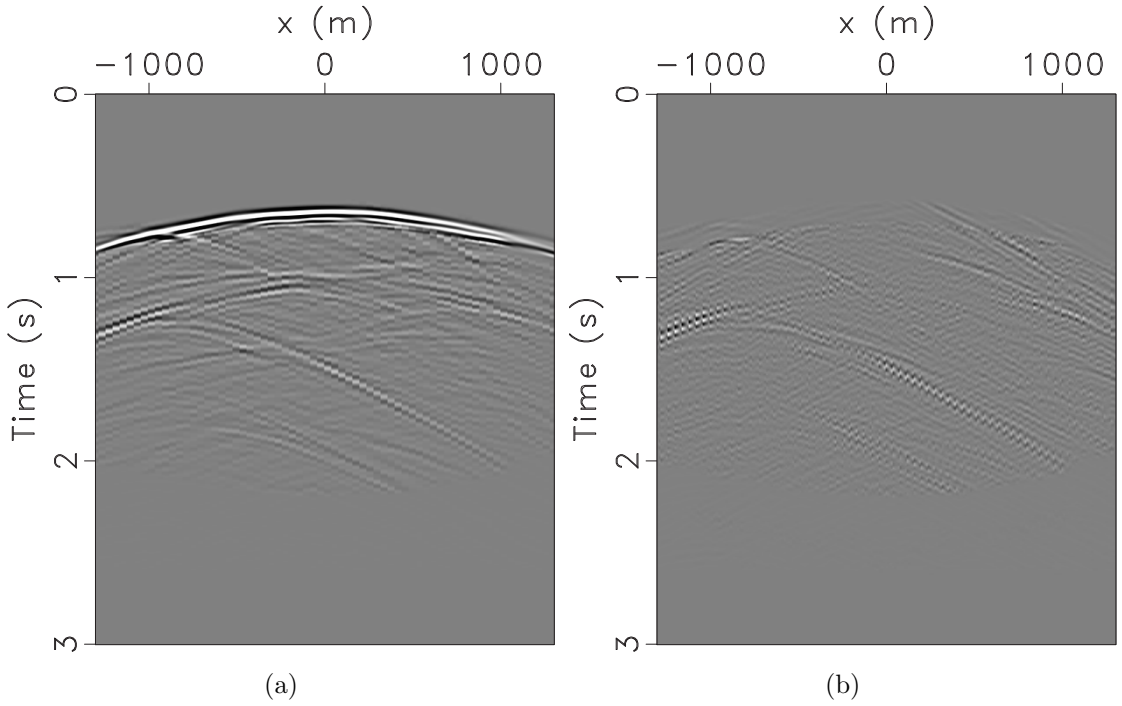

(a) (b)

Figure 3.17: (a) In-line section of the 3D Green's function retrieved by Marchenko redatuming with 3D interpolated surface data from nearest neighbor interpolation. (b) The difference between (a) and the reference Green's function.

3.5 Imaging with an erroneous background velocity: 2D and field data examples

In this section, we investigate the behaviour of Marchenko imaging given a background velocity model that contains errors. We perform three experiments with 1) a three-layer model, 2) a Gulf of Mexico model, and 3) a field data example involving imaging under a volcanic intrusion, and show that Marchenko imaging is robust with respect to velocity

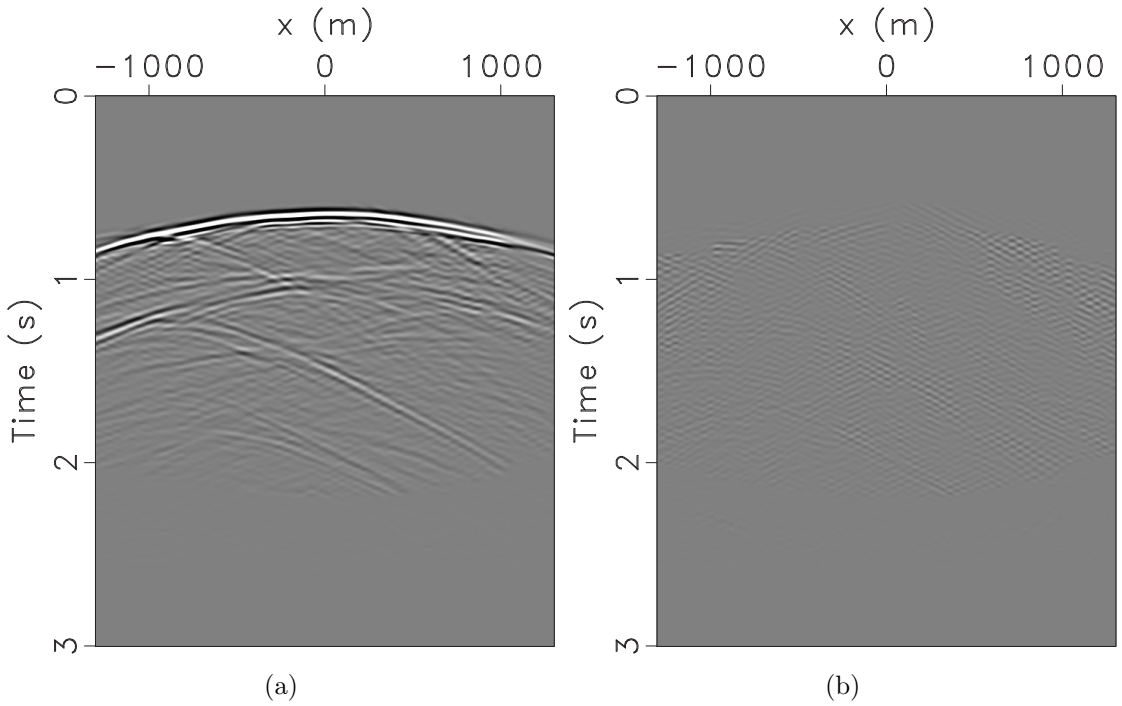

(a) (b)

Figure 3.18: (a) In-line section of the 3D Green's function retrieved by Marchenko redatuming with 3D interpolated surface data from 8-point B-spline interpolation. (b) The difference between (a) and the reference Green's function.

errors.

3.5.1 Three-layer model

In this numerical experiment, we use a simple velocity model - a three layer velocity model to investigate the influence of velocity errors for Marchenko imaging. We show the velocity model in Figure 3.19a and the RTM image produced with surface data in Figure 3.19b. There is no free surface boundary used for surface data generation so all the multiples in the surface data are internal multiples. The first two interfaces in the RTM image are the real interfaces for this model, however, the following three interfaces indicated in the image in Figure 3.19b by the green arrows are artifacts that are caused by internal multiples. Our goal is to remove these artificial events with the Marchenko method.

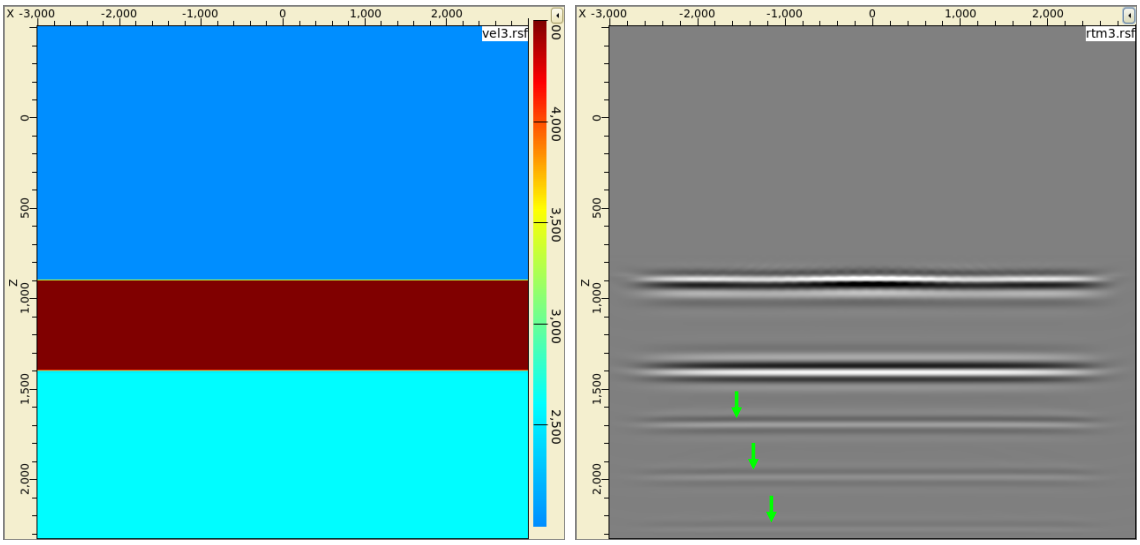

(a) (b)

Figure 3.19: (a) The velocity model of the three-layer model. (b) The RTM image produced with the surface data. The green arrows indicate the artifacts caused by internal multiples.

We show a comparison of the directly simulated Green's function for a subsurface location at $x = 0\ m$ and $z = 1200\ m$ to the surface and the retrieved Green's function with Marchenko redatuming using the true (or 100%) velocity in Figure 3.20a and Figure 3.20b, respectively. The first two events are the primary reflections by the two interfaces and the following events

are internal multiples. The retrieved Green's function (Figure 3.20b) matches well with the direct simulation (Figure 3.20a) in both kinematics and phase.

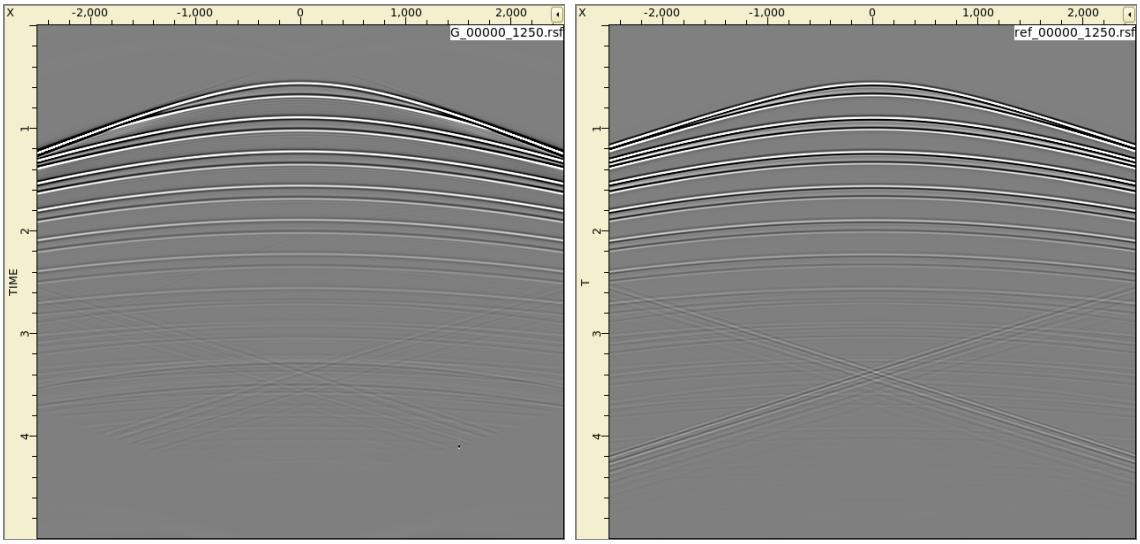

(a) (b)

Figure 3.20: (a) The Green's function for a subsurface location at $x = 0$ m and $z = 1200$ m to the surface simulated by finite-difference modeling. (b) The Green's function retrieved with Marchenko redatuming with the correct velocity.

We perform Marchenko imaging with the Green's functions retrieved with the surface data and three different velocity models: the true velocity model (100%), the velocity model that is 15% faster (115%) and the velocity model that is 50% faster (150%). We show the Marchenko images produced with these three background velocity models in Figure 3.21b, Figure 3.21c, and Figure 3.21d, respectively. The Marchenko image produced with the correct velocity (100%) shows good match with the model in Figure 3.21a for the locations of the interfaces. The interfaces in the Marchenko image produced with the velocity model of 15% errors and 50% errors are shifted and mapped to greater depth. There are, however, only two interfaces in these images and the artifacts caused by internal multiples are successfully eliminated despite of using inaccurate velocity models. This because that the image obtained by Marchenko imaging with an erroneous background model still focuses the multiples along with the primaries, although at the wrong location.

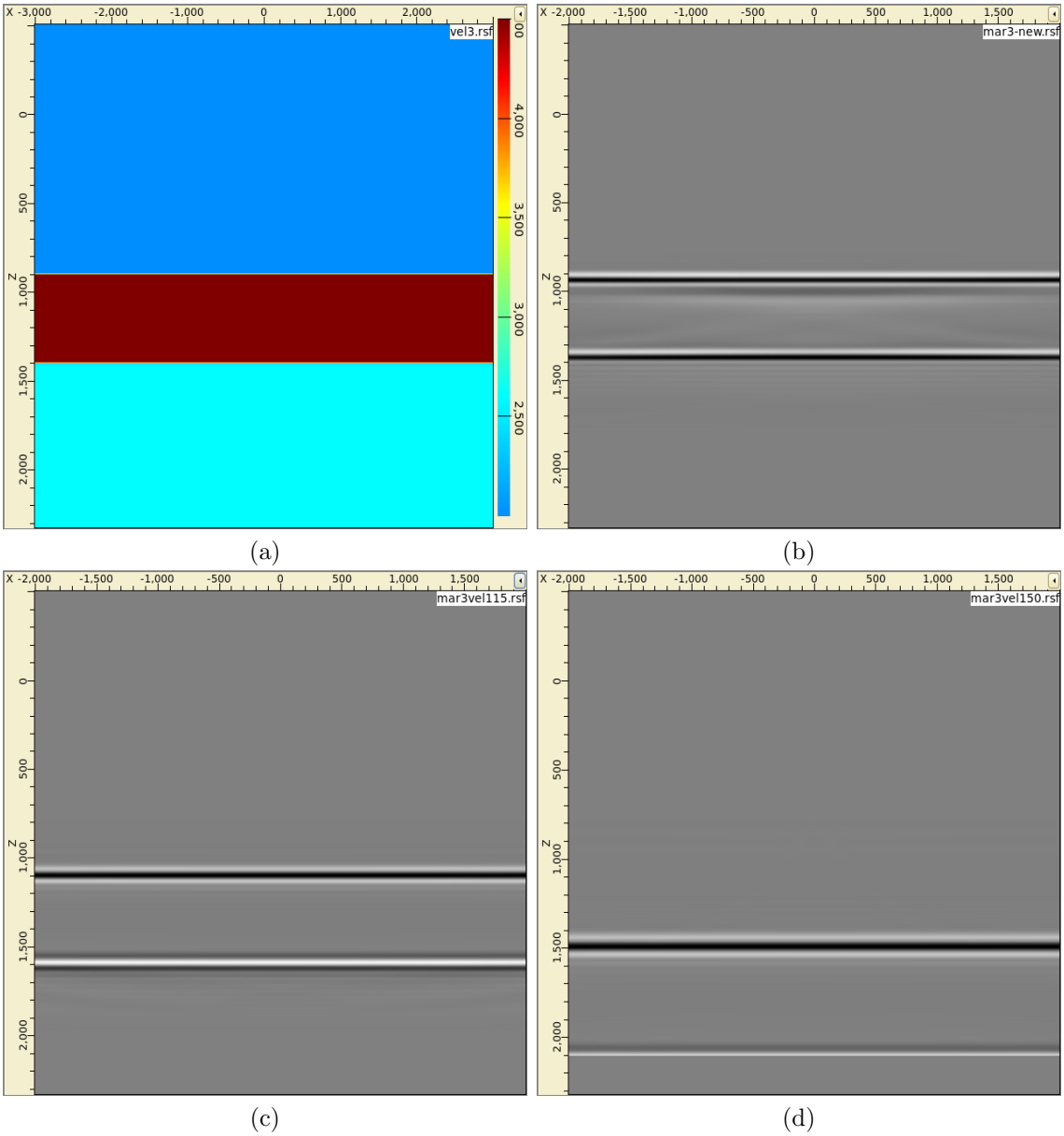

Figure 3.21: (a) The three-layer velocity model. (b) The Marchenko image produced with the correct velocity. (c) The Marchenko image produced with the model with the 15% velocity error. (d) The Marchenko image produced with the model with the 50% velocity error.

3.5.2 Gulf of Mexico model

In this synthetic experiment, we use a more complex model - the whole Gulf of Mexico model (the Gulf of Mexico model used in previous examples is a portion of this whole model) to test how Marchenko imaging behaves when the background velocity model is inaccurate. The green box in Figure 3.22 depicts the target area where we perform RTM and Marchenko imaging with the correct velocity model and the velocity model with that is 15% faster. We show an RTM image of the target area in Figure 3.23a. The dipping event between 3000 m and 4000 m is an artificial event that is caused by internal multiples from the bottom salt. This event is removed in the Marchenko image that is produced with the correct velocity model as shown in Figure 3.23b. We show the Marchenko image produces with the model with 15% velocity errors in Figure 3.23c. The locations of the four flat reflectors are shifted because the velocity model are off by 15%, but the dipping artifacts due to internal multiples is largely suppressed. A residual of the dipping artifacts shows up when using the 115% velocity, but it is much weaker compared to the one in the RTM image.

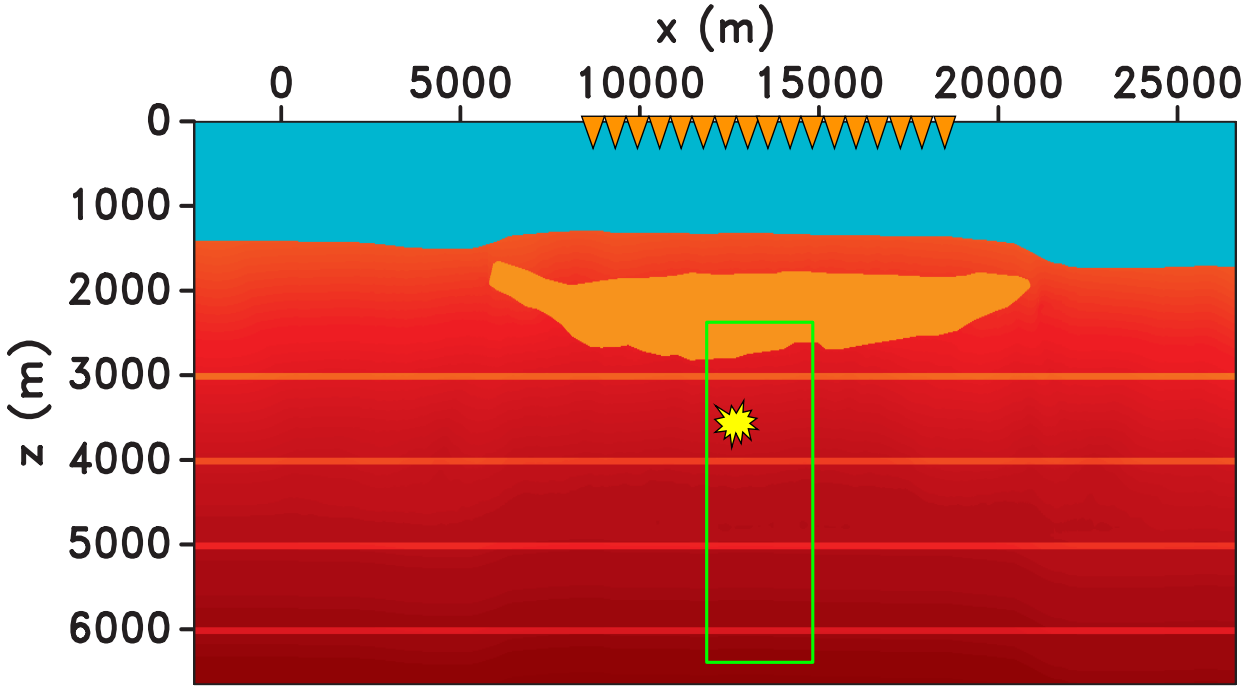

Figure 3.22: The Gulf of Mexico model. The green box indicates the target area.

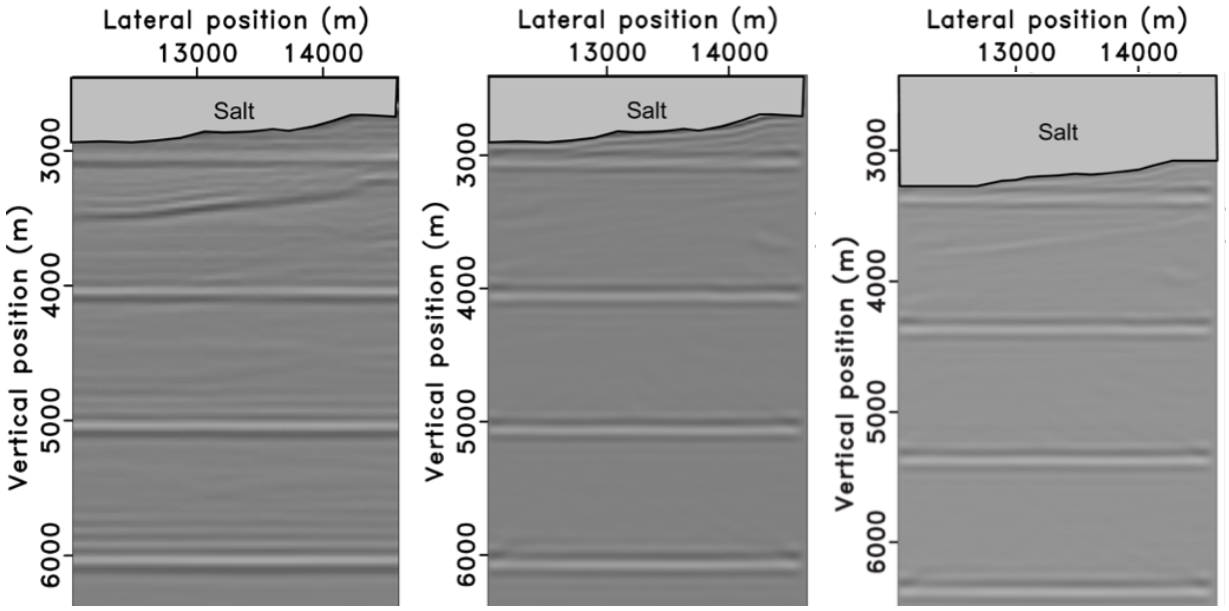

Figure 3.23: (a) The RTM image of the target area indicated by the green box for the Gulf of Mexico model shown in Figure 3.22. (b) The Marchenko image of the same area produced with 100% velocity. (c) The Marchenko image of the same area produced with 115% velocity.

3.5.3 Field data example

Last we show the influence of the background velocity model on the image produced by the Marchenko method with an offshore Brazil field data example, in which strong internal multiles are generated by volcanic intrusions. More information of the field dataset can be found in chapter 5, including the details of data regularization and the redatuming and imaging process. For the purpose of this study, we compare and analyze the final images produced by RTM and Marchenko imaging. The RTM image of the subsurface area of interest is shown in Figure 3.25a. The corresponding Marchenko image is shown in Figure 3.25b. Both images are generated with the same surface data and the same velocity model (Figure 3.24), a velocity model that is stongly smoothed and far from accurate. It's fair to assume that the velocity model is relatively accurate for the shallow parts and errors increase with depth. The red arrows in Figure 3.25a and Figure 3.25b depict the real subsurface structures. The green and blue arrows in Figure 3.25a depict the artifacts that are caused by internal multiples.

For this field data example, strong internal multiples are generated by the water bottom and volcanic intrusions. Note that the positions of the reflectors match well in the shallow areas (above the brown dashed line) in Figure 3.25a and Figure 3.25b, however, the deep reflectors right above the pink dashed line in the two images show up at slightly shifted locations. This is because for greater depth the imprint of velocity errors become larger. The velocity errors cause both RTM and Marchenko imaging to map the reflectors to shifted locations in the deeper portion of the model. Since Reverse Time Migration is based on two-way wave equation while Marchenko imaging is based on one-way travel time, the two methods behave slightly differently with respect to an erroneous velocity model of same errors. This example shows that, despite of using an inaccurate velocity model to estimate first arrivals, the Marchenko method is still able to eliminate the internal multiple artifacts.

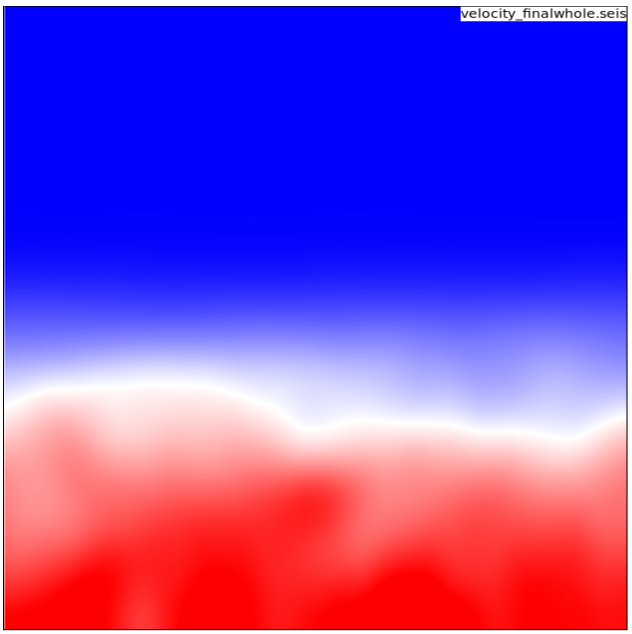

Figure 3.24: Background velocity model for the offshore Brazil dataset.

3.6 Discussion and conclusions

We investigate the two required inputs by Marchenko redatuming and imaging, the surface reflection data and the background velocity model. The surface data required by

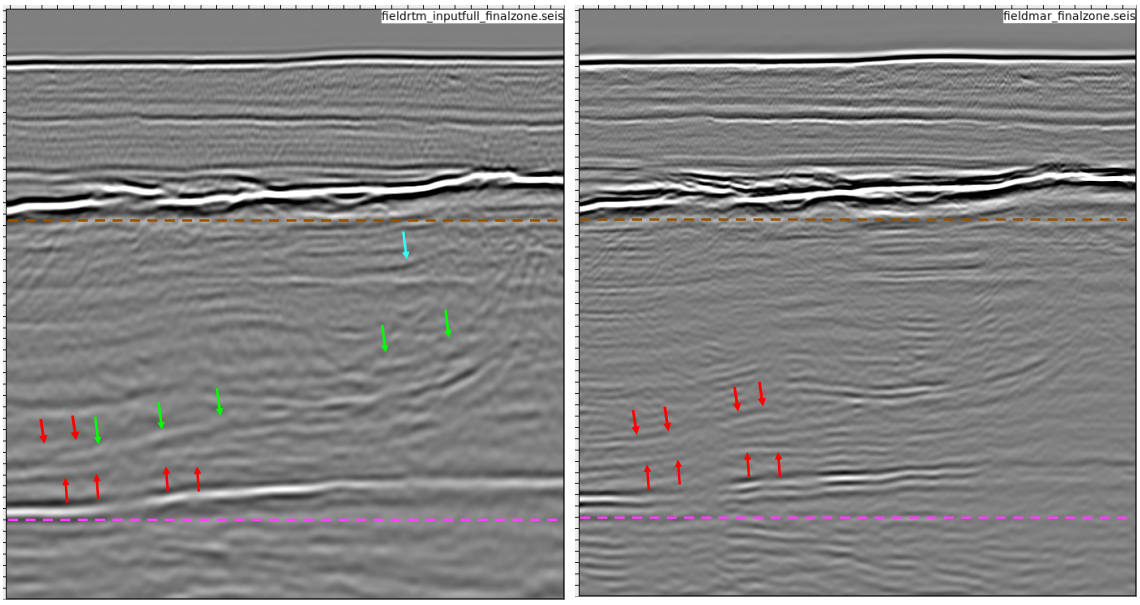

(a) (b)

Figure 3.25: (a) The RTM image of a target area produced with offshore Brazil field data. (b) The Marchenko image of the same area.

Marchenko redatuming needs to be acquired in an idealised scenario where, 1) an equal number of seismic sources and receivers are used for acquisition, 2) the depths and lateral positions of all sources and receivers are the same, 3) both sources and receivers are placed on an uniform, regular and dense grid, 4) the aperture of the sources and receivers are sufficiently large (Strategies for the determination of the acquisition sampling and aperture are discussed in Chapter 4 of this dissertation). Data regularization, which always involves data interpolation, is required to prepare the surface reflection data for Marchenko redatuming. We show that forward interpolation methods: nearest neighbor interpolation, Lagrange interpolation, *Sinc* interpolation, and B-spline interpolation are sufficiently accurate for 2D data regularization. The imprint of the sampling and interpolation errors are smaller in the extracted Green's function than in the interpolated shot gathers, as the Marchenko redatuming algorithm involves an integration over surface locations and edge tapers are applied for far offsets at each iteration. For 3D data regularization, with a relatively complex 2.5D Gulf of Mexico model, we show that B-spline interpolation is sufficiently accurate to interpolate

sparse 3D shot gather, while nearest neighbor interpolation produces significant errors. We focus on the interpolation for missing receivers in this study. One way to reconstruct missing sources is to utilize the interpolated receiver traces and source-receiver reciprocity. In general, interpolation for sources in three dimensions is a challenging problem and needs further investigations. We then show that the background velocity model required by Marchenko redatuming does not need to be known in great detail. We demonstrate that, with an erroneous background model, Marchenko redatuming still focuses the multiples along with the primaries (although both at the wrong location), and in the following imaging stage, the retrieved internal multiples can still be effectively eliminated by multi-dimensional deconvolution. In sum, combination of Marchenko redatuming and imaging is robust when an erroneous velocity model is used to estimate the first arrivals.

3.7 Acknowledgements

This work was supported by the Consortium Project on Seismic Inverse Methods for Complex Structures at the Colorado School of Mines.

CHAPTER 4

3D MARCHENKO GREEN'S FUNCTION RETRIEVAL

Xueyi (Alex) Jia[1], Yang Zhao[2], and Roel K. Snieder[1]

In SEG Technical Program Expanded Abstracts 2018, pp. 4588-4592. Society of Exploration Geophysicists, 2018. Prepared for submission to *Geophysics*.

4.1 Abstract

The response to an impulse source is defined as Green's function. The Green's function of the earth represents the elastic properties of the earth's interior. Marchenko redatuming enables an accurate retrieval of the earth's Green's function using single-sided seismic reflection responses in a one, two or three dimensional medium. Various studies have been published to demonstrate instinct aspects or applications of the Marchenko method. The majority of the Marchenko examples, however, are performed with a 1D or 2D wave propagation. We investigate Marchenko redatuming in the three dimensions. We reformulate the Marchenko-type equations in the three dimensional Cartesian coordinate system, which is then realised in our 3D numerical implementation of Marchenko redatuming. Based on the 3D Marchenko equations and the stationary phase method, we propose an approach to determine the aperture and the spatial sampling of the source/receiver pairs required by 3D Marchenko redatuming. To overcome the sparsity of the 3D seismic data acquired with practical 3D marine towed-streamer surveys, we revisit a forward interpolation method, based on B-splines, for 3D data regularization. We validate our 3D Marchenko redatuming algorithm with a 3D trapezoidal-dipping model and a 2.5D Gulf of Mexico salt model. By comparing the retrieved 3D Green's function with a simulated one by finite-difference modeling, we demonstrate that both primaries and multiples are accurately reconstructed with

[1]Center for Wave Phenomena, Colorado School of Mines, 1500 Illinois St., Golden, CO 80401, USA
[2]Former: Aramco Services Company: Aramco Research Center-Houston, Texas, USA. Current: China University of Petroleum, Beijing, China.

our 3D Marchenko redatuming algorithm given a dataset acquired from an idealised acquisition geometry. We then apply B-spline interpolation to sparse 3D data and demonstrate that the Green's function retrieved with the interpolated 3D data is sufficiently accurate. We discuss the associated computational optimization of the 3D numerical implementation of Marchenko redatuming for the purpose of saving memory and CPU time. We clarify the similarities and differences between surface-related multiple elimination (SRME) and the Marchenko method.

4.2 Introduction

Rose (2001) raised a simple yet interesting question: can one find a wave, incident from one side of a medium, such that the wave focuses at a pre-defined location and time? He sought for the equation that determines such a focusing incident wave, and he found that the equation he looked for was the Marchenko's equation. Marchenko (1955) derived the equation of 1D inverse-scattering, which governs single-sided focusing for several wave equations (such as the time-dependent Schrödinger equation and the plasma wave equation). Hence, a newly developed framework, which aims to retrieve the impulse response to a virtual source at a pre-defined location inside a medium, was named after Marchenko. This framework to retrieve the scattering effects of a medium was first formulated by Broggini *et al.* (2012) and by Broggini & Snieder (2012) for seismic applications, where they demonstrated the Marchenko framework using the single-sided reflection response of a 1D medium. Based on a decomposition of the wavefield into upgoing and downgoing waves, Wapenaar *et al.* (2014b) generalized the theory of Marchenko redatuming/Green's function retrieval to 2D and 3D, and they proposed the framework to eventually produce a seismic image based on the up and down decomposition of the retrieved Green's functions. The retrieved Green's function is proven to accurately contain both primaries and multiples that propagates in the medium. Therefore, unlike conventional imaging approaches which are meaningful only for the primaries, Marchenko imaging provides an alternative idea for creating a seismic image which takes the internal multiples into account (Behura *et al.*, 2014; Broggini *et al.*,

2014b; Singh *et al.*, 2015a; Wapenaar *et al.*, 2014b). More specifically, the artifacts caused by internal multiples can be eliminated in the seismic image produced by Marchenko imaging.

The Marchenko framework continued to develop towards several directions. da Costa Filho *et al.* (2014, 2015) investigated the elastic extensions of both Marchenko redatuming and imaging. After Ravasi *et al.* (2016) presented a first field example for Marchenko imaging, Jia *et al.* (2017) investigated the practical aspects of applying subsalt Marchenko imaging using a Gulf of Mexico field dataset. Staring *et al.* (2017) applied an adaptive Marchenko imaging scheme to a marine streamer dataset. Singh *et al.* (2015b, 2016b) added to the Marchenko framework by integrating the free-surface multiples in the seismic reflection response into the Marchenko equations with the aim to bypass the need for applying SRME to the seismic recordings. Dukalski & de Vos (2017) proposed two methods to solve the Marchenko equation: LSQR (least squares) method and a modified Levinson-type algorithm, both of which take account of the internal multiples and the free-surface multiples without suffering from convergence problems. Provided dual-sensor (e.g. pressure and vertical particle velocity) data, Ravasi (2017) and Slob & Wapenaar (2017) proposed approaches to solve the couple Marchenko equations that can handle band-limited seismic date with an unknown wavelet from a more flexible acquisition system (arbitrarily located sources above a line of regularly sampled receivers). Besides imaging, applications such as internal multiples prediction and removal, source wavelet estimation, and time-lapse monitoring have been developed based on the Marchenko framework (Meles *et al.*, 2014; Mildner *et al.*, 2017; Wapenaar & Slob, 2017).

For the Marchenko applications discussed above, the numerical experiments are mostly carried out with 2D seismic surveys, which provide a "slice" or cross-section through the earth. It is assumed that seismic reflections arise along the vertical plane of the acquisition line in 2D seismic experiments. When the earth has significant cross-line structures, the seismic reflections recorded on the 2D survey line might come from the out-of-plane reflections. The events caused by the out-of-plane structures exist in the 2D seismic recording but

cannot be explained with 2D models. In this case, the idea of 2D seismic doesn't work very well. Also, the cross-line spacing between 2D survey lines can be large (as large as 1 km); therefore, attempts to interpret adjacent 2D sections involve a high degree of guesswork and inaccuracy, and often result in an incorrect interpretation. Today, 3D seismic surveys, in which a designed grid layout of receivers and sources covering an area on the surface are used for acquisitions, has become a standard tool for oil and gas exploration and production. Seismic methods for three-dimension configurations are significant for fields with complex structures. In the theory subsection, we reformulate the Marchenko type equations in three-dimension Cartesian coordinates that can be directly implemented numerically. Based on the spatial variation of the integrand in the Marchenko equations, we propose an approach to efficiently determine the smallest aperture for the surface seismic survey and the largest spatial sampling of the sources/receivers pairs required by the Marchenko algorithm. We discuss the B-spline interpolation method that we use for the cross-line data reconstruction for the marine streamer type data. In the numerical experiments subsection, we apply 3D Marchenko redatuming with a 2.5D Gulf of Mexico salt model and a 3D trapezoidal and dipping model. We demonstrate that 3D Marchenko redatuming is able to retrieve both primaries and multiples with an ideal dataset. Then we create a synthetic marine streamer dataset with sparse cross-line data sampling and conduct the B-spline interpolation to reconstruct the data in-between the cross lines. We apply our 3D Marchenko algorithm to the dataset reconstructed by the B-spline method, and demonstrate that we are able to successfully retrieve the Green's function with the reconstructed dataset. Finally, we discuss how to save memory and CPU time in our implementation of the 3D Marchenko redatuming algorithm.

4.3 Theory

We reformulate the equations for the Marchenko algorithm from Wapenaar *et al.* (2014b) in a three dimensional Cartesian coordinate system as following,

$$M_k^+\big(\mathbf{r_0''},\mathbf{r}',-t\big)=\int_{\partial x_0}\int_{\partial y_0}\Bigg(\int_{-t^d}^{t}R\big(\mathbf{r_0''},(x_0,y_0,0),t-t'\big)\cdot f_{1,k}^-\big((x_0,y_0,0),\mathbf{r}',-t'\big)dt'\Bigg)dy_0dx_0; \quad (4.1)$$

and

$$f_{1,k+1}^-\big(\mathbf{r_0''},\mathbf{r}',t\big)=f_{1,0}^-\big(\mathbf{r_0''},\mathbf{r}',t\big)+\int_{\partial x_0}\int_{\partial y_0}\Bigg(\int_{-t^d}^{t}R\big(\mathbf{r_0''},(x_0,y_0,0),t-t'\big)\cdot M_k^+\big((x_0,y_0,0),\mathbf{r}',t'\big)dt'\Bigg)dy_0dx_0; \quad (4.2)$$

with

$$f_{1,0}^-\big(\mathbf{r_0''},\mathbf{r}',t\big)=\int_{\partial x_0}\int_{\partial y_0}\Bigg(\int_{-\infty}^{-t^d}R\big(\mathbf{r_0''},(x_0,y_0,0),t-t'\big)\cdot T_d\big(\mathbf{r}',(x_0,y_0,0),t'\big)dt'\Bigg)dy_0dx_0, \quad (4.3)$$

where $\mathbf{r_0''}=(x_0'',y_0'',0)$ represents a point located on the surface, and $\mathbf{r}'=(x_i',y_i',z_i')$ stands for a point located in the 3D earth model at the depth of z_i' (as shown in Figure 4.1). Symbol R represents the seismic reflection response. Particularly, $R\big(\mathbf{r_0''},(x_0,y_0,0),t-t'\big)$ represents the reflection response corresponding to a source at the surface location $\mathbf{r_0''}$ and a receiver at the surface location $(x_0,y_0,0)$, at time $t-t'$. The one-way travel time of the first arrival from a subsurface focusing location at (x_i',y_i',z_i') to a surface location $(x_0,y_0,0)$ is represented by t^d. Using S to represent the source wavelet and D to represent the recorded surface data, the surface reflection response is given by $R=S^{-1}*D$, where symbol $*$ represents temporal convolution. The detailed physical meanings of M_k^+, $f_{1,k}^-$, and T_d are discussed in Wapenaar *et al.* (2014b).

The integrations over dy_0 and dx_0 should be ideally applied over an infinite surface. Covering an infinite line (in 2D) or infinite surface (in 3D) is impossible in practice. According to

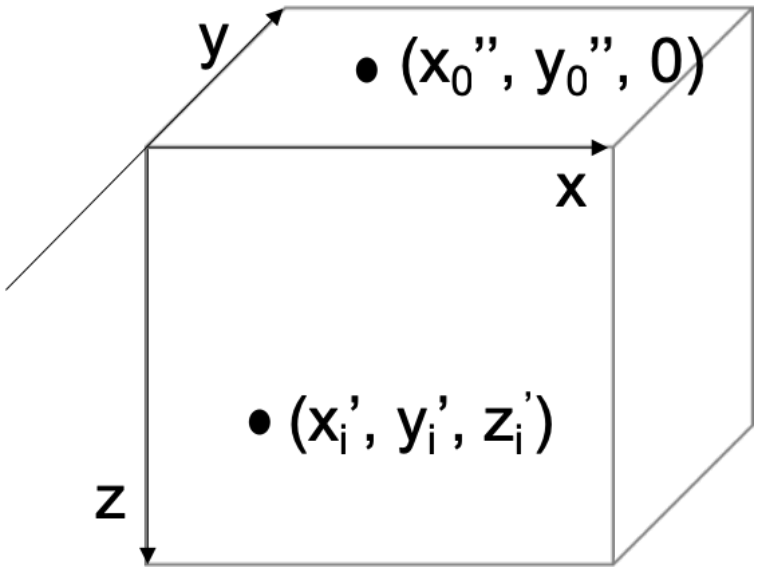

(a)

Figure 4.1: Illustration of symbols of the 3D points. Subscript 0 indicts the point is at the earth surface and subscript i indicts the point is in the subsurface.

the method of stationary phase that is mentioned in the appendix of Wapenaar *et al.* (2012), once the stationary phase zone is properly sampled and covered, an accurate estimation of the integration can be obtained. In the following subsection, we introduce an approach to determine the stationary phase area and the spatial sampling by investigating the integrand in equation 4.3. Equations 4.1, 4.2, and 4.3 are directly implemented for numerical computations of the 3D Green's function.

4.3.1 Spatial sampling and aperture of the source/receiver pairs

Marchenko redatuming requires the seismic data to be recorded with co-located sources and receivers which are placed regularly and densely along a straight line on the surface for 2D cases or on a grid layout covering a surface area for 3D cases. This requirement for data originates from equations 4.1, 4.2, and 4.3, where an infinite line or area integral needs to be evaluated. An infinitely large acquisition aperture is, of course, not practical. To determine the largest spatial sampling and the smallest aperture required by Marchenko redatuming for

the retrieval of the Green's function at a certain depth/location, we investigate the integrand of equation 4.3, which is a temporal convolution between the direct arrival from virtual source to the surface and a common shot gather at the surface.

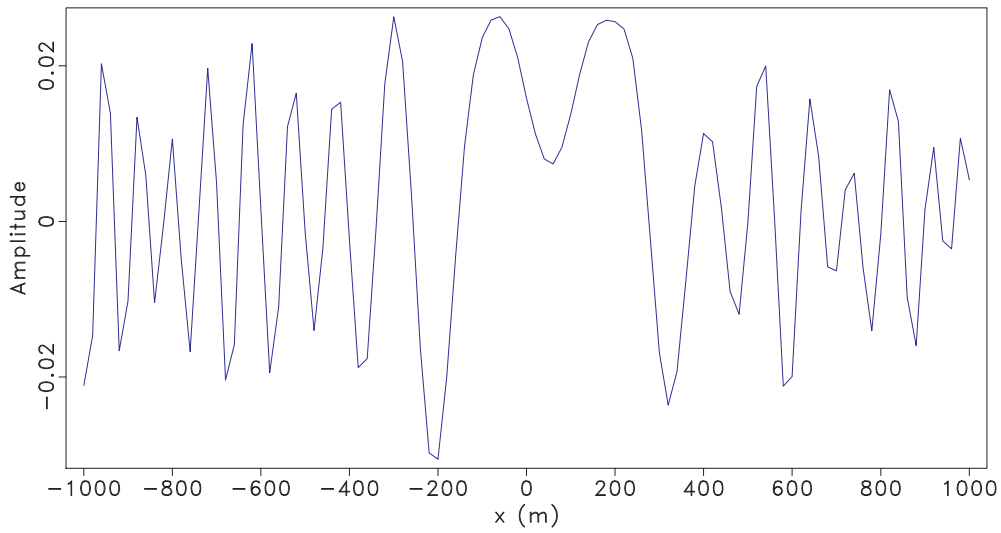

(a)

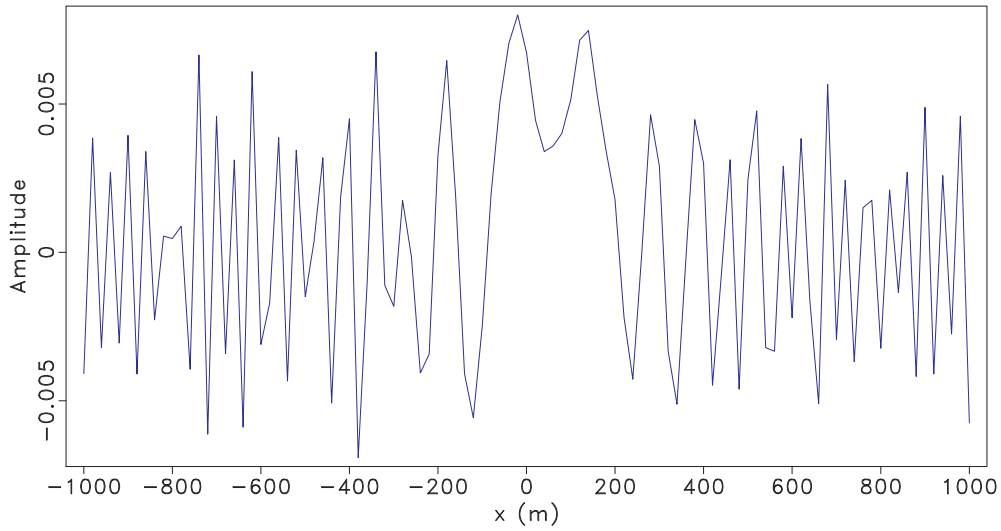

(b)

Figure 4.2: (a) Cross-section of the integrand in equation 4.3 at 20 Hz in the frequency domain, (b) Cross-section of the integrand of equation 4.3 at 40 Hz in the frequency domain.

We select a 2D cross-section at $x = 0\ m$ in the velocity model (Figure 4.4a) and the density model (Figure 4.4b) for demonstration. Figure 4.2a and Figure 4.2b show the integrand of equation 4.3 in the frequency domain for a focusing point located at $\mathbf{r}'$ ($x = 200\ m$, $y = 0$

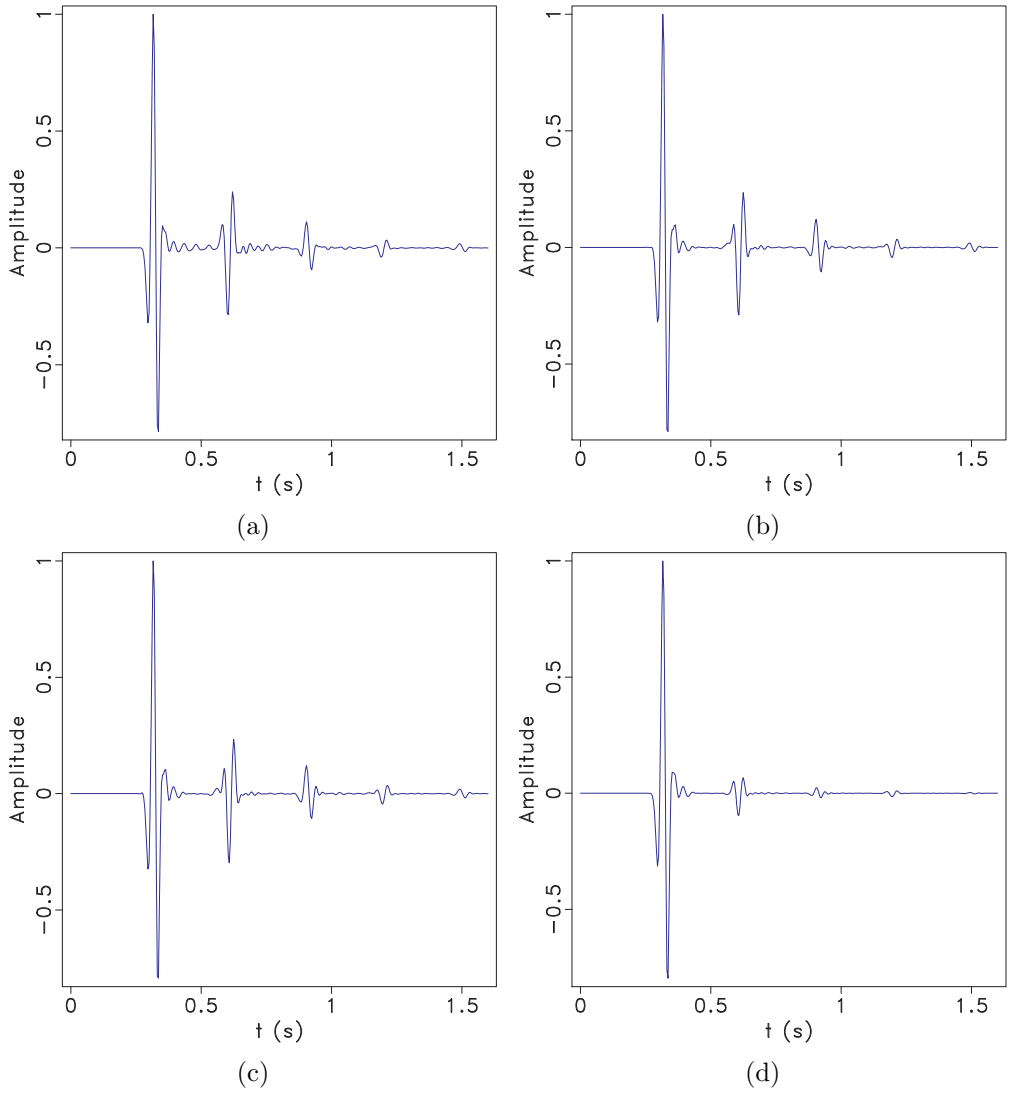

Figure 4.3: (a) Green's function from a virtual source $\mathbf{x}'$ ($x = 0\ m$ and $z = 800\ m$) to a surface receiver $\mathbf{x_0''}$ ($x = 0\ m$ and $z = 0\ m$) produced using finite-difference modeling, (b) Green's function retrieved with Marchenko redatuming with spacial sampling of $dx = 10\ m$ and an aperture from $-1000\ m$ to $1000\ m$, (c) Green's function retrieved with Marchenko redatuming with spacial sampling of $dx = 25\ m$ and an aperture from $-1000\ m$ to $1000\ m$, (d) Green's function retrieved with Marchenko redatuming with spacial sampling of $dx = 10\ m$ and an aperture from $-200\ m$ to $200\ m$.

m, and $z = 800\ m$). The surface shot is located at $\mathbf{r_0''}$ ($x = 200\ m$, $y = 0\ m$, and $z = 0\ m$). Figure 4.2a is a cross-section at 20 Hz and Figure 4.2b is a cross-section at 40 Hz, which is close to the high end of the frequency band of the data. We can identify the stationary phase zones in the middle and rapid oscillations outside of the stationary phase zone. Summing/integrating along the horizontal axis (receiver locations), the high frequency oscillations on the side lobes will cancel out and converge approximately to zero.

To avoid aliasing and improve accuracy, we choose to put at least four sampling points within the smallest wavelength of the curves in Figure 4.2b. The smallest wavelength for the maximum frequency (Figure 4.2b) is approximately 100 m; therefore, the largest space between two neighboring sources/receivers should be no larger than 25 m ($dx \leq 25\ m$). We also need to properly sample and cover the stationary phase area to obtain a good approximation of the integral. Figure 4.2a and Figure 4.2b indicate how to determine the aperture for a virtual source at a specific depth. In this example, placing source/receiver pairs ranging from $-500\ m$ to $500\ m$ is sufficient to cover the stationary phase area.

We perform three experiments using various values of spatial sampling and aperture for verification. Figure 4.3a shows the Green's function obtained using finite-difference modeling, which is used as a reference. Figure 4.3b shows the retrieved Green's function with an aperture of 1000 m and spatial sampling of 10 m. Figure 4.3c shows the retrieved Green's function with an aperture of 1000 m and sampling of 20 m. Both sampling intervals fall into our desired sampling range (smaller than 25 m), and we obtain almost the same results of the retrieved Green's function both in amplitudes and kinematics (Figure 4.3b and Figure 4.3c). Figure 4.3d shows the retrieved Green's function with an aperture ranging from $-200\ m$ to $200\ m$ with a source/receiver spacing of 10 m. Since the sources/receivers in this experiment do not cover the entire stationary phase zone, the value of the integration computed with this source/receiver coverage is less than the theoretical value of the integration. Thus, the amplitudes of the retrieved Green's function is underestimated.

The criteria that we use to determine the aperture and spatial sampling is summarized as follows: 1) the aperture should be large enough to cover the stationary phase area of the integrand of equation 4.3 in the frequency domain, and 2) the smallest wavelength of the integrand of equation 4.3 in the frequency domain should be sampled at least by four points.

The aperture and spatial sampling are determined according to the targeting redatuming depth and the surface shot data with this approach. In general, deeper virtual sources require larger acquisition aperture yet allow for a sparser spatial sampling. The reason is that for deeper virtual sources, the horizontal wavelengths observed at the earth surface are longer, and having four samples in one horizontal wavelength leads to a more relaxed spatial sampling requirement at the surface. Given a background velocity model, this approach can be used at an early stage for survey designs to determine the sampling and aperture for various Marchenko applications and can be used to decide if a provided dataset with a particular aperture and spatial sampling meets the requirements for Marchenko redatuming and imaging.

4.3.2 Interpolation for 3D data

Indicated by the integrations in 3D Marchenko equations 4.1, 4.2, and 4.3 (with infinite limits of integration along x and y axis), the Marchenko algorithm requires a dataset with a sufficiently large range along the x and y axis and a sufficiently small spatial sampling. Here we define x axis as the in-line direction and y axis as the cross-line direction for a 3D marine streamer seismic survey. In typical 3D marine seismic acquisitions, spatial sampling (dx) along the in-line direction is relatively small, however, spatial sampling (dy) along the cross-line direction is much larger/sparser (usually fourfold of dx). In order to make the marine streamer type of data meet the requirements of 3D Marchenko imaging (in other words, to accurately evaluate the integrations in equations 4.1, 4.2, and 4.3) with a 3D streamer dataset), we need to conduct interpolation along the cross-line direction.

We assume that cross-line are regularly sampled in a 3D marine steamer survey. Here we introduce the B-spline method, which is proven to be accurate and efficient for interpolating

regularly spaced data (Fomel, 2000). The B-spline is a set of convolutional basis for forward interpolation problems and related signal processing problems due to their compact support and other attractive numerical properties (Unser, 1999). Fomel (2000) showed that the B-spline method leads to a faster iterative conversion in under-determined problems and a more accurate result in over-determined problem in comparison with other linear interpolation methods, such as the nearest neighbor method and Sinc interpolant method.

Here we briefly summaries the forward interpolation method with B-spline basis. The general form of a linear forward interpolation operator is

$$f(x) = \sum_{n \in N} W(x, n) f_n, \tag{4.4}$$

where n is a point on a given regular grid N, x is a point in the continuum, $f(x)$ is the reconstructed continuous function, and $W(x, n)$ is a linear weight. This form can be generalized to multi-dimensions.

One general approach to construct the weighting function in equation 4.4 is to select an appropriate basis to represent the function $f(x)$. The function basis takes the form

$$f(x) = \sum_{k \in K} c_k \psi_k(x), \tag{4.5}$$

where $\psi_k(x)$ are basis function, and c_k are the corresponding coefficients. The $W(x, n)$ function can be defined with the least squares method, once an appropriate basis is selected.

In the B-spines method, we select a convolutional basis in such way that B-spline $\beta^n(x)$ of an order n can be defined by a repetitive spatial convolution of the zeroth-order spline $\beta^n(x)$ (the boxcar function) with itself:

$$\beta^n(x) = \beta^0(x) * ... * \beta^0(x). \tag{4.6}$$

Hence, the B-spline basis satisfies equation

$$\psi_k(x) = \beta(x - k). \tag{4.7}$$

Substituting equation 4.7 into equation 4.5 yields

$$f(x) = \sum_{k \in K} c_k \beta(x - k). \tag{4.8}$$

Evaluating the function $f(x)$ in equation 4.8 at an integer value n yields,

$$f_n = \sum_{k \in K} c_k \beta(n - k), \tag{4.9}$$

which leads to the exact form of a discrete convolution. We can invert equation 4.9 to obtain the coefficients c_k from $f(n)$ by means of deconvolution. With the B-spline convolutional basis, forward interpolation becomes a two-step procedure: (1) obtain the basis coefficients c_k by deconvolving the sampled function $f(n)$ with the factorized filter $\beta(n)$ based on equation 4.9, and (2) reconstructs function $f(x)$ according to equation 4.8.

The explicit expression of the B-spline basis is (Fomel, 2000)

$$\beta^n(x) = \frac{1}{n!} \sum_{k=0}^{n+1} C_k^{n+1} (-1)^k (x + \frac{n+1}{2} - k)_+^n, \tag{4.10}$$

where C_k^{n+1} are the binomial coefficients which are given by

$$C_k^n = \frac{n!}{k!(n-k)!}, \tag{4.11}$$

and the function x_+ is defined as: for $x > 0$, $x_+ = x$, otherwise $x_+ = 0$.

We apply the B-spline interpolation at each time sample, which is most accurate when the curvatures of seismic events in the dataset are relatively flat in time domain. To fulfill this condition, we first apply normal moveout (NMO) to the dataset before interpolation to flatten the seismic arrivals. We aim to make the curvature of the seismic events relatively small and flat without requiring a perfect NMO velocity model. Then we conduct the B-spline cross-line interpolation in the NMO domain. Finally we apply the inverse NMO to obtain the reconstructed dataset with the densely interpolated cross-line data.

4.4 Numerical examples

4.4.1 Trapezoidal and dipping 3D model

In this synthetic example, we use a set of trapezoidal and dipping 3D velocity and density models (Figure 4.4a and Figure 4.4)b to validate our 3D Marchenko Green's function retrieval algorithm. On an arbitrary $x - z$ section, the model contains a trapezoidal high velocity/density layer in the middle. On an arbitrary $y - z$ section, the model contains three dipping layers. The grid of source/receiver pairs we use for Marchenko redatuming is chosen as 101 grid lines (cross-line, $-2000\ m$ to $2000\ m$) by 101 grid lines (in-line, $-2000\ m$ to $2000\ m$), and the spacing between neighboring sources/receivers is $20\ m$ in both cross-line and in-line directions.

As indicted by equations 4.1, 4.2, and 4.3, the integrals are evaluated over x axis and y axis successively as two one-dimensional integrals. Figure 4.5a shows the reference Green's function obtained using 3D finite-difference modeling from a virtual source at ($x = 0\ m$, $y = 0\ m$, and $z = 600\ m$) to a line of receivers (along $y = 0\ m$) at the earth's surface ($z = 0\ m$). Figure 4.5b shows the corresponding Green's function produced using our 3D Marchenko redatuming algorithm. The reference Green's function obtained using 3D finite-difference modeling from a virtual source at ($x = 0\ m$, $y = 0\ m$, and $z = 600\ m$) to a line of receivers (along $x = 0\ m$) at the earth's surface ($z = 0\ m$) and the corresponding Green's function produced using our 3D Marchenko redatuming algorithm are shown in Figure 4.6a and Figure 4.6b respectively. A comparison of the asymmetry of the Green's functions in both Figure 4.6a and Figure 4.6b indicates that both primaries and multiples are correctly retrieved with the dip interfaces taken into account.

4.4.2 3D Marchenko with sparsely sampled data

We test our 3D Marchenko algorithm with a 2.5D Gulf of Mexico model in this numerical experiment. Figure 4.7a and Figure 4.7b show the velocity and the density of the 2.5D Gulf of Mexico model. This model is referred to as a 2.5D model as it is created by extending a

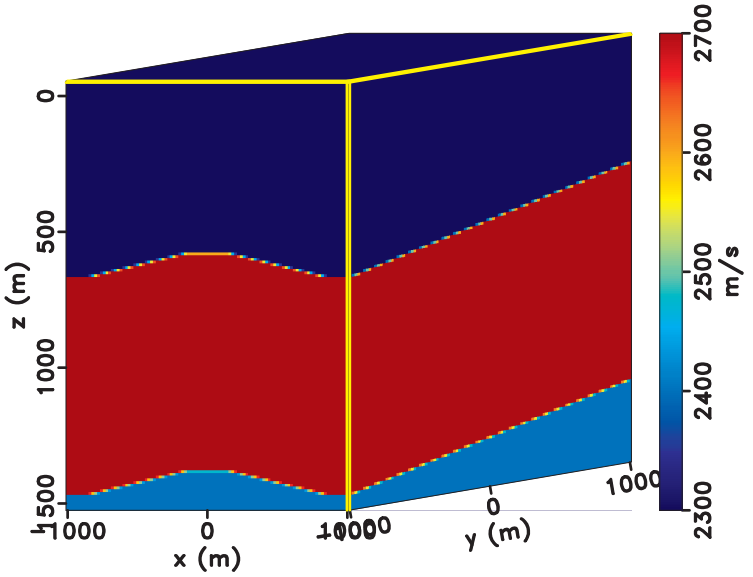

(a)

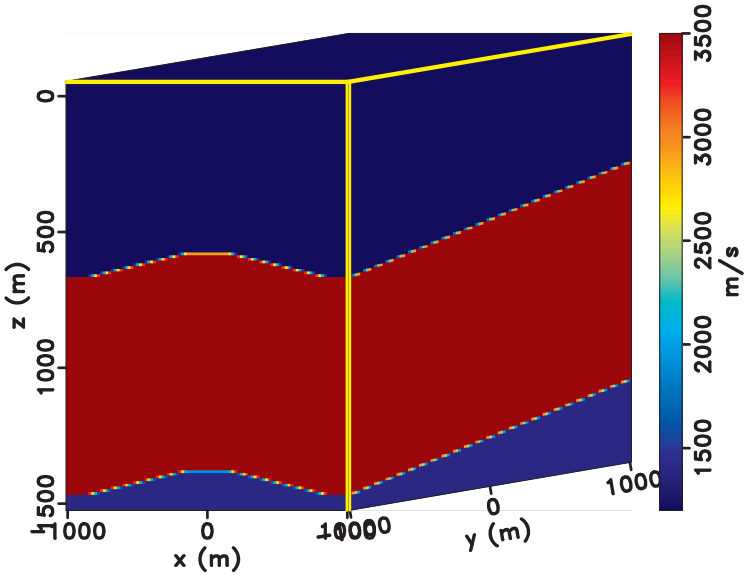

(b)

Figure 4.4: (a) The dipping velocity model, (b) The dipping density model.

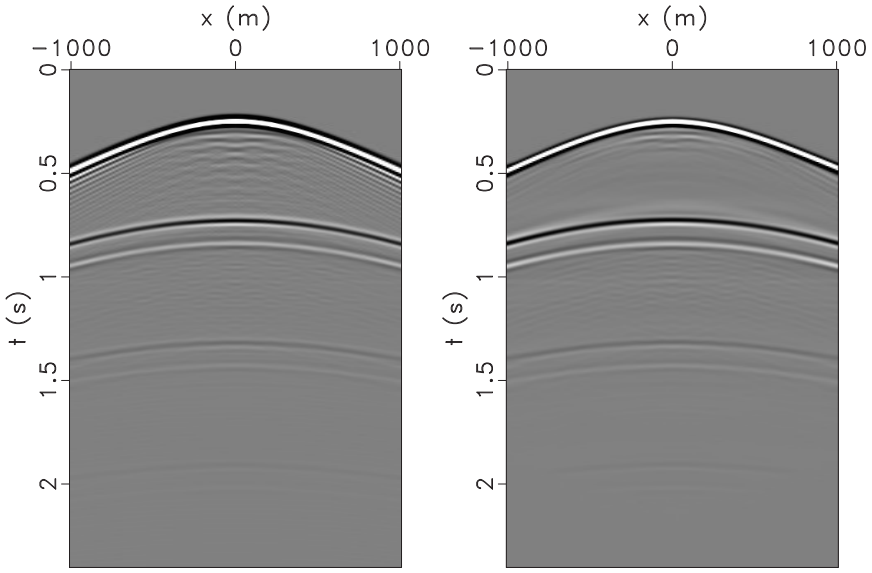

(a) (b)

Figure 4.5: In-line Green's function: (a) Green's function from a virtual source at $x = 0$ m and $z = 600$ m to a line of surface receivers at $y = 0$ m produced using finite-difference modeling, (b) Green's function on a line of surface receivers at $y = 0$ m retrieved with 3D Marchenko redatuming.

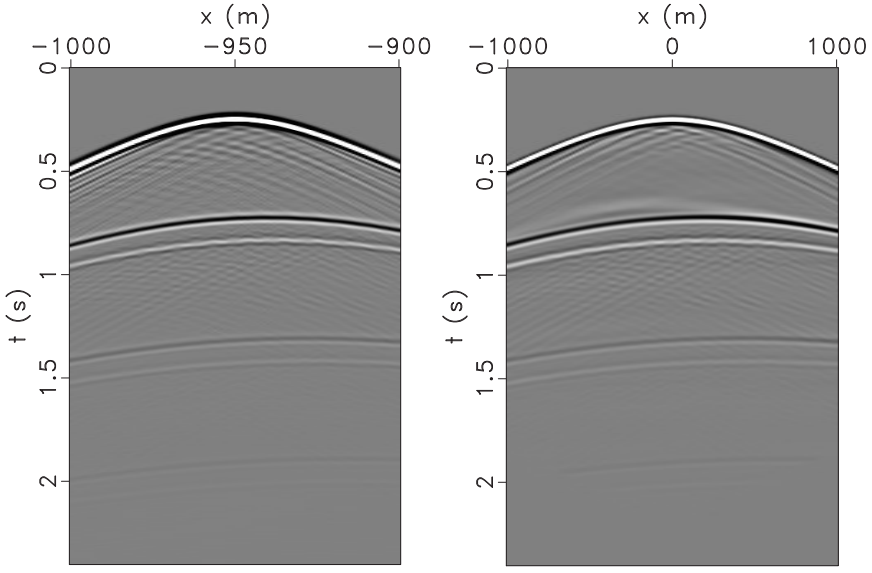

(a) (b)

Figure 4.6: Cross-line Green's function: (a) Green's function from a virtual source at $x = 0$ m and $z = 600$ m to a line of surface receivers at $x = 0$ m produced using finite-difference modeling, (b) Green's function on a line of surface receivers at $x = 0$ m retrieved with 3D Marchenko redatuming.

relatively complex 2D Gulf of Mexico model along another horizontal axis - y-axis. We use this model for a proof of concept and 2.5D geometry the model allows for 1) a reduction of the computational costs for surface data generation, as we create all the 3D shot gathers over a large surface area by generating the 3D surface shot records along one line in the middle ($y = 0\ m$) and use transnational invariance in the y-direction to create all other surface 3D shot gathers and 2) a relatively simple and intuitive process of analyzing and interpreting the reconstructed Green's function results as no out-of-plane reflections present. The grid of the model is 10 m by 10 m by 10 m along x (in-line), y (cross-line), and z (depth).

Surface seismic data are rarely acquired with fully, densely and regularly sampled sources and receivers in a practical 3D seismic survey. Three typical seismic data acquisition patterns, marine steamer data, land data and ocean-bottom seismic (OBS) data, have individual characteristics. In this study, we apply our 3D Marchenko algorithm with marine 3D streamer type of seismic data. The challenges in applying Marchenko to ocean-bottom type data are: 1) the receivers/nodes are placed on the water or sea bottom (which can be pretty rough), while the sources are excited near the sea surface. An extra redatuming to move the receivers to acquisition surface is needed as the Marchenko method requires sources and receivers to be placed on the same depth level, 2) the receivers of OBS data are usually sparsely and irregularly distributed on the water bottom. Application of the Marchenko methods to land data faces its own obstacles, such as complex near-surface structures, surface topography, sparse spatial sampling and poor signal-to-noise ratio. Meanwhile, the multiples generated on land are mostly downward reflected from non-planar surface (unlike being reflected from the water bottom in the marine environment), so the shape of the multiples involves both the topography of the earth surface and the multiple generators. This makes it more difficult to recognize and predict the multiples on land compared to offshore. Meanwhile, the interplay between statics, which are caused by uneven surface and non-uniform shallow layers, and surface multiples for land data is another complication (Wilkinson & Bale, 2014).

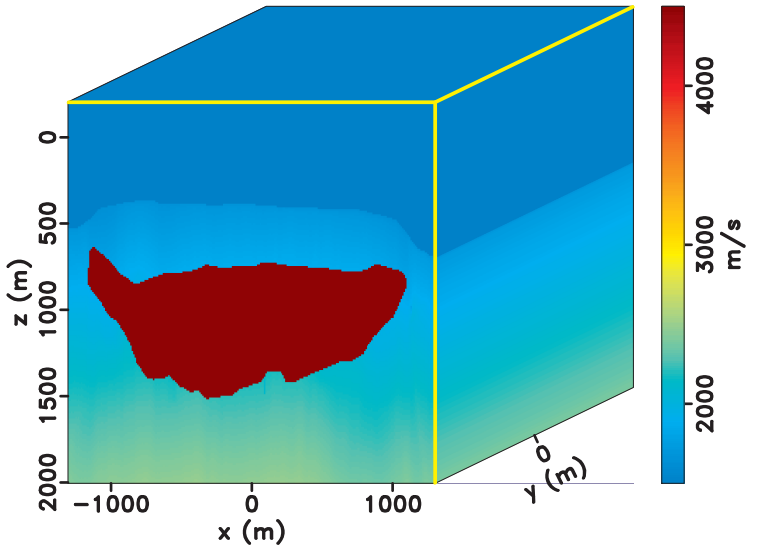

(a)

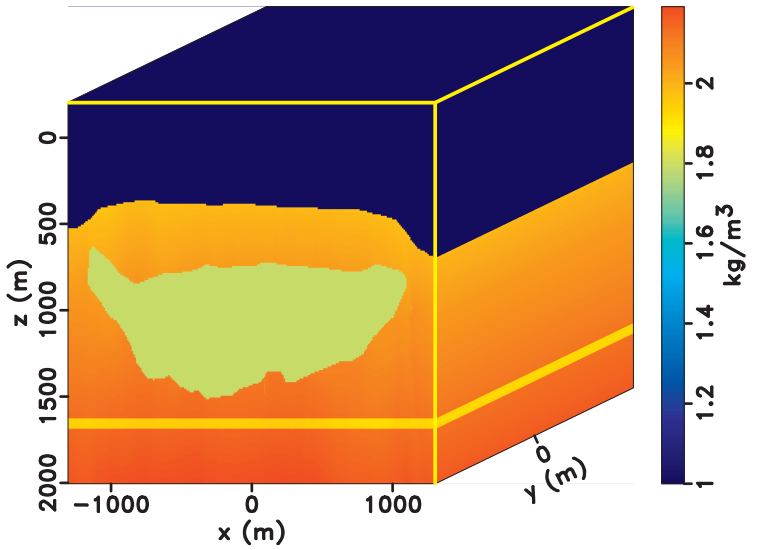

(b)

Figure 4.7: The 2.5D Gulf of Mexico velocity model (panel a) and density model (panel b).

In a 3D marine streamer seismic survey, data are acquired by survey vessels that traverse an area of the ocean following a series of parallel lines, trailing air gun arrays and hydrophone streamers as long as tens of kilometers. The typical marine acquisition is illustrated in Figure 4.8. We assume that the data acquired from a modern 3D marine survey contains, 1) long offsets along in-line direction, 2) dense spatial sampling along the in-line direction (e.g. 12.5 m). Yes the spacing of hydrophones along the cross-line direction is usually sparse (fourfold or more of the in-line spacing). The 3D Marchenko algorithm (equations 4.1, 4.2, and 4.3) involves the integration over an aperture of temporal convolutions and temporal cross-correlations of pairs of traces, therefore, both in-line and cross-line sampling density should be sufficiently fine to avoid having aliased energy contaminate the stacked trace. The desired sampling of the recorded data is determined by the condition: having at least four samples for the smallest wavelength.Therefore, interpolation is needed to overcome the sparse spatial sampling in the cross-line direction. We use B-spline forward interpolation to obtain densely sampled shot gathers from sparse surface data and we apply 8-point B-spline interpolation at each time sample.

A 3D surface shot gather with densely sampled receivers in shown in Figure Figure 4.9(a) shows, of which both in-line and cross-line sampling are 10 m. This is used as a reference 3D surface shot gather. We sub-sample the reference surface shot gather in both the in-line and cross-line directions to obtain a sparse shot gather shown in Figure Figure 4.9(b). We show the interpolated 3D surface shot gathers by 8-point B-spline interpolation in Figure Figure 4.9(c). To evaluate how the interpolation algorithms work, we compare three time slices at t=0.52 s, 0.68 s, and 1.00 s between the original densely-sampled shot gather and the interpolated shot gather by B-spline interpolation in Figure 4.10. The three panels in the last column, Figure 4.10(c), Figure 4.10(f), and Figure 4.10(i) depict the errors generated by B-spline interpolation at t=0.52 s, 0.68 s, and 1.00 s, respectively. The interpolation errors from B-spline interpolation are considerably small and most residuals appear at far offsets. Far offset errors are further suppressed as we apply a taper to the edges of the far

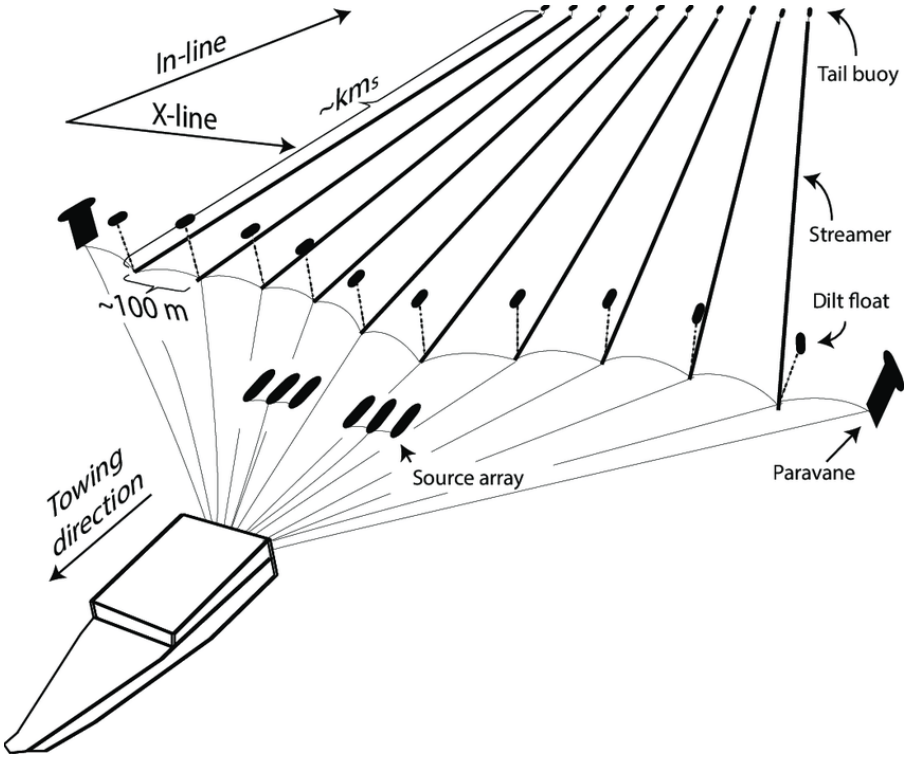

Figure 4.8: Illustration of the geometry of a standard towed streamer survey in marine seismic

offsets when calculating the source integrations in equations 4.1, 4.2, and 4.3 at the Green's function retrieval stage.

With 3D Marchenko redatuming, we retrieve the Green's function from a virtual source at $x = 0\ m$, $y = 0\ m$, and $z = 1500\ m$ to all the surface grid points. For this 2.5D model, the salt structure appears only along the x-direction and the layers are flat in the y-direction. We use a 2D slice of the 3D Green's function in the plane $y = 0\ m$ to demonstrate the signature of the 3D Green's function. Figure Figure 4.11(a) shows the in-line Green's function section simulated with 3D finite difference modeling with a source at $x = 0\ m$, $y = 0\ m$, and $z = 1500\ m$ and receivers along $y = 0\ m$. Figure Figure 4.11(b) shows the Green's function retrieved by 3D Marchenko redatuming algorithm with the densely sampled surface data and a background velocity model. Figure Figure 4.11(c) shows the Green's function retrieved by the 3D Marchenko redatuming algorithm with the sub-sampled surface data. With the sparsely sampled data as input, 3D Marchenko redatuming produces the Green's function that is severely aliased.

An in-line section of the 3D Green's function retrieved by Marchenko redatuming with the 3D data reconstructed by 8-point B-spline interpolation is shown in Figure 4.12(a) and the difference between Figure 4.12(a) and the reference Green's function Figure 4.11(b) in Figure 4.12(b). Figure 4.12(b) shows negligible residuals, indicating that the B-spline interpolation is efficiently accurate for 3D Marchenko redatuming,

4.5 Discussion and conclusions

It is efficient and convenient to perform the temporal convolution and cross-correlation in the Marchenko iteration algorithm in the frequency domain. For 3D Marchenko implementation, the input reflection response data, which is a 5D cube with axes of source positions (in-line and cross-line), receiver positions (in-line and cross-line), and frequency samples, needs to be loaded into the memory. The total numbers of sources/receivers are determined by multiplying the number of sampling points along the in-line direction with the number of sampling points along the cross-line direction. For example, if the sources/receivers are

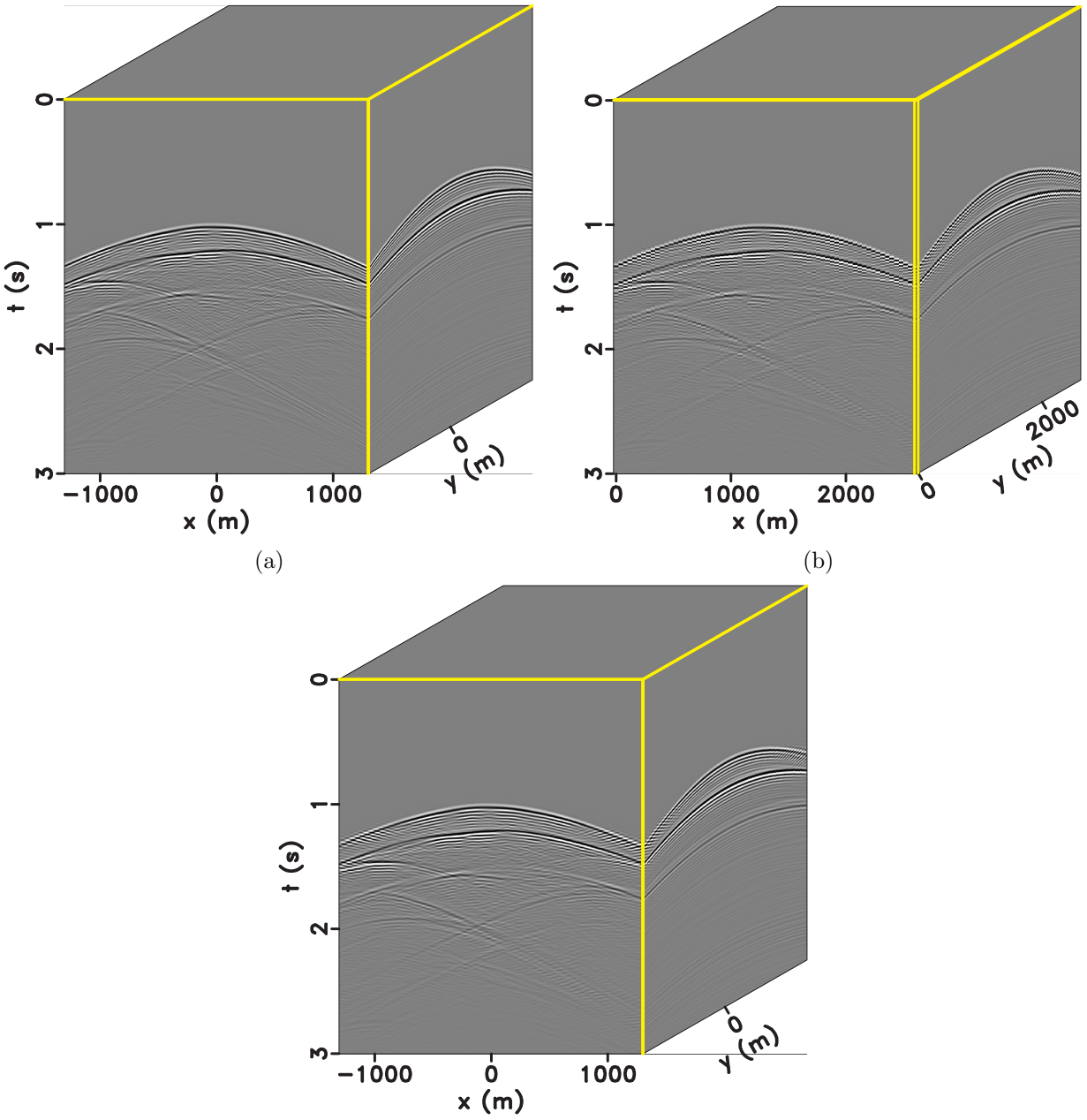

Figure 4.9: (a) A 3D surface shot gather with dense in-line and cross-line sampling. (b) Sub-sampled surface shot gather with sparse in-line and cross-line sampling. (c) Interpolated surface shot gather using 8-point B-spline interpolation method.

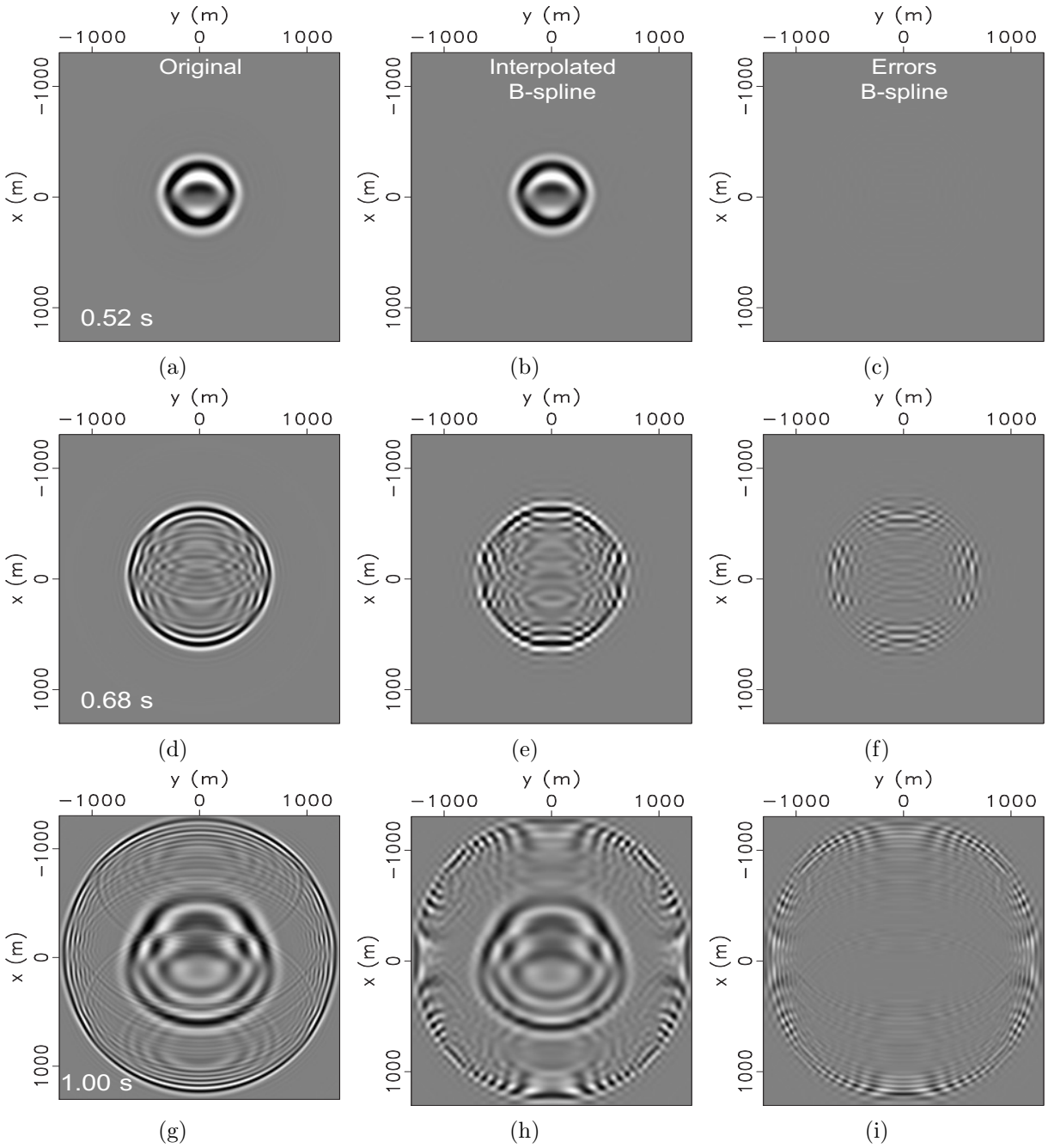

Figure 4.10: B-spline interpolation: Panels a, d, and g show the time slices of the directly simulated surface gather for 0.52 s, 0.68 s, and 1.00 s, respectively. Panels b, e, and h show the time slices of the interpolated surface gather by B-spline interpolation for 0.52 s, 0.68 s, and 1.00 s, respectively. Panels c, f, and i depict the differences between the interpolated surface gather and the direct simulated surface gather at 0.52 s, 0.68 s, and 1.00 s, respectively

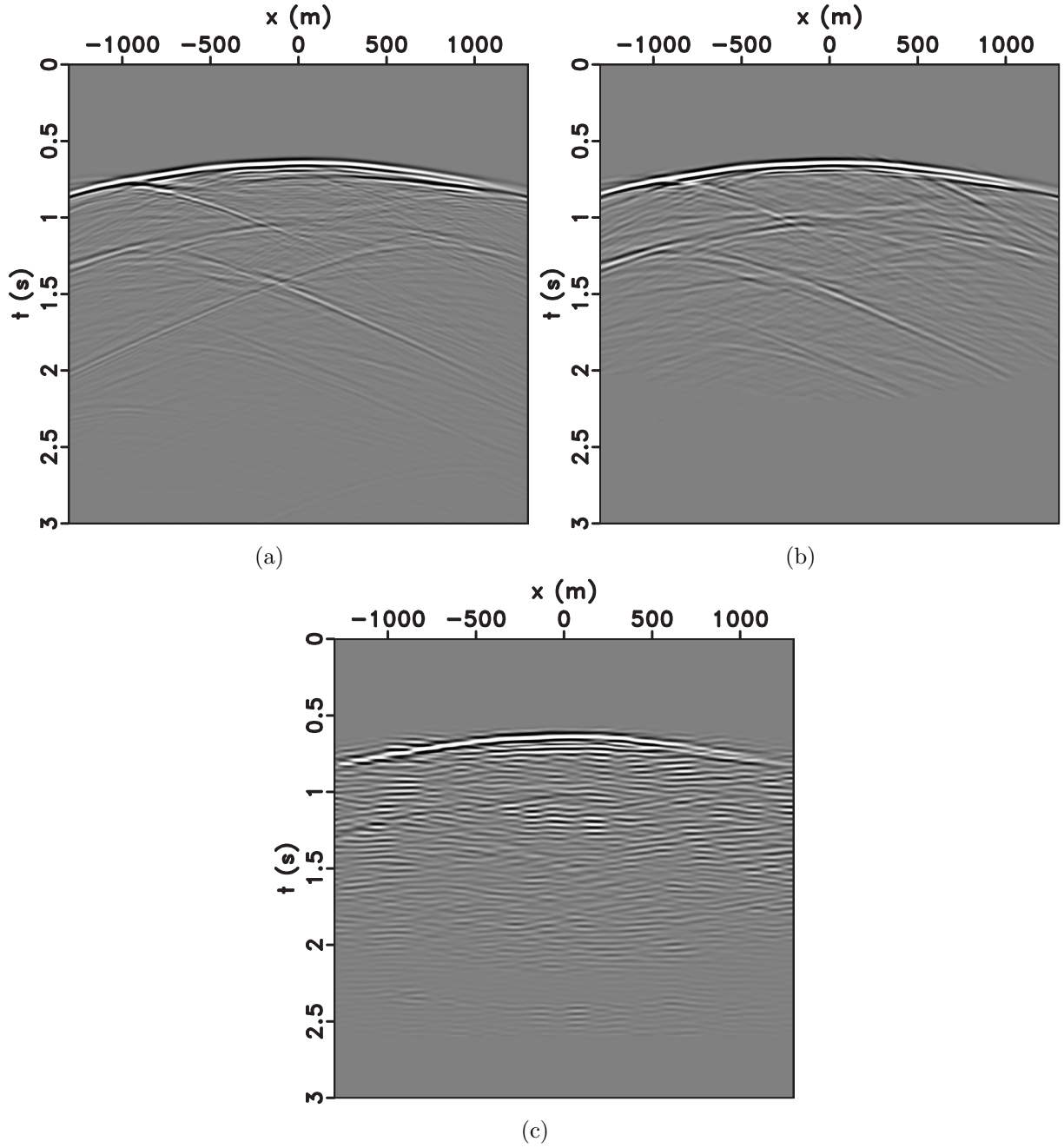

Figure 4.11: (a) In-line section of the 3D Green's function for a source at $x = 0\ m$, $y = 0\ m$, and $z = 1500\ m$ to receivers along $y = 0\ m$, simulated using 3D finite-difference modeling. (b) In-line section of the 3D Green's function retrieved by 3D Marchenko redatuming with densely sampled surface data. (c) In-line section of the 3D Green's function retrieved by 3D Marchenko redatuming with sparsely sampled surface data.

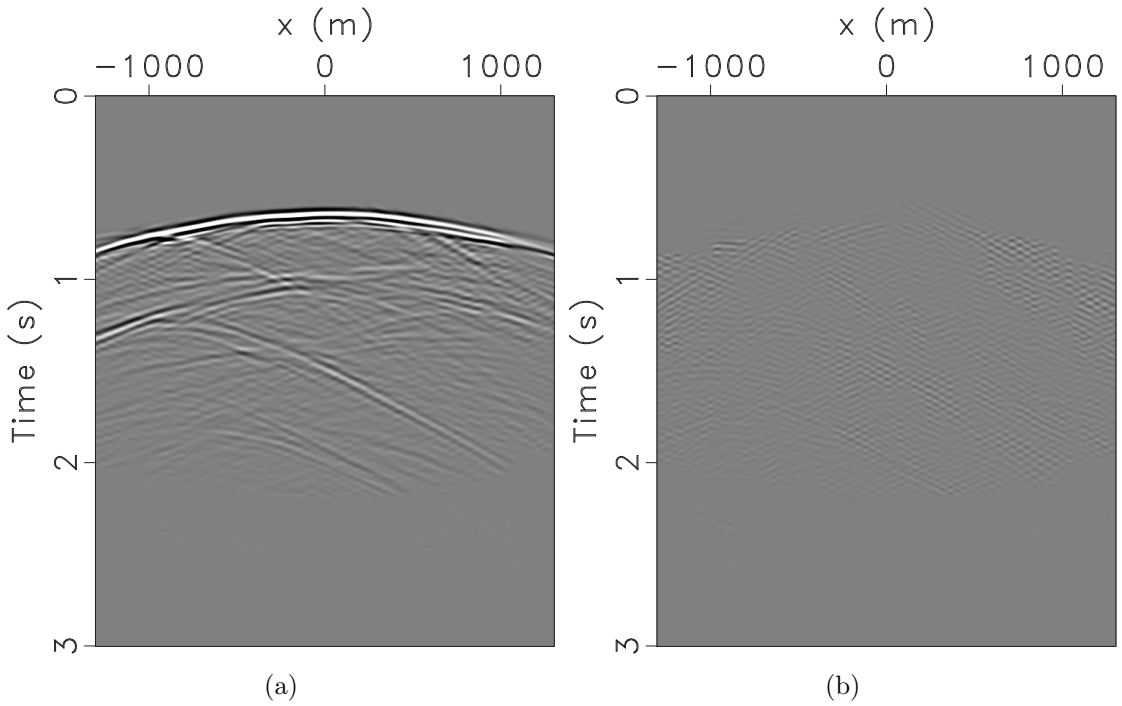

(a) (b)

Figure 4.12: (a) In-line section of the 3D Green's function retrieved by Marchenko redatuming with 3D interpolated surface data from 8-point B-spline interpolation. (b) The difference between (a) and the reference Green's function.

placed on a 200 grid lines by 200 grid lines area and we keep 200 frequency samples, the size of the 5D data cube is 2,560 GB, which is much greater than the memory capacity of a typical computing node (16 GB to 256 GB). Hence, the maximum memory of the computing node puts a limitation on the scale of the 3D problem that we can handle. Apparently, we first need to choose the spatial sampling as large as possible within the requirement for the Marchenko method so as to cover a larger area with same numbers of total sources/receivers. One general way to manage a larger area is to minimize the number of frequency samples. Standard fast Fourier transform tends to keep the frequency content from 0 Hz up to approximately 120 Hz; however, the highest meaningful frequency will be smaller (approximately 40-70 Hz) in most seismic imaging projects. In our examples, the highest frequency is approximately 40 Hz. Therefore, by muting the frequency samples higher than 40 Hz in the reflection response and conducting the convolution and cross-correlation from 0 Hz to 40 Hz, we reduce both the memory needed and the CPU time for loading the 5D cube by 66.7%. Meanwhile, the CPU time for computing the iterations for the Marchenko algorithm is also reduced by 66.7%. As the time-windowing is applied in the time domain, we pad the end of the inter-medium convolution and cross-correlation results with zeros to match with the frequency samples before muting. This approach allows us to handle medium size 3D projects using computers with a 256 GB memory. For large scale 3D projects, we might need to adjust the code to conduct numerical parallelization by frequency.

3D seismic data are almost never acquired with sources and receivers placed on the fully, densely and regularly sampling grids. In this study, we perform the cross-line data interpolation by means of the B-spline method for the 3D marine streamer type of data. For a complicated 3D data acquisition geometry, we may need to borrow the interpolation methods that have been deployed for 3D SRME, since both SRME and Marchenko methods involve computing the integration over the aperture of cross-convolutions of pairs of traces, and they both require the sampling density to be sufficient to avoid having aliased energy contaminate the stack trace. A comparison of the formulations of Marchenko and SRME

algorithm is presented in the following table:

SRME (R=$S^{-1} * D$)	Marchenko
$M_k = \int_{\partial D_0} R * P_k$	$M_k = \int_{\partial D_0} R \star f_k$
$P_{k+1} = P_0 - \int_{\partial D_0} R * P_k$	$f_{k+1} = f_0 + \int_{\partial D_0} R * M_k$
$P_0 = D$	$f_0 = \int_{\partial D_0} R * T_d^{inv}$

The symbol $\star$ represents the temporal cross-correlation and $*$ represents temporal convolution. The differences of these two algorithms are, (1) in the Marchenko framework, a direct arrival from virtual source location to surface T_d^{inv} needs to be computed , and (2) the iterative process includes both convolution and cross-correlation in the Marchenko framework, while only convolution is computed in SRME. However, as demonstrated in the above table, the requirement for the sampling and coverage of sources and receivers are very similar. Therefore, interpolation methods for 3D SRME, such as DMO-based interpolation and interpolation on-the-fly, are to be investigated and accommodated for 3D Marchenko redatuming in the future for 3D land and ocean bottom seismic data.

In summary, we reformulate the 3D Marchenko-type equations, which are then realized with numerical implementation. We propose an approach to determine the sufficient aperture and the spatial sampling of the source/receiver pairs required by the Marchenko redatuming algorithm. We revisit B-spline forward interpolation for the reconstruction of sparse 3D data that is often acquired in a practical marine streamer survey. We validate our numerical implementation of 3D Marchenko redatuming with a 2.5D Gulf of Mexico model and a 3D trapezoidal-dipping model. We show the 3D Green's function retrieved by Marchenko redatuming with the reconstructed data from B-spline interpolation is sufficiently accurate compared to the Green's function from a direct simulation.

4.6 Acknowledgements

This work was supported by the Consortium Project on Seismic Inverse Methods for Complex Structures at the Colorado School of Mines. We acknowledge Antoine Guitton for inspiring research direction of this work.

CHAPTER 5

SUB-BASALT MARCHENKO IMAGING WITH OFFSHORE BRAZIL FIELD DATA

Xueyi (Alex) Jia[1], Anatoly Baumstein[2], Charlie Jing[2], Erik Neumann[2], and Roel K. Snieder[1]

Prepared for submission to *Geophysics*.

5.1 Abstract

Sub-basalt imaging for hydrocarbon exploration is challenging because of multiple scattering, attenuation and mode-conversion when seismic waves encounter highly heterogeneous and rugose basalt layers. With densely sampled seismic data by modern acquisition and advanced imaging techniques, imaging through basalt becomes feasible. Yet, the strong internal multiples generated by the basalt layers and the seabed remains a challenge for conventional imaging techniques. If not properly handled during seismic imaging, internal multiples can be mapped below the basalt layers, overlapping with the hydrocarbon reservoirs, which could mislead the further geologic interpretations. Conventional methods for internal multiple elimination suffer from the requirements for accurate horizons of the multiple generators and/or a labor-intensive adaptive subtraction process. In Marchenko imaging, the artifacts related to internal multiples are mitigated directly without the need neither for picking the multiple generators nor for detracting the predicted multiples. The Marchenko method can produce seismic images that are comparable with the images by Reverse Time Migration in both positions and phases of subsurface reflectors, but are free from the nonphysical interfaces related to internal multiples, with a simply smooth velocity model. We propose a practical work flow for the preparation of typical marine streamer data and show that data regularization is crucial to the success of the Marchenko method. With a realistic synthetic

[1]Center for Wave Phenomena, Colorado School of Mines, 1500 Illinois St., Golden, CO 80401, USA
[2]ExxonMobil Upstream Research Company, Spring, Texas, USA

example, we show that far offset horizontally propagating waves can be reconstructed by Marchenko redatuming. We then show successful applications of the Marchenko method to sub-basalt imaging, with a realistic synthetic example and field data acquired from offshore Brazil. The nonphysical interfaces due to the strong internal multiples generated by the seabed and basalt layers are clearly eliminated in our field data example.

5.2 Introduction

The elimination of internal multiples has long been a challenging problem in seismic data processing. Strong internal multiples can be generated in a variety of subsurface environments. Particularly, for marine seismic surveys, the water bottom or seabed is one of the strongest interbed multiple generator due to the high velocity and density contrast between water and sediments. Generally, multiple-generating interfaces can be any interface with strong acoustic impedance, such as salt bodies, carbonates, volcanic intrusions, gas layers, etc. Because of the complexity (structural shapes and various impedance along the interfaces) of the internal multiples generators and the similar behaviour of internal multiples and primaries, the attenuation of the internal multiples remains challenging for seismic processing. Surface related multiple elimination (SRME) based methods do not necessary work when applied to suppress internal multiples. Internal multiples and primaries can have similar moveout, so that Radon-based methods are ineffective. Internal multiples and primaries can have similar frequencies and amplitudes, so that predictive filtering based methods may not work as well. And internal multiples and primaries can have similar dips, so that $f-k$ filters, tau-p filters, and migration methods implementing dip-discrimination techniques may also not be as effective.

Conventional seismic methods for imaging the earth's interior, such as Ray-based migration (e.g Kirchhoff migration): Beylkin (1985); Bleistein *et al.* (2001); Bleistein (1987); French (1975); Operto *et al.* (2000); Schneider (1978), one-way wave equation migration: Claerbout (1971); Hale (1991); Zhang *et al.* (2005), and two-way wave equation migration (Reverse Time Migration): Baysal *et al.* (1983); McMechan (1983); Whitmore (1983), rely

on the single-scattering assumption, which means these methods require that the recorded seismic data do not include waves that reflected more than once in the subsurface before reaching the receivers (for overviews of the conventional migration methods: Etgen *et al.* (2009); Sava & Hill (2009)). Geophysicists consider that the single-scattering assumption is valid for majority of the seismic data. Yet, multiples - the waves that reflected more than once in the subsurface - usually are present in seismic data. If strong internal multiples exist but are not properly handled, conventional imaging methods will map the internal multiples to a deeper location in the seismic image. Meanwhile, because the large impedance difference between the multiple generators and the surrounding sediments, hydrocarbons tend to be trapped beneath the multiple generators. When the artifacts due to the internal multiples overlay with the reservoir layer, which is often the case, geological interpretation for the seismic images can be extremely challenging. Therefore, a robust and effective method for handling the internal multiples is needed for from the oil and gas industry for exploration and production purposes.

One conventional workflow used in the oil and gas industry includes 1) predicting internal multiples and 2) removing them using adaptive subtraction in the data or image domain. Berkhout & Verschuur (1997) proposed an algorithm for the removal of internal multiples, which requires knowledge of the macro velocity model between the surface and the upper boundary of the multiple generating layer. Jakubowicz (1998) developed a more explicit internal multiple prediction method involving a two-trace convolution followed by a single-trace correlation. Many industrial internal multiple prediction tools are developed based on this idea. However, these tools require an accurate picking of the internal multiple generators (either by geophysicists or automated computer algorithms) and inevitably rely upon the adaptive subtraction for the attenuation of the internal multiples. Both horizon picking and adaptive subtraction are labor-intensive. Horizon picking suffers if the model is not accurate, and adaptive subtraction, which is usually performed in a least-squares sense, can damage primaries at the location where primaries and multiples interfere.

Marchenko imaging is a novel technique to produce multiple-free seismic images with only surface seismic data and a background velocity model (Broggini *et al.*, 2012, 2014b; Wapenaar *et al.*, 2014b). It provides a target-oriented image reconstruction specifically for imaging areas with complex structures that generates strong internal multiples. The core of the Marchenko frame work is the Marchenko receiver redatuming, which allows for an accurate reconstruction of both primaries and internal multiples (Broggini *et al.*, 2012; Rose, 2002; Wapenaar *et al.*, 2014b). The reconstructed wavefields are naturally separated into up- and downgoing components, which can be utilized to virtually move the surface sources to a redatuming level by means of multidimensional deconvolution (van der Neut *et al.*, 2011). With the redatumed sources and receivers, one can further perform imaging with various strategies and directly obtain multiple-free seismic images without performing multiple subtraction (Jia *et al.*, 2018; Singh & Snieder, 2017). Theory of the Marchenko framework has been extend to elastic data (da Costa Filho *et al.*, 2014, 2015; Wapenaar, 2014) ,the incorporation of free surface related multiples (Singh *et al.*, 2016a), and the handling of short-period Dukalski *et al.* (2019). Dukalski & de Vos (2017) presented two alternative methods to solve the Marchenko equations with the free surface multiples taken into account: LSQR (least squares) and a modified Levinson-type algorithm. Even though the Marchenko method is robust with respect to velocity errors and does not require a detailed velocity model (Broggini *et al.*, 2014a), it would be beneficial to make it completely data driven. Zhang & Staring (2018) proposed a modified Marchenko algorithm, where a truncation operator is used to make the method completely model-free. In order to relax the relatively strict requirement for the surface reflection data by Marchenko redatuming, Ravasi (2019) showed that if multi-component seismic data is used, one can perform Marchenko Green's function retrieval with sparse source sampling.

Besides theoretical developments, Marchenko imaging has been successfully applied with various field datasets. Ravasi *et al.* (2016) applied Marchenko imaging to an ocean-bottom cable survey recorded over the Volve North Sea field. Staring *et al.* (2017) show an adap-

tive double-focusing Marchenko imaging with a Santos Basin field dataset. Jia *et al.* (2018) demonstrated a practical work flow to perform Marchenko imaging with marine streamer data for subsalt imaging and showed that subsalt image produced with the Marchenko method was cleaner and more continuous compared to the RTM image using a Gulf of Mexico field dataset. Krueger *et al.* (2018) presented their internal multiple attenuation workflow based on the Marchenko framework for four pre-salt fields in the Santos Basin, Brazil. In this study, we demonstrate a successful application of the Marchenko method with a marine streamer dataset for sub-basalt imaging. The multiple generators are seabed and volcanic intrusions with rugose interfaces. This dataset provides a challenging geologic setting to test Marchenko redatuming and imaging. In the synthetic example section, we apply Marchenko imaging with a dataset that is generated using a velocity model and a density model that are inspired by the field dataset. We designed the synthetic experiment and use it to calibrate the amplitudes of the field surface data and to identify artifacts due to internal multiples. In the field data example section, we investigate the three major stages of the implementation of Marchenko imaging: 1) pre-processing, including data regularization and data calibration; 2) Marchenko redatuming or Green's function retrieval in the target area; and 3) multiple-free imaging. We discuss our work flow for data pre-processing in detail. We show a comparison between the Marchenko image and the RTM image, and discuss how the internal multiples are removed by the Marchenko scheme.

5.3 Methodology

In this section, we outline the methodology for the Marchenko framework. Given ideal data as input, the Marchenko imaging framework contains two major steps: Marchenko redatuming and imaging.

5.3.1 Marchenko redatuming

We use an iterative scheme for receiver redatuming which is adapted from the work of Broggini *et al.* (2014b) on the basis of the earlier theoretical Marchenko studies (Broggini

et al., 2012; Rose, 2002; Wapenaar *et al.*, 2014b). The heart of the Marchenko redatuming is the representation theorem. The convolution- and correlation-type representation theorem relates two wave states with different field, material, and source properties in heterogeneous media (de Hoop, 1988; Vasconcelos *et al.*, 2009; Wapenaar *et al.*, 2004). The two wave states we choose to relate by the representation theorem are, 1) wavefield A, a wavefield, which is injected at the surface, focuses at a pre-defined subsurface location at time zero and propagates only downwards shortly after the focusing time; 2) wavefield B, the actual wavefield in the subsurface corresponding to surface sources. Wavefield A is represented by the focusing function (upgoing component f^- and downgoing component f^+) which is defined in a modified medium that is reflection-free below the focusing level ∂D_i. Wavefield B is a the wavefield in the actual subsurface responding to surface seismic sources. At the focusing depth, wavefield B consists of the upgoing component G^- and downgoing component G^+ (referred to as up- and downgoing Green's functions in the following discussions). The upgoing wavefield is defined as the wavefield that leaves a virtual source at the focusing point in the upward direction, while the downgoing wavefield is the wavefield that leaves a virtual source in the downward direction (ray paths of upgoing and downgoing waves are indicated with G^- and G^+, respectively, in Figure 5.2).

Based on one-way representation theorems, the Green's function and the focusing function are related by (van der Neut *et al.*, 2015a; Wapenaar *et al.*, 2014b):

$$\begin{aligned} G^-(x_i, x_0, \omega) =& - f_1^-(x_0, x_i, \omega) + \int_{\partial D_0} R(x_0, x_0^{'}, \omega) f_1^+(x_0^{'}, x_i, \omega) dx_0^{'}, \\ G^+(x_i, x_0, \omega) =& [f_1^+(x_0, x_i, \omega)]^* - \int_{\partial D_0} R(x_0, x_0^{'}, \omega) [f_1^-(x_0^{'}, x_i, \omega)]^* dx_0^{'}, \end{aligned} \tag{5.1}$$

where $G^-(x_i, x_0, \omega)$ and $G^+(x_i, x_0, \omega)$ are the frequency domain up- and downgoing Green's functions, corresponding to a implusive point source at x_0 at the acquisition surface and receivers on a desired subsurface depth (x_i). The focusing functions $f_1^-(x_0^{'}, x_i, \omega)$ and $f_1^+(x_0^{'}, x_i, \omega)$ are the up- and downgoing parts of the solution for a specified wave equa-

tion whose wavefield focuses at the subsurface location x_i. $R(x_0, x_0^{'}, \omega)$ contains the earth's reflection response from a vertical dipole source at $x_0^{'}$ recorded by a pressure receiver at x_0. The multiplication is equivalent to convolution in the time-space domain, while * denotes complex conjugation.

One can solve for $G^-(x_i, x_0, \omega)$ and $G^+(x_i, x_0, \omega)$ by decomposing equation 5.1 into two time windows: $t < t_d$ and $t > t_d$, where t_d is the direct arrival travel time from the focusing point x_i to the surface. In the time window $t < t_d$, the Green's functions $G^+(x_0, x_i, \omega)$ and $G^-(x_0, x_i, \omega)$ are equal to zero. Decomposing f^+ into a direct wave T_d^{inv} and a following coda M^+ yields:

$$f_1^+(x_0, x_i, \omega) = T_d^{inv}(x_0, x_i, \omega) + M^+(x_0, x_i, \omega). \tag{5.2}$$

Substituting $f_1^+(x_0, x_i, \omega)$ in equation 5.1 with equation 5.2, we compute the focusing functions by the following iterative scheme in the time window $t < t_d$:

$$\begin{aligned} [M_k^+(x_0, x_i, \omega)]^* &= \int_{\partial D_0} R(x_0, x_0^{'}, \omega)[f_{1,k}^-(x_0^{'}, x_i, \omega)]^* dx_0^{'}; \\ f_{1,k+1}^-(x_0, x_i, \omega) &= \int_{\partial D_0} R(x_0, x_0^{'}, \omega) M_k^+(x_0^{'}, x_i, \omega) dx_0^{'} + f_{1,0}^-(x_0, x_i, \omega), \end{aligned} \tag{5.3}$$

with the initial value of f_1^- computed by

$$f_{1,0}^-(x_0, x_i, \omega) = \int_{\partial D_0} R(x_0, x_0^{'}, \omega) T_d^{inv}(x_0^{'}, x_i, \omega) dx_0^{'}; \tag{5.4}$$

where T_d^{inv} is the inverse waveform of the direct arrival from the focusing point to the surface. Note that T_d^{inv} is also the initial value of f_1^+, and T_d^{inv} is in practice approximated by Eikonal solver in this study. Finally, in the time window $t > t_d$, $G^-(x_i, x_0, \omega)$, $G^-(x_i, x_0, \omega)$ and $G^+(x_i, x_0, \omega)$ are obtained by substituting the $f_1^-(x_0^{'}, x_i, \omega)$ and $f_1^+(x_0^{'}, x_i, \omega)$ into equation 5.1.

5.3.2 Imaging

With the Green's functions obtained using the surface reflection data and the background velocity model, we are able to produce a multiple-free image with multi-dimensional decon-

volution (MDD). MDD is applied independently to each depth level using

$$\tilde{R} = \frac{\int_{\partial D_0} dx_0^{"} \int_{-\infty}^{\infty} G^+ \star G^-}{\int_{\partial D_0} dx_0{"} \int_{-\infty}^{\infty} G^+ \star G^+ + \epsilon}, \tag{5.5}$$

where $\int_{\partial D_0} dx_0^{"}$ represents the integration over surface source/receiver pair locations, G^+ represents the downgoing Green's function and G^- represents the upgoing Green's function. The symbol $\star$ represents cross-correlation, and ϵ represents a stabilization parameter. When ϵ approaches infinity, MDD is equivalent to a cross-correlation imaging condition applied between the up and downgoing Green's functions.

The redatumed reflection response $\tilde{R}(x_i, x_i^{'}, \omega)$ can be used with different strategies for imaging (Singh & Snieder, 2017). One strategy is to obtain the full reflection response by redatuming the sources and receivers at the same depth level, and produce seismic images below the redatuming depth level using established imaging algorithms (e.g. RTM) with the redatumed data. Note that a velocity model for the areas below the redatuming depth level is still needed in the imaging stage when performing conventional imaging methods with the redatumed data.

An alternative imaging strategy is adopted for this study. For every image point inside a target zone, we extract the zero-offset and zero-time component $\tilde{R}(x_i, x_i, t = 0)$ from the redatumed reflection response $\tilde{R}(x_i, x_i^{'}, t)$, and construct an image of the zero-offset reflectivity using

$$I(x_i) = \tilde{R}(x_i, x_i, t = 0). \tag{5.6}$$

With this imaging condition, we can compute the reflectivity of every image point in a target zone. This imaging strategy is more robust because it does not create the artifacts from the local internal multiples below the redatuming level, but it comes with an additional cost of performing Marchenko redatuming and MDD for each depth level inside the target area. Note for both imaging strategies mentioned above, no multiple generator picking or adaptive subtraction is performed.

5.4 Synthetic examples

We validate Marchenko imaging with a realistic synthetic experiment which is inspired by a field dataset. This synthetic example helps us to identify the major internal multiple generators and understand the artifacts associated with internal multiples that can be generated when applying conventional imaging method to the original surface data. The synthetic data is also used to calibrate the field data that is used for the field example. We first compare the Green's function retrieved with the Marchenko method with the wavefield generated from direct simulation and recorded at the surface. We discuss the horizontally propagating waves in the Green's function that can be reconstructed with Marchenko redatuming when the refractions are included in the surface data. We then perform Marchenko imaging with the retrieved Green's functions in a target zone to generate a multiple-free image and analyze this image by comparing it with an image produced with Reverse Time Migration (RTM).

5.4.1 Marchenko redatuming vs finite-difference modeling

Figure 5.1a shows the background velocity model estimated from an offshore Brazil field dataset. The velocity model is so strongly smoothed that the water layer smears with the sediments at the seabed. Figure 5.1b shows the corresponding density model we use for this example. The density model consists of the complex subsurface structures. It is designed and built by following the steps 1) we use Gardner's relation to convert the smooth velocity model (Figure 5.1a) to a smooth density model, 2) we migrate the surface dataset acquired over the target field where considerable amount of basalt layers exist, generating a reflectivity image, 3) we mute the deeper parts of the reflectivity image (right below the main volcanic intrusion layers) while keeping the shallow interfaces, including several multiple generators, 4) we apply weighting factors on both the smooth density model and the reflectivity model then add them together, and 5) we insert a dipping high density layer along the dipping multiple generator and a horizontal strong density contrast at the bottom of the model.

Step 3 ensures that every reflector in the image below the muted depth is caused by an improperly imaged internal multiples. In step 5, a high density contrast is inserted in the model to ensure that strong internal multiples can be generated and a flat density contrast is inserted at the bottom of the model to mimic a deeper reservoir layer that is seen in the field data image. The strong dipping contrast helps to identify internal multiples in the data and evaluate our multiple elimination scheme. The deep flat reflector serves as an imaging target and helps to test if our multiple-free imaging algorithm works effectively when internal multiples interfere with primary events. The grid of the model is 5 m by 5 m (along x and z directions). The spacing between neighbouring surface shot/receiver pairs is 20 m for the surface data simulation. The total number of co-located shots/receivers are 734.

Putting a virtual source below the dipping reflector (location of the virtual source is shown in Figure 5.2), we expect the following events to be recorded by the surface receivers: 1) the direct arrivals from the virtual source to the acquisition surface, 2)a primary event with a ray path that propagates downwards from the virtual source and then reflected upwards by the deep flat reflector (Note that this event is counted as a primary because it only incurred one reflection along its travel path), 3) the upgoing Green's functions, which follow the ray paths that went upwards initially from the virtual source and incurred at least two reflections at the seabed and the multiple generators, and 4) the downgoing Green's functions, which follow the ray paths that initially propagates downwards from the virtual source and incurred multiple reflections at the seabed and other multiple generators. The ray paths of all the events mentioned are illustrated and labelled in Figure 5.2.

Figure 5.3 shows a comparison between the Green's function reconstructed by the Marchenko method (labelled with "Reconstruction") and the directly simulated Green's function (labelled with "Direct simulation"). Due to the large aperture of the data acquisition, substantial refractions are recorded in the surface data at far offsets. According to the requirement of the Marchenko method, we mute the far offsets in the surface shot gathers to ensure the removal of refractions in the data. Comparing the "Reconstruction" and "Direct simula-

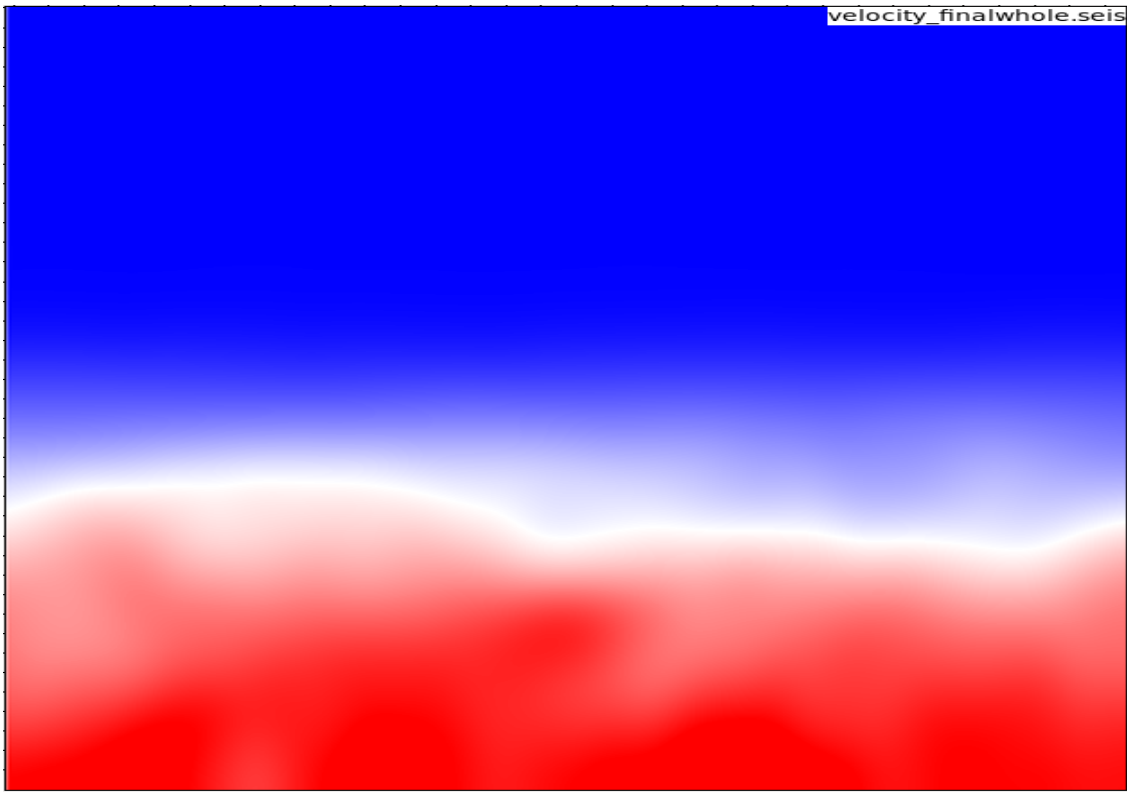

(a)

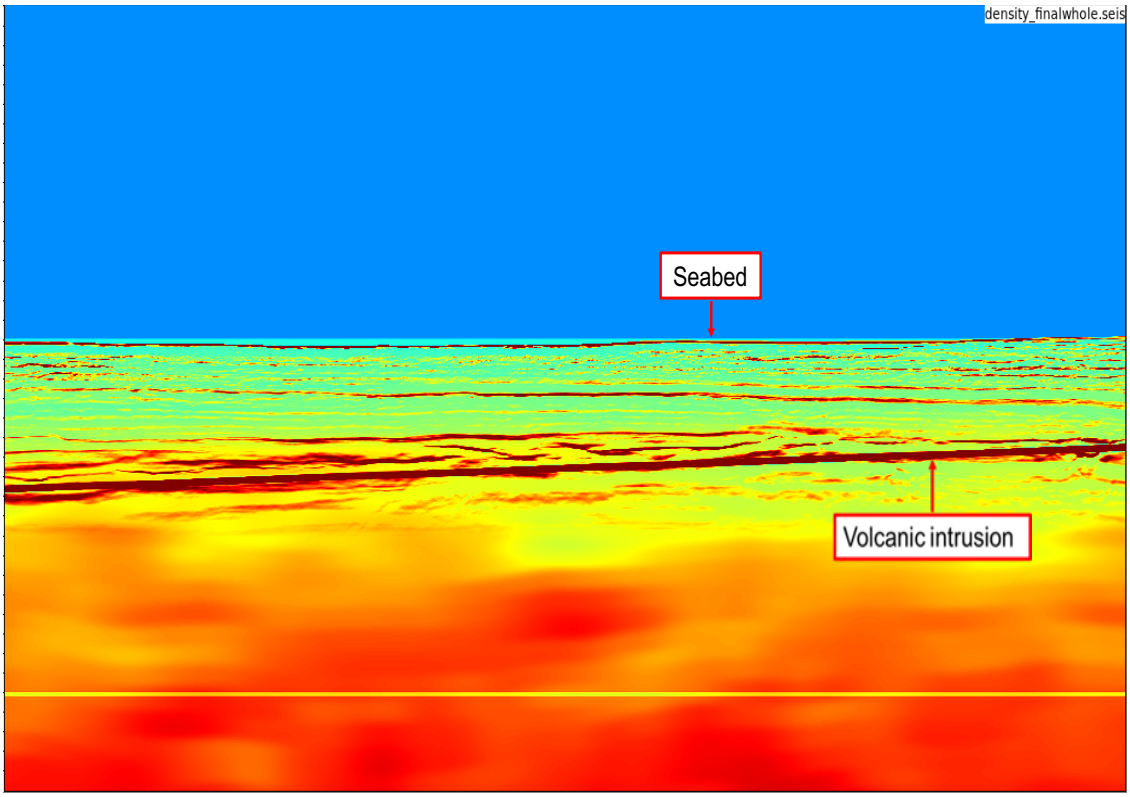

(b)

Figure 5.1: The velocity model (panel a) and density model (panel b) of the synthetic example. The velocity model is so strongly smoothed that the water bottom smears with the sediments.

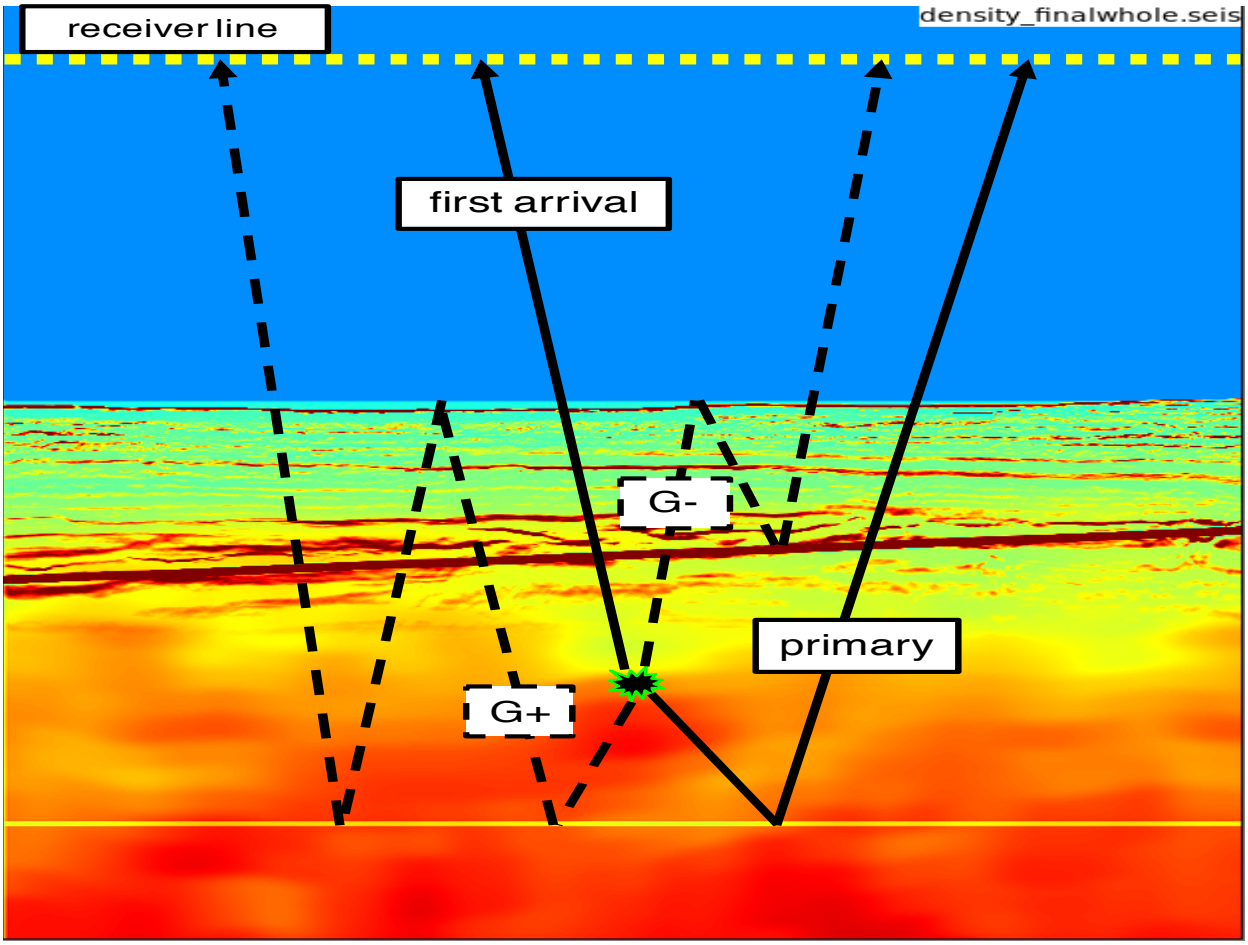

(a)

Figure 5.2: The ray paths of the four different kinds of events that are recorded at the surface receivers from a subsurface virtual source

tion" in Figure 5.3, the near offsets of the Green's functions match well, as shown in the comparison of the two overlapped traces extracted from the middle of the Green's functions (the far right panel in Figure 5.3). Some horizontally propagating events that appear at the far offsets in the "Direct simulation" panel are not properly reconstructed by the Marchenko algorithm. This is due to the fact that we mute the far offset events from the surface data.

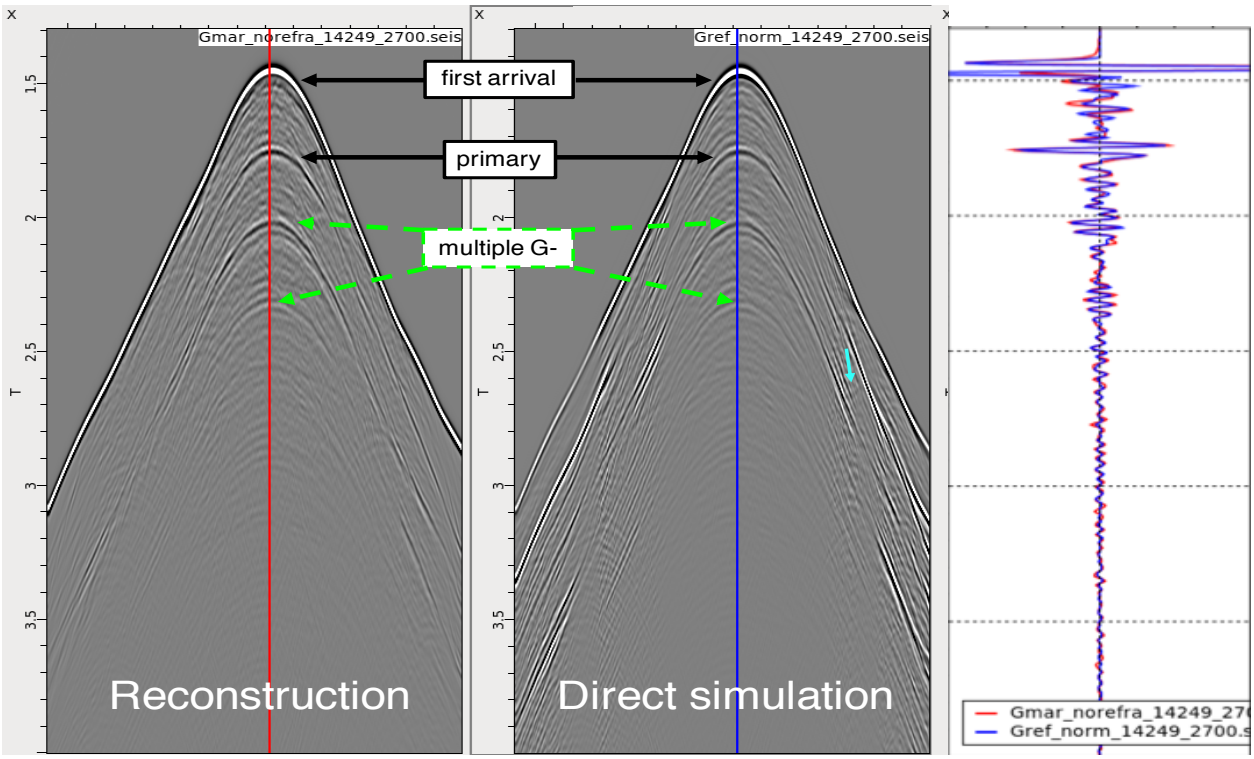

(a)

Figure 5.3: A comparison between the Green's function reconstructed by the Marchenko method and the directly simulated Green's function.

To further explore if the Marchenko algorithm is able to reconstruct the waves that incurred horizontal propagation along ray paths, we performed Marchenko redatuming with the original surface data with full offsets. Figure 5.4 shows the comparison of a) the Green's function reconstructed with the surface data with only reflections, b) directly simulated Green's functions, and c) Green's function reconstructed with the surface data of full offsets (including both reflections and refractions). With far offsets muted in the surface data, we obtain a good reconstruction of the near and middle offsets but get artificial events that look

continuous with near offsets but do not match the "direct simulations" (Figure 5.4b) at far offsets. With the full surface data, we obtain good reconstruction at the far offsets, which are horizontally propagating waves. After a scrutiny of the snapshots of the wavefields from the direct simulation, we are able to determine the ray path of the horizontally propagating events of Figure 5.4b and Figure 5.4c at far offsets, which is demonstrated in Figure 5.5. In sum, we show the reconstruction of the horizontally propagating waves in the Green's function by the Marchenko method. How to better utilize the reconstructed far offset waves remains an open research topic.

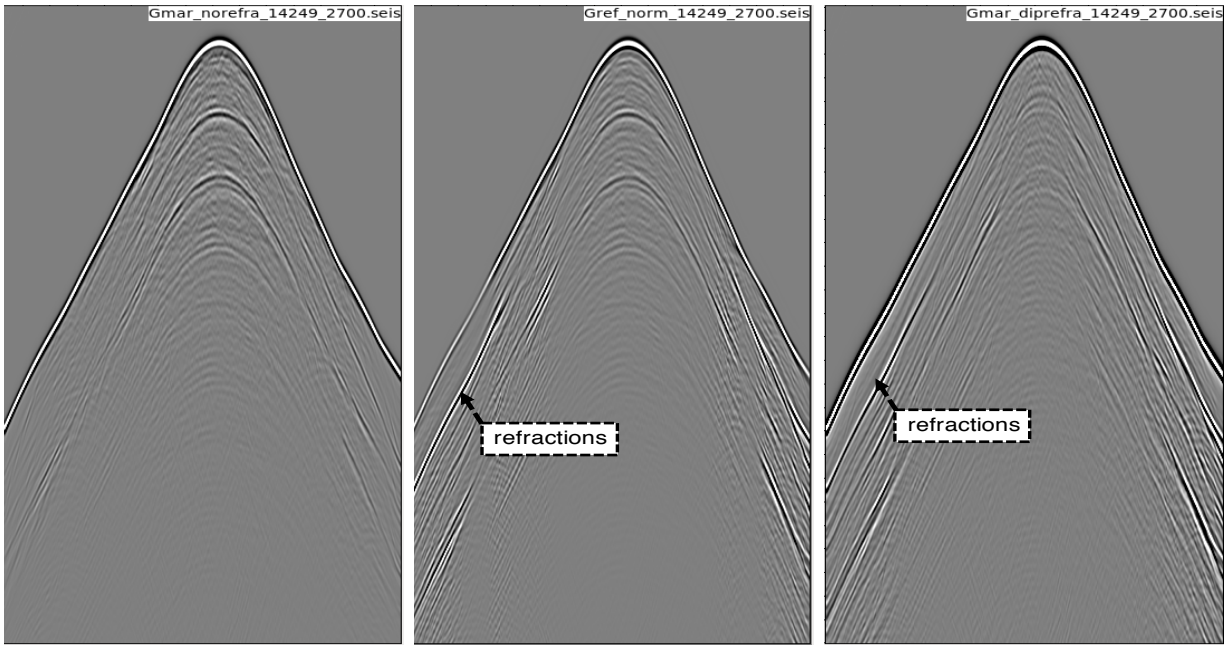

(a) (b) (c)

Figure 5.4: (a) Green's function retrieved by Marchenko algorithm using the data without refractions (b) Green's function by finite-difference modeling (c) Green's function retrieved by the Marchenko algorithm using the data of full offsets

To better reveal the artifacts due to internal multiples in the RTM image, we perform RTM with data of different offsets: full offsets with refractions muted, medium offsets from -2 km to 2 km, and near offsets from -500 m to 500 m, as shown in Figure 5.7 from left to right, respectively.

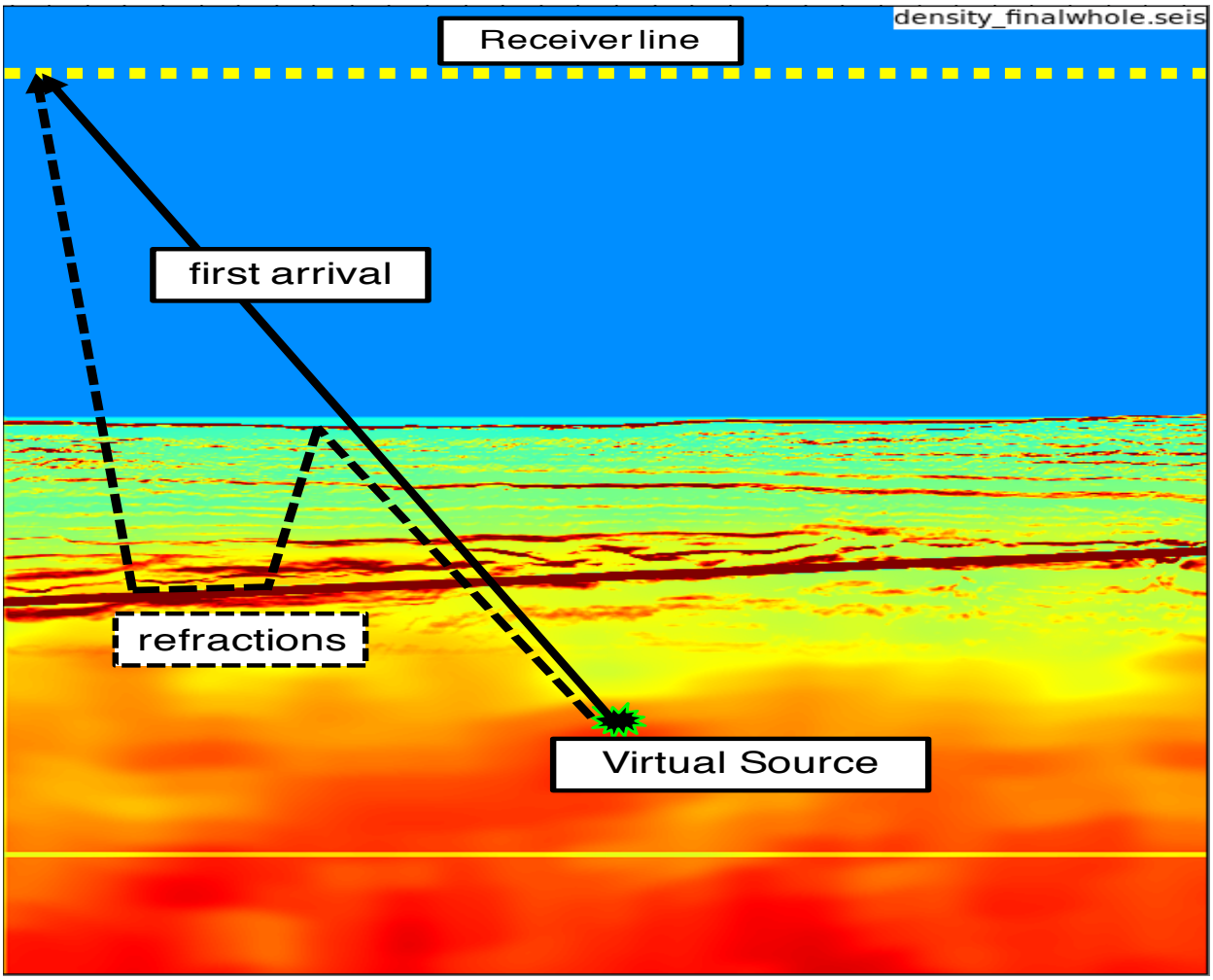

Figure 5.5: Ray paths of the horizontally propagating events in Figure 5.4b and Figure 5.4c

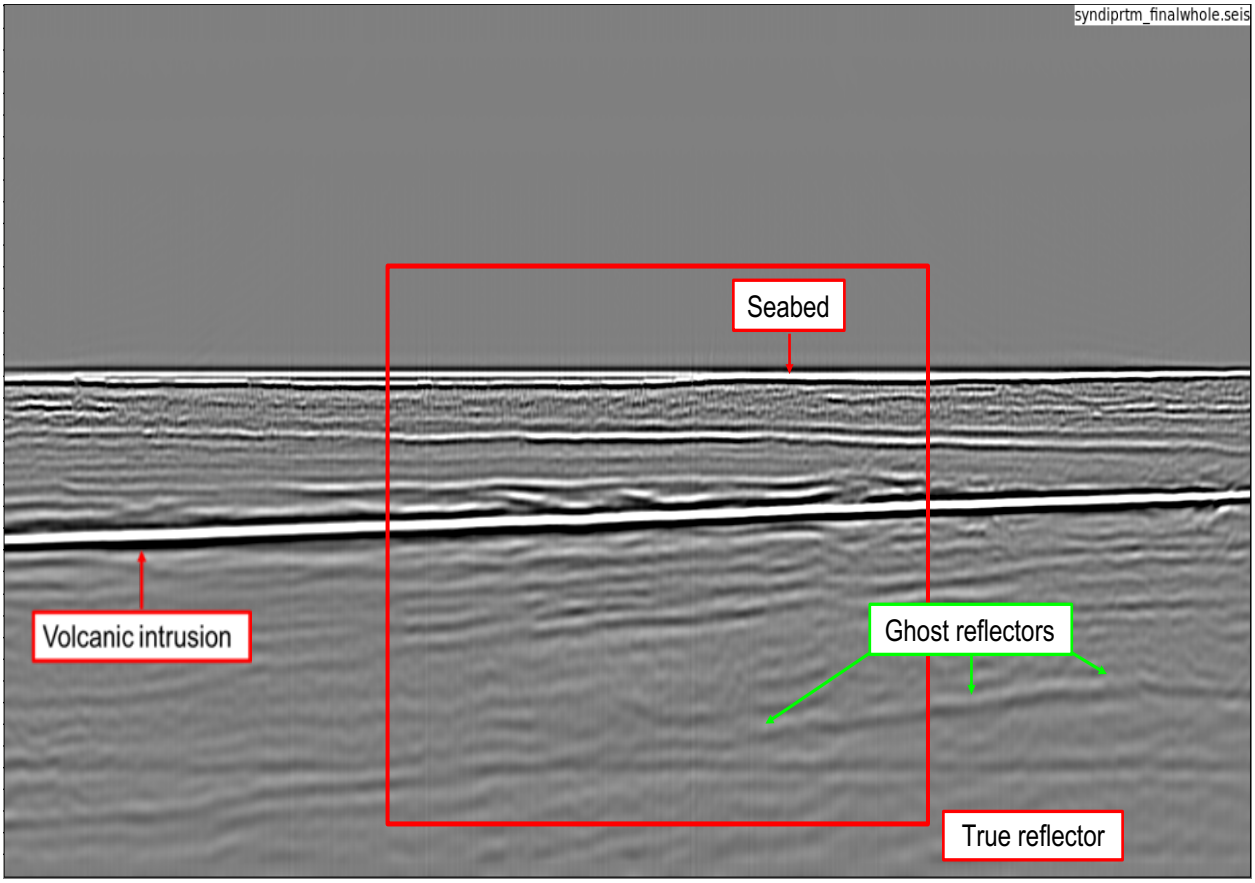

(a)

Figure 5.6: RTM image of the whole model. Red box indicates the target area where Marchenko imaging is applied.

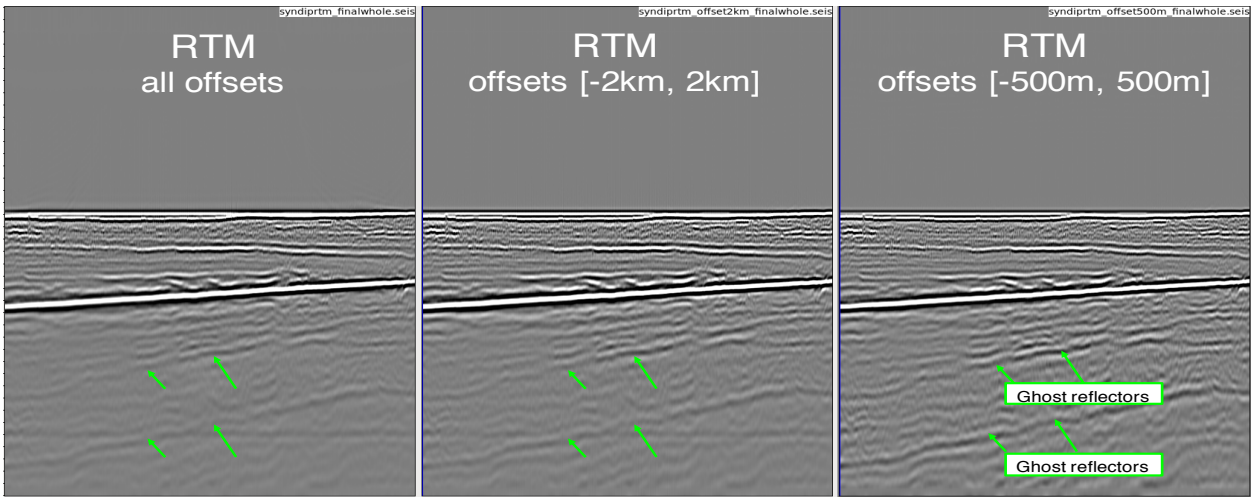

Figure 5.7: RTM images produced with data of various offsets

We show the RTM image of the whole model in Figure 5.6. True subsurface structures, the seabed, the volcanic intrusions and the deep flat reflector, are labelled and denoted by the red arrows. Some of the multiple-related artificial interfaces or ghost reflectors are labelled and denoted by the solid green arrows. The target area of this model is denoted with the red box. Next, we apply Marchenko imaging in the red box and compare it with the RTM image of the same area. We first reconstruct the Green's functions at each depth level inside the red box in Figure 5.6. Then we apply MDD independently to each depth level following equation 5.5. To evaluate and calibrate the Marchenko image produced by MDD, we compare it with the image produced by RTM. The consistency of the phase of a reflector and the relative phases between different reflectors are important information for seismic interpretation. Hence, it's desirable that the images produced with different methods are comparable in phase for the same reflectors. For the MDD method, the selection of ϵ plays an important role in keeping the phase of Marchenko image consistent with RTM image. The proper value of ϵ can be case-dependent. A rule of thumb is that ϵ should be within the range of 0.1 to 1 of the maximum value of the first term in the denominator.

We show the RTM image of the target area in Figure 5.8 and the Marchenko image of the same area in Figure 5.9. The images are produced with same surface dataset and same background velocity model. The red arrows denote the true structures, the seabed, the volcanic intrusions and the deep flat reflector, while the solid green arrows denote several nonphysical interfaces associated with internal multiples that are generated by the seabed and the intrusions. The dashed green arrows indicate a shallow smile-shaped true reflector and its corresponding deeper ghost artifacts. The RTM image is contaminated with multiple artifacts in the deeper area, as only the flat reflector should appear in the deeper area of the model but we see many ghost interfaces. The flat deep reflector is destructed and distorted by these ghost reflectors in the RTM image. While matching well with the RTM image in the shallow portion of the model, the Marchenko image is much cleaner in the deeper area with the flat reflector much better imaged.

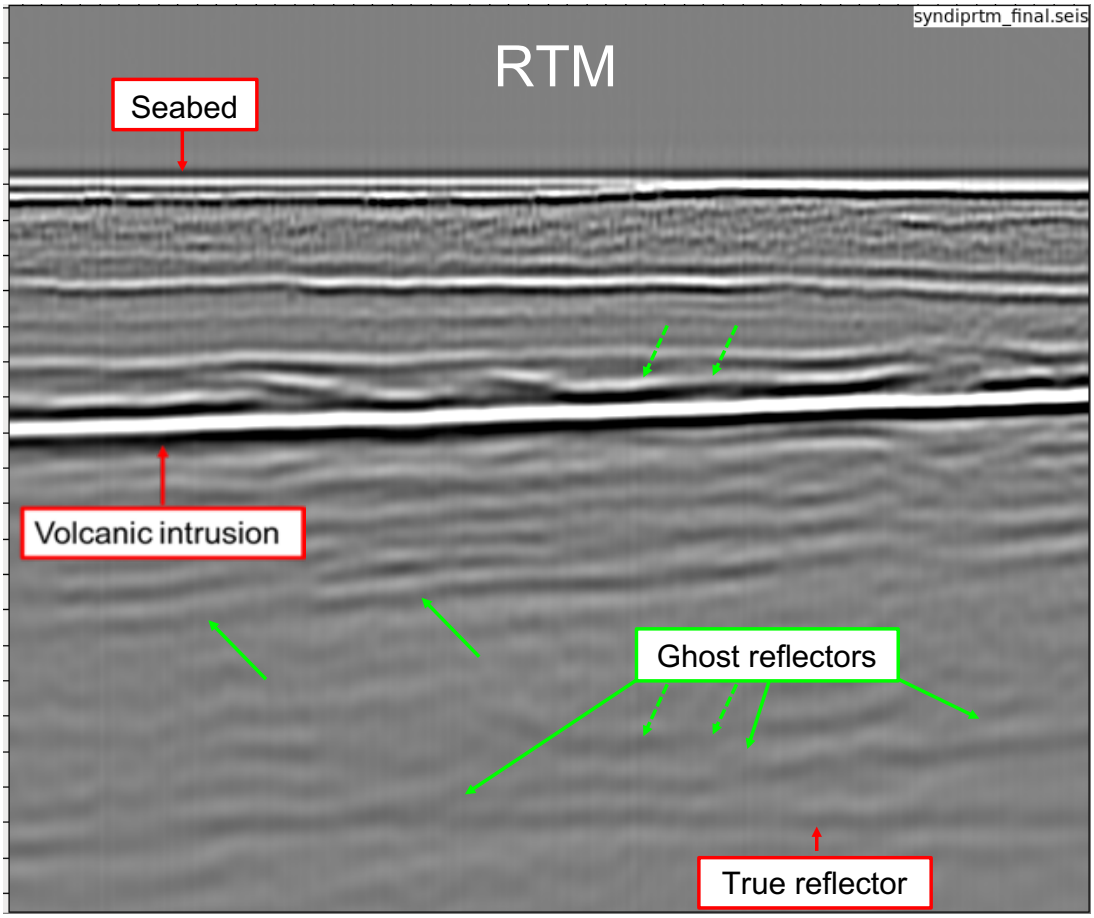

(a)

Figure 5.8: RTM image of the target area.

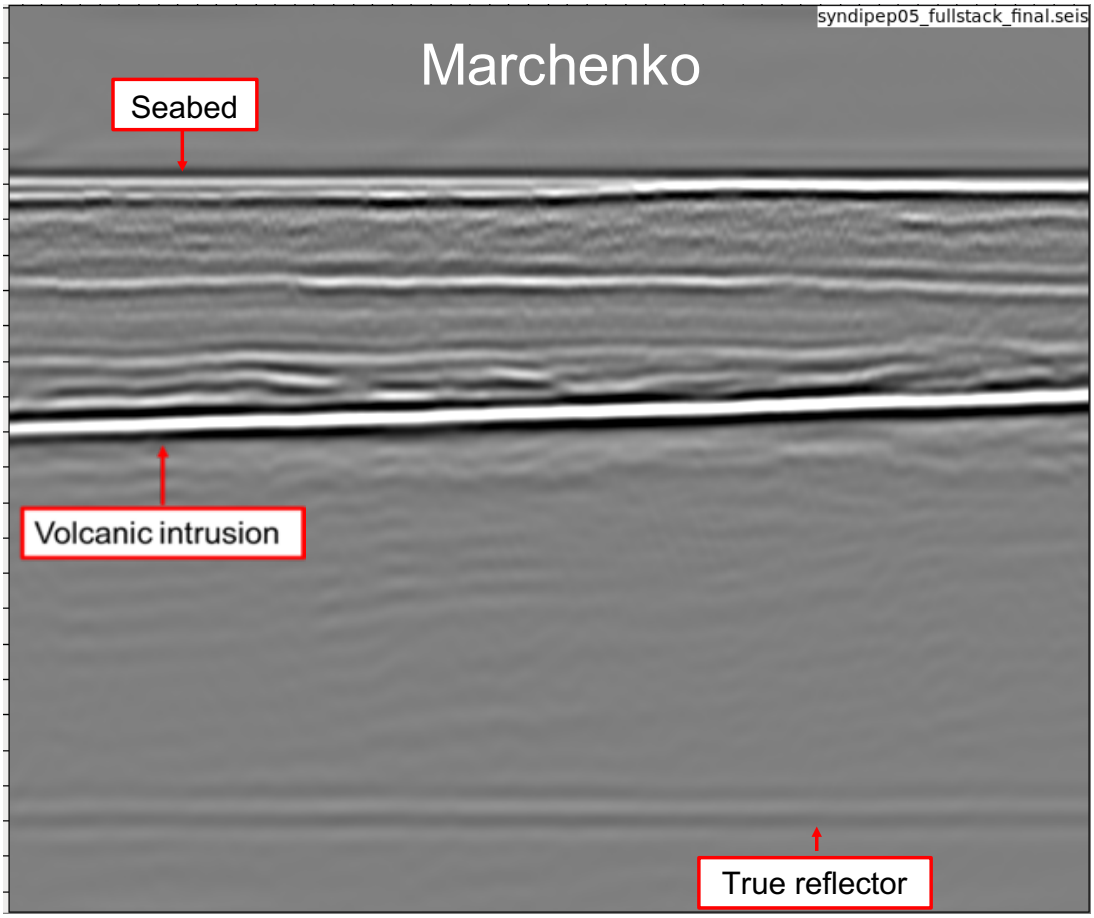

(a)

Figure 5.9: Marchenko image of the target area.

5.5 Field data example: offshore Brazil

We implement Marchenko imaging to a 2D marine field dataset acquired offshore Brazil. We aim to test the Marchenko method for imaging ultra-deep reflectors beneath sub-basalt or volcanic intrusion layers, as the field of interest is occupied by volcanic intrusions which can generate strong internal multiples.

5.5.1 Data regularization

We propose a practical work flow to apply Marchenko imaging to marine streamer data (Figure 5.10). In this case, we remove the surface-related multiples by muting the data after certain recording time, as the surface-related multiples appear at much later time than the primaries and first order internal multiples in this deep sea environment. In the left branch of the work flow in Figure 5.10, we prepare the surface data to make it adequate for the Marchenko redatuming algorithm, which requires the surface data to be recorded by equal number of co-located sources and receivers spreading on the acquisition surface. In order to regularize the data, we first extrapolate the data for near offsets, which can be achieved with existing SRME data regularization tools. We then sort the data into CMP-offset gathers and interpolate the data in offset, populating the offset spacing to a denser grid. At this point, the CMP-offset gather is still one-sided. To created two-sided data, we copy the one-sided offsets in each CMP gather, flip the sign of the offsets and place them onto the other side of that CMP gather. In this way, we are able to obtain the CMP-offset gathers with two-sided offsets. We resort the CMP-offset gathers to shot-receiver gathers, successfully recreating the regularized data with equal numbers of densely sampled and co-located sources and receivers. The dataset naturally has fixed offset length in each shot gather, as the length of the cable towed by the streamer is fixed. The Marchenko algorithm requires the input - the surface shot gathers to be recorded by fixed receivers sampled along the whole acquisition surface of the velocity model in the target area. To meet this requirement, after muting the refractions in the data, we convert the shot gathers with fixed offsets to the shot gathers

with fixed receives by windowing or padding with empty traces.

On the other hand, as shown on the right branch of Figure 5.10, we obtain the time-reversal of the first arrival by first computing the direct arriving time based on a smooth velocity model (Figure 5.1a) and then placing a Ricker wavelet at the arriving time of each surface receiver. Based on the iteration algorithm we adopt (equation 5.3), we need to calibrate the amplitude of the surface dataset in such way that after its convolution or correlation with the first arrival (Ricker wavelet) in the frequency domain, the maximum value of the convolution or correlation should be around one and won't get dramatically magnified or decreased over iterations. In this field example, we neither have information about the amplitude of the original source functions nor of the seismic pre-processing steps (e.g. noise attenuation and gaining) that the surface data has gone through. We calibrate the data by comparing the maximum amplitude of the primary reflections from the seabed of the field data with the equivalent events in the synthetic data that generated in the previous example with the synthetic velocity (Figure 5.1a) and the density (Figure 5.1b) models. It is feasible to use the synthetic data to calibrate the field data because, the first arrivals we use for the field data is exactly the same as what we use for the synthetic example, so the amplitudes of the surface data in both scenarios should be comparable. With such an approach, we obtain a constant scaling factor and apply it to all field shot gathers. This is a simple yet practical way to calibrate the field surface dataset and provides relatively accurate results.

There will be inaccuracies introduced following the above data regularization process. For example, the shots and receivers can never be strictly sampled on a perfect 2D line in field seismic acquisitions. But the Marchenko algorithm (equation 5.3) involves integrations over source locations, which is a process of stacking thousands of traces to reconstruct one trace. The inaccuracy introduced in data regularization is reduced in the stacking process and should be acceptable to a large extent. Figure 5.11 demonstrates one shot gather after our data regularization work flow.

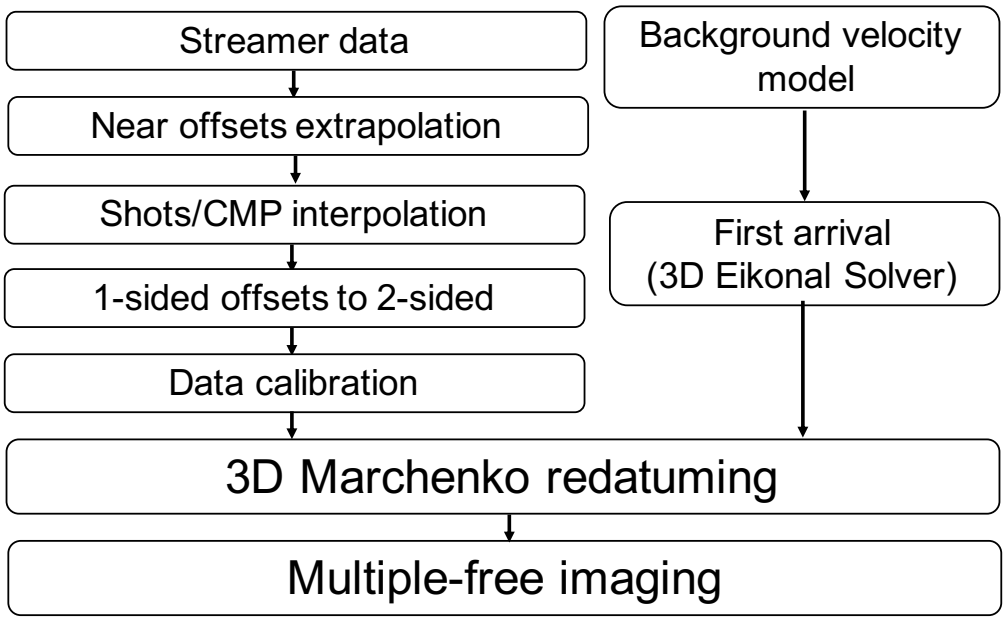

Figure 5.10: Workflow to apply Marchenko imaging to field data.

5.5.2 Field data images: Marchenko imaging vs RTM

Figure 5.12 shows the RTM image produced with the regularized field surface dataset. Some typical geological structures are labelled, such as the seabed, a volcanic intrusion layer and a deep reflector. A target area is denoted by the red box. We show the RTM image of the target area in Figure 5.13 and the Marchenko image of the same area in Figure 5.14. Both images are produced with the same surface dataset that is discussed above and a same smooth velocity model (Figure 5.1a). These two images are comparable and consistent for the most parts - the positions of the reflectors and the phases of the reflectors in the shallow parts of the model match adequately. In Figure 5.13, green arrows indicate the ghost reflectors due to internal multiples and red arrows indicate the true subsurface reflectors. We interpret the reflectors indicted by the red arrows as real geologic reflectors because they are flat, continuous and consistent in both images. The dipping structures pointed by the green arrows are interpreted as multiple artifacts as these events destructively intersect with the real flat reflectors, causing discontinuities and cross-talks. These artificial dipping events are

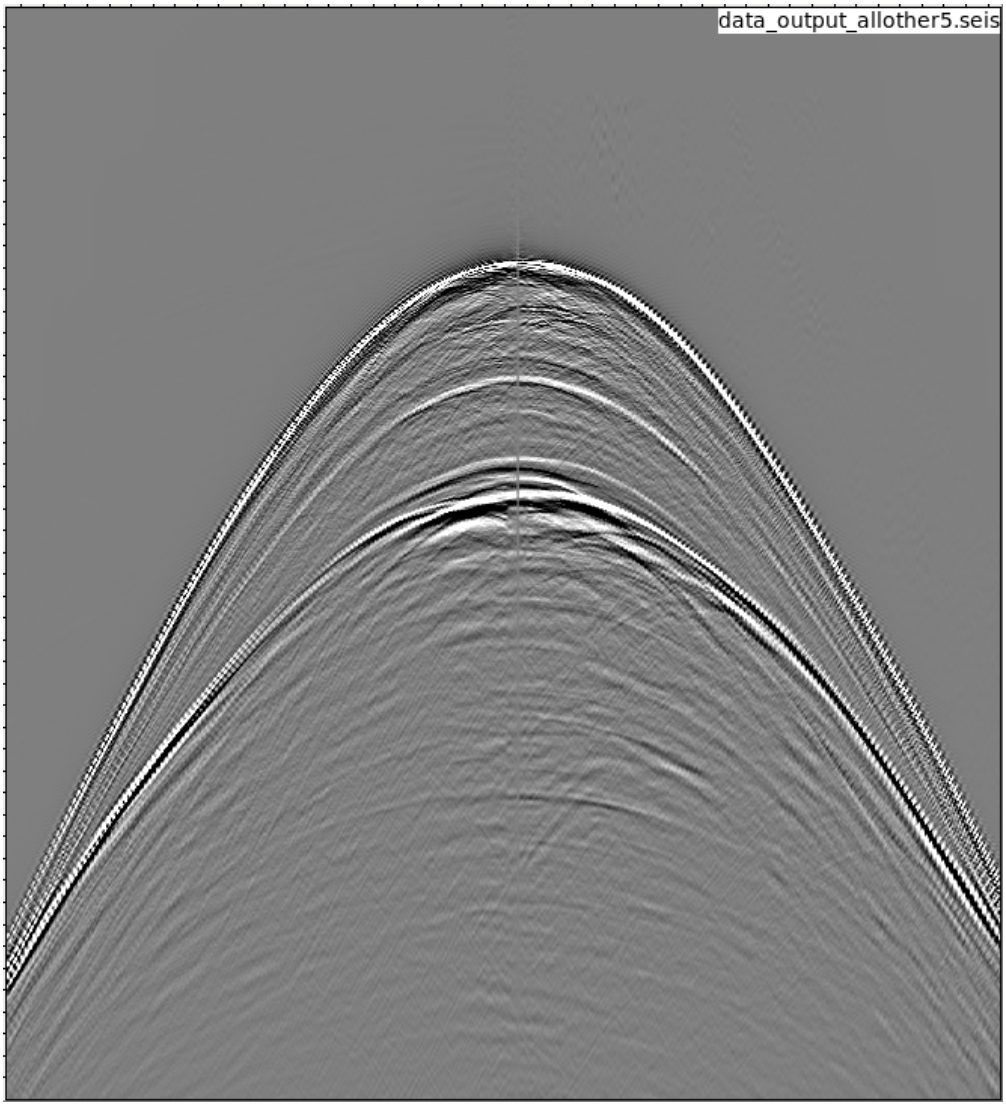

Figure 5.11: A 2-sided shot gather after data regularization with the work flow in Figure 5.10.

clearly eliminated in the Marchenko image in Figure 5.14. The blue arrow in Figure 5.13 points at another location where dipping artifacts caused by the internal multiples show in the RTM image. We also remove these artifacts in the Marchenko image (Figure 5.14).

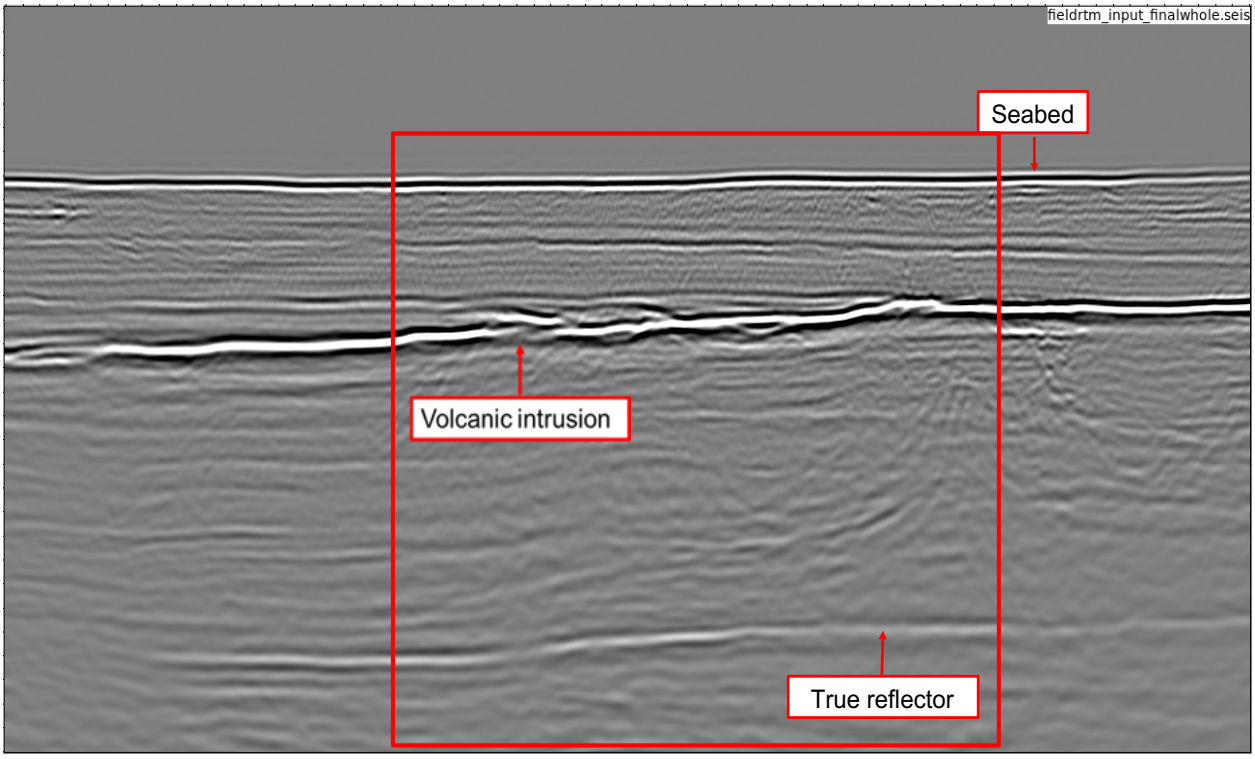

Figure 5.12: RTM image of the whole field. The red box denotes a target area that is compared with a Marchenko image.

5.6 Conclusions

We show the capacity of the Marchenko method for sub-basalt imaging with an offshore Brazil field dataset. In this field example, strong internal multiples are generated by the seabed and volcanic intrusions. Reverse Time Migration produces nonphysical interfaces due to the incorrect handling of these internal multiples. These artifacts are clearly attenuated in the image produced with Marchenko imaging. Meanwhile, we demonstrate the potential of the Marchenko method to reconstruct horizontally propagating waves and propose a practical workflow for the regularization and pre-processing of typical marine streamer data. Conventional internal multiple attenuation methods typically require accurate information

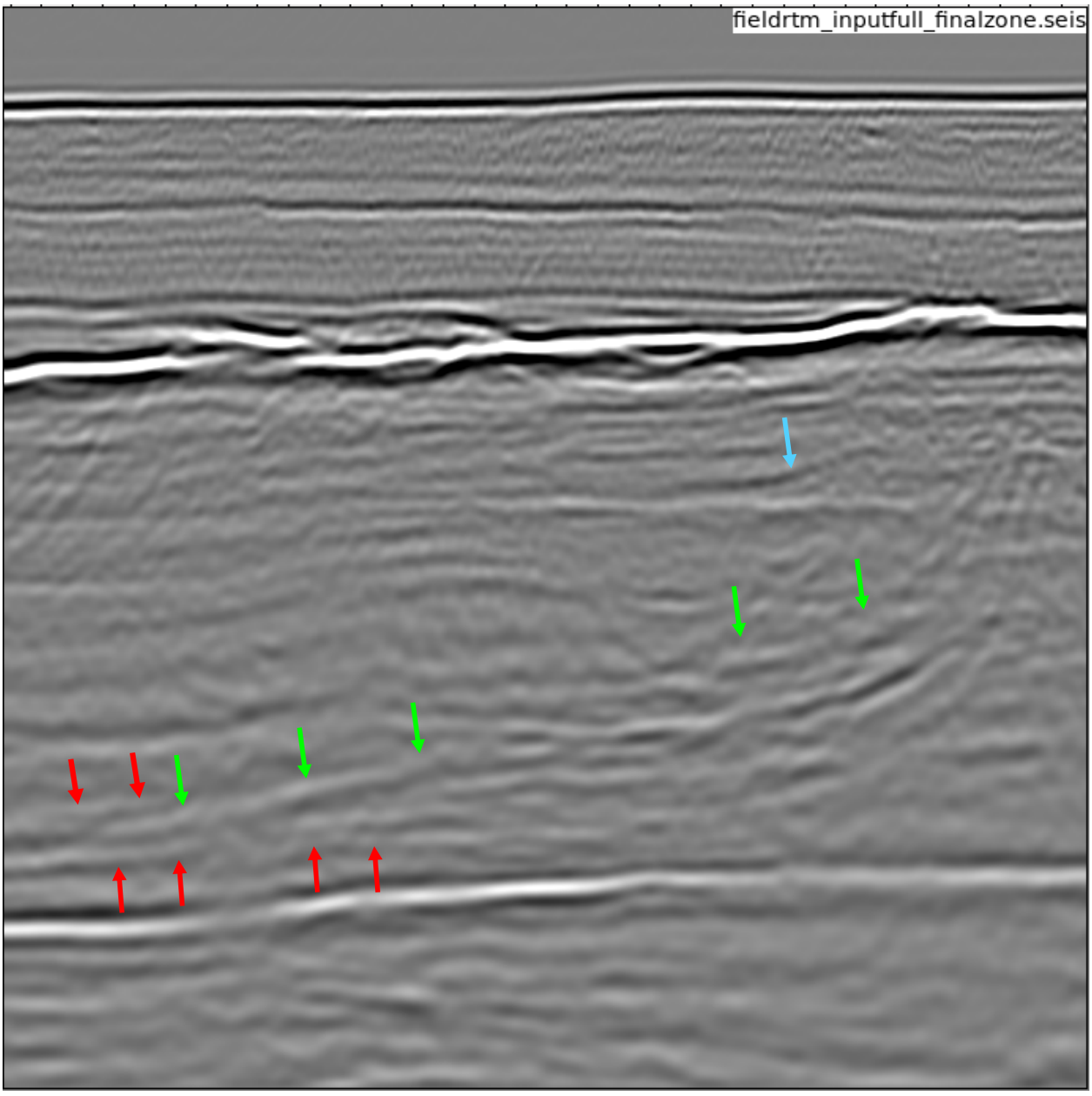

(a)

Figure 5.13: Field data RTM image inside the red box of Figure 5.12.

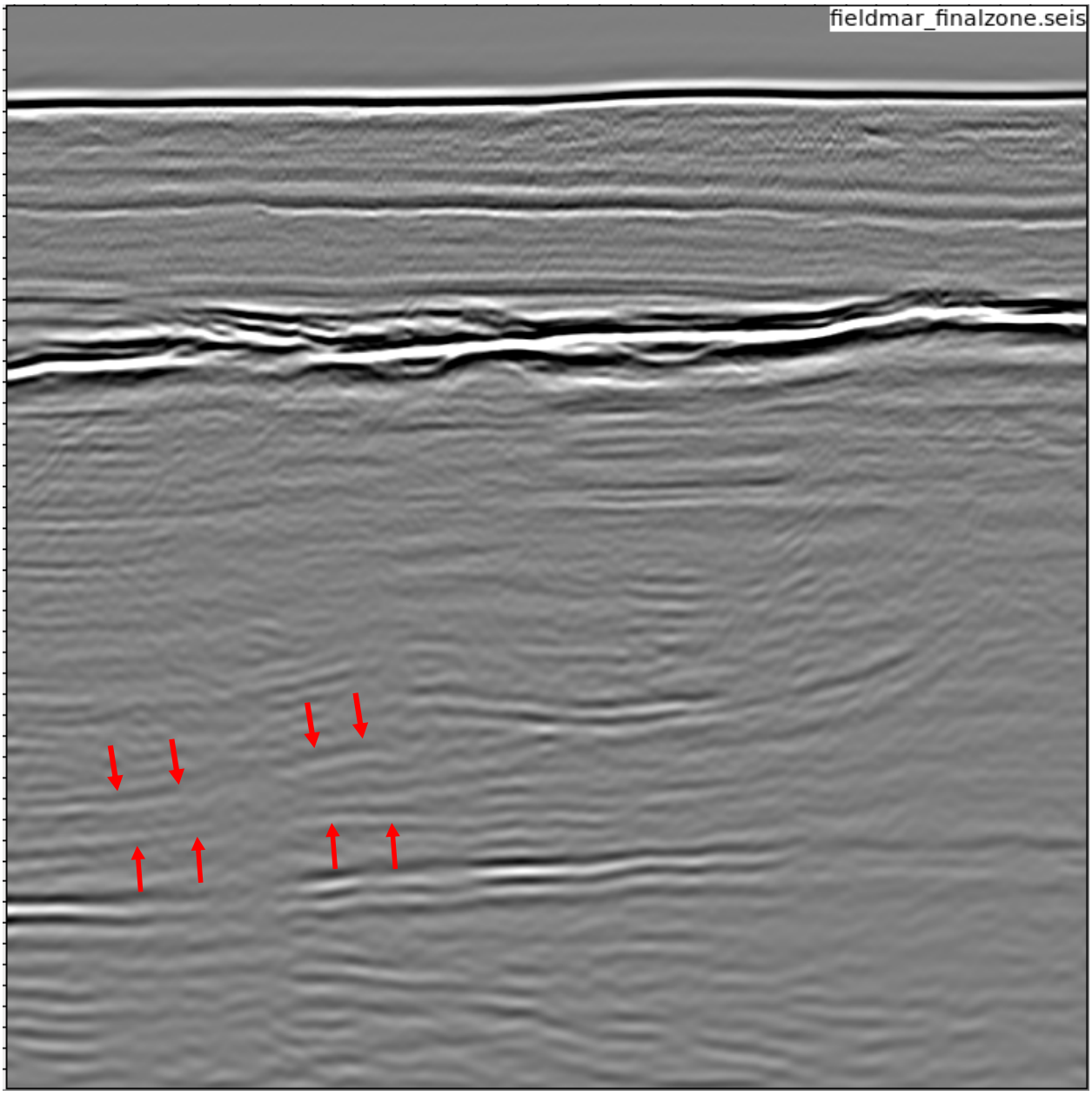

(a)

Figure 5.14: Field data Marchenko image inside the red box of Figure 5.12.

of multiple generators and eliminate internal multiples with an adaptive subtraction. Obtaining the horizons of multiple generators and subtracting the predicted multiples are both labor-intensive processes and often provide sub-optimal results when the primaries intervene with the internal multiples. With application to the offshore Brazil field data, we show that the Marchenko method works effectively for multiple-free imaging of complex sub-basalt structures without performing adaptive subtraction.

5.7 Acknowledgments

This work was supported by the Consortium Project on Seismic Inverse Methods for Complex Structures at the Colorado School of Mines. We are grateful to ExxonMobil for providing the field data. We thank Spectrum (now TGS) for giving the permission to show the data and WesternGeco for pre-processing the data.

CHAPTER 6

GENERAL CONCLUSIONS AND FUTURE RESEARCH

In this Chapter, I provide a brief and general conclusion to this dissertation and make recommendations for future research. Readers are referred to the individual conclusions in Chapters 2 through 6 for the specific conclusion associated with each chapter.

The most significant contribution of my dissertation to the field of seismic imaging is the development and implementation of the 2D and 3D Marchenko framework for field data applications. The Marchenko framework consists of 1) *Marchenko redatuming*, a method that creates virtual seismic wave forms that are generated by a point source in the subsurface and recorded at the surface, and 2) *Marchenko imaging*, a method that produces multiple-free seismic images using the redatumed seismic waves by Marchenko redatuming. I research on the practical aspects of this elegant theoretical framework and investigate how to make it applicable for the real seismic data.

I elucidate the specific requirements of the two inputs, surface reflection data and the background velocity model, needed by the Marchenko redatuming and imaging algorithms in **Chapter 3**. I show that Marchenko redatuming simply requires a smooth velocity model and this redatuming approach is robust with respect to errors in the velocity model. I emphasize that regularization and interpolation for the surface reflection data are the key to a successful implementation of Marchenko redatuming. I consider and compare several forward interpolation methods, demonstrating that for realistic acquisition geometries, forward interpolation methods are sufficiently accurate for 2D and 3D Marchenko redatuming. Modern seismic processing and imaging techniques benefit from utilizing 3D seismic data. In **Chapter 4**, I present an efficient 3D Marchenko redatuming numerical implementation, in which I resolve the associated computational optimization and memory issues. With the limited computational and data resources available in an academic environment, I cannot

fully demonstrate the potential for 3D Marchenko imaging to the extensive datasets that are currently acquired in the petroleum industry. I discuss future work along this path and make recommendations later in this chapter.

Internal multiples contaminate seismic images in two ways: by producing false negatives through destructively interfering with primaries or by creating false positives through focusing energy at nonphysical interfaces. In the first scenario, the destructive interference of internal multiples and primaries cause subsurface reflectors to be discontinuous or unsmooth in conventional seismic images. In **Chapter 2**, with a Gulf of Mexico field dataset, I show that the discontinuities caused by the destructive interference between internal multiples and primaries can be resolved by applying Marchenko imaging, where I produce a cleaner and more continuous image compared to the image produced by RTM for the same sub-salt area. In most cases, with conventional imaging methods, internal multiples are focused at nonphysical locations, generating artificial reflectors. The reduction of the nonphysical interfaces due to incorrectly handled multiples is my main focus in the data example using an offshore Brazil dataset. In **Chapter 5**, I show that Marchenko imaging is able to eliminate the nonphysical interfaces related to the strong internal multiples that are generated from basaltic intrusions in the overburden and produce a superior sub-basalt seismic image compared to the image produced by Reverse Time Migration.

6.1 Future research

There are a variety of directions for innovative open research under the Marchenko framework. Theoretical and methodological pathways include developing a model-free Marchenko method, updating velocity models for a localized or target subsurface area, time-lapse monitoring, and incorporating anisotropy and attenuation into the Marchenko framework. Some of these topics are discussed in the last chapters of the dissertations of Broggini (2013) and Singh (2016). In the following discussion, I focus on the practical challenges along the path of the field data application of the Marchenko framework and make recommendations accordingly for future research.

1 Application to the ocean bottom seismic data and the land seismic data

The use of ocean bottom seismic (OBS) data, including ocean bottom cables (OBC) data and ocean bottom nodes (OBN) data, generally has improved signal-to-noise ratios compared to streamer seismic data. Moreover, OBS acquisition technology provides multi-component data and offers more flexibility for the source-receiver geometry, allowing for the acquisition of data with full azimuth and/or longer offsets compared to the streamer data. To apply Marchenko imaging to OBS data, however, we need to undertake the problem that the sources and receivers are located at different depths. We can redatum the receivers of the OBS data to the acquisition surface. But since the Marchenko framework also involves redatuming, is it possible to modify the Marchenko algorithm and make it directly applicable to the OBS data? Another challenge with OBS data is that receivers are irregularly and sparsely distributed over a small area because of the expense of placing receivers on the ocean floor. Various techniques have been developed to overcome the sparsity problem associated with the recorded OBS data (Abma & Kabir, 2006; Berkhout & Verschuur, 2006; Curry & Shan, 2010; Ramírez & Weglein, 2009). Strategies for incorporating these interpolation methods with OBS data and produce the dense and regularized data required by Marchenko redatuming need further investigation.

Land seismic data processing and imaging increasingly attracts attention because of the rapid development of unconventional oil and gas exploration and production. Strong internal multiples are often generated by the complex near-surface heterogeneity from land seismic data. The land seismic data processing itself, however, faces several unique challenges, such as source signature related issues and severe and incoherent noise in the data. Other than the challenging issues of data regularization and source de-signature, near-surface heterogeneity, such as Karst stuctures, can be severe, which violates the up/down decomposition of the seismic wavefield that is used in current formulations of Marchenko imaging. How can we effectively resolve these problems for the land data application of the Marchenko method?

2 Selection of the calibration and stabilization parameters

We need to calibrate the amplitude surface reflection seismic data with an appropriate calibration parameter or scaling factor. The value of the calibration parameter is currently determined empirically. So is the stabilization parameter which is used in the calculation of multi-dimensional deconvolution. The value of the stabilization parameter not only affects the resolution of the image, but also plays a key role in determining the phase of the reflectors in Marchenko images. The phase information of the reflector is important for geologic interpretation, and interpreters demand the phases of the interfaces in seismic images produced with the Marchenko method to be consistent with the images produced with other conventional imaging approaches. Strategies for a automatic or systematical determination of the ad-hoc values for the calibration and stabilization parameters need further investigation.

3 Reduction of computational cost

Large 3D seismic data processing algorithms have become feasible thanks to the development of CPU and GPU clusters for high performance computing. Surface Related Multiple Elimination (SRME) with 3D field data has become a standard step in the seismic data processing work flow. The Marchenko redatuming algorithm involves similar computations as SRME, including trace-by-trace convolution and integration over a surface area. Marchenko redatuming, however, is performed in a iterative fashion, and approximately ten iterations are needed to ensure the convergence of the Marchenko redatuming algorithm for complex structures. The reduction of the computational cost of 3D Marchenko redatuming and imaging is an urgent issue to solve for commercializing the Marchenko method for hydrocarbon exploration. Avoiding redundant trace-by-trace convolution/cross-correlation during the retrieval of the Green's functions of adjacent subsurface points is one opportune direction.

4 Incorporation of horizontal propagating energy in Marchenko redatuming with two-way representation theorems

The Marchenko equations are derived using one-way representation theorems, which restrict the retrieval of the Green's function to the propagation paths that are not horizontal or

near horizontal. Two-way formulations of the representation theorems exist and can include horizontally propagating events (Wapenaar, 1996). The current one-way formulation of the Marchenko framework limits the ability of Marchenko imaging to resolve the internal multiple artifacts associated with steeply dipping interfaces. An ansatz to this problem would be incorporating horizontal propagating energy by re-deriving the Marchenko equations with two-way wavefields.

My PhD dissertation takes one of the first steps in the application of Marchenko imaging for complex subsurface structures with field data. I am dedicated to further address this problem in the future.

REFERENCES CITED

Abma, Ray, & Kabir, Nurul. 2006. 3D interpolation of irregular data with a POCS algorithm. *Geophysics*, **71**(6), E91–E97.

Bakulin, Andrey, & Calvert, Rodney. 2006. The virtual source method: Theory and case study. *Geophysics*, **71**(4), SI139–SI150.

Baysal, Edip, Kosloff, Dan D, & Sherwood, John WC. 1983. Reverse time migration. *Geophysics*, **48**(11), 1514–1524.

Behura, Jyoti, Wapenaar, Kees, & Snieder, Roel. 2014. Autofocus Imaging: Image reconstruction based on inverse scattering theory. *Geophysics*, **79**(3), A19–A26.

Berkhout, AJ, & Verschuur, DJ. 1997. Estimation of multiple scattering by iterative inversion, Part I: Theoretical considerations. *Geophysics*, **62**(5), 1586–1595.

Berkhout, AJ, & Verschuur, DJ. 2006. Imaging of multiple reflections. *Geophysics*, **71**(4), SI209–SI220.

Berryhill, John R. 1979. Wave equation datuming. *Geophysics*, **44**(8), 1329–1344.

Berryhill, John R. 1984. Wave equation datuming before stack. *Geophysics*, **49**(11), 2064–2066.

Beylkin, G. 1985. Imaging of discontinuities in the inverse scattering problem by inversion of a causal generalized Radon transform. *Journal of Mathematical Physics*, **26**(1), 99–108.

Bleistein, N, Stockwell, JW, & Cohen, JK. 2001. *Multidimensional Seismic Inversion*. Springer.

Bleistein, Norman. 1987. On the imaging of reflectors in the earth. *Geophysics*, **52**(7), 931–942.

Broggini, F, & Snieder, R. 2012. Connection of scattering principles: a visual and mathematical tour. *Eur. J. Phys.*, **33**, 593–613.

Broggini, Filippo. 2013. *Wave field autofocusing and applications to multidimensional deconvolution and imaging with internal multiples*. Ph.D. thesis, Colorado School of Mines.

Broggini, Filippo, Snieder, Roel, & Wapenaar, Kees. 2012. Focusing the wavefield inside an unknown 1D medium: Beyond seismic interferometry. *Geophysics*, **77**(5), A25–A28.

Broggini, Filippo, Wapenaar, Kees, van der Neut, Joost, & Snieder, Roel. 2014a. Data-driven Green's function retrieval and application to imaging with multidimensional deconvolution. *Journal of Geophysical Research: Solid Earth*, **119**(1), 425–441.

Broggini, Filippo, Snieder, Roel, & Wapenaar, Kees. 2014b. Data-driven wavefield focusing and imaging with multidimensional deconvolution: Numerical examples for reflection data with internal multiples. *Geophysics*, **79**(3), WA107–WA115.

Claerbout, Jon F. 1971. Toward a unified theory of reflector mapping. *Geophysics*, **36**(3), 467–481.

Curry, William, & Shan, Guojian. 2010. Interpolation of near offsets using multiples and prediction-error filters. *Geophysics*, **75**(6), WB153–WB164.

da Costa Filho, Carlos Alberto, Ravasi, Matteo, Curtis, Andrew, & Meles, Giovanni Angelo. 2014. Elastodynamic Green's function retrieval through single-sided Marchenko inverse scattering. *Physical Review E*, **90**(6), 063201.

da Costa Filho, Carlos Alberto, Ravasi, Matteo, & Curtis, Andrew. 2015. Elastic P-and S-wave autofocus imaging with primaries and internal multiples. *Geophysics*, **80**(5), S187–S202.

de Hoop, Adrianus T. 1988. Time-domain reciprocity theorems for acoustic wave fields in fluids with relaxation. *The Journal of the Acoustical Society of America*, **84**, 1877–1878.

Dragoset, Bill, Verschuur, Eric, Moore, Ian, & Bisley, Richard. 2010. A perspective on 3D surface-related multiple elimination. *Geophysics*, **75**(5), 75A245–75A261.

Dukalski, Marcin, & de Vos, Koos. 2017. Marchenko inversion in a strong scattering regime including surface-related multiples. *Geophysical Journal International*, **212**(2), 760–776.

Dukalski, Marcin, Mariani, Elisa, & de Vos, Koos. 2019. Handling short-period scattering using augmented Marchenko autofocusing. *Geophysical Journal International*, **216**(3), 2129–2133.

Etgen, John, Gray, Samuel H, & Zhang, Yu. 2009. An overview of depth imaging in exploration geophysics. *Geophysics*, **74**(6), WCA5–WCA17.

Fomel, Sergey. 1997. A variational formulation of the fast marching eikonal solver. *SEP-95: Stanford Exploration Project*, 127–147.

Fomel, Sergey. 2000. *Three-dimensional seismic data regularization.* Ph.D. thesis, Stanford University.

French, William S. 1975. Computer migration of oblique seismic reflection profiles. *Geophysics*, **40**(6), 961–980.

Guitton, Antoine, & Claerbout, Jon. 2015. Nonminimum phase deconvolution in the log domain: A sparse inversion approach. *Geophysics*, **80**(6), WD11–WD18.

Hale, Dave. 1991. Stable explicit depth extrapolation of seismic wavefields. *Geophysics*, **56**(11), 1770–1777.

Jakubowicz, Helmut. 1998. Wave equation prediction and removal of interbed multiples. *Pages 1527–1530 of: SEG Technical Program Expanded Abstracts 1998*. Society of Exploration Geophysicists.

Jia, Xueyi, Guitton, Antoine, Singh, Satyan, Snieder, Roelof, *et al.* . 2017. Subsalt Marchenko imaging: A gulf of mexico example. *In: 2017 SEG International Exposition and Annual Meeting*. Society of Exploration Geophysicists.

Jia, Xueyi, Guitton, Antoine, & Snieder, Roel. 2018. A practical implementation of subsalt Marchenko imaging with a Gulf of Mexico data set. *Geophysics*, **83**(5), S409–S419.

Kinneging, NA, Budejicky, V, Wapenaar, CPA, & Berkhout, AJ. 1989. Efficient 2d and 3d Shot Record Redatuming. *Geophysical Prospecting*, **37**(5), 493–530.

Krueger, J, Donno, D, Pereira, R, Mondini, D, Souza, A, Espinoza, J, & Khalil, A. 2018. Internal multiple attenuation for four presalt fields in the Santos Basin, Brazil. *Pages 4523–4527 of: SEG Technical Program Expanded Abstracts 2018*. Society of Exploration Geophysicists.

Marchenko, Vladimir Aleksandrovich. 1955. On reconstruction of the potential energy from phases of the scattered waves. *Pages 695–698 of: Dokl. Akad. Nauk SSSR*, vol. 104.

Matson, Ken H, & Abma, Ray. 2005. Fast 3D surface-related multiple elimination using azimuth moveout for multiples. *Pages 2064–2067 of: SEG Technical Program Expanded Abstracts 2005*. Society of Exploration Geophysicists.

McMechan, George A. 1983. Migration by extrapolation of time-dependent boundary values. *Geophysical Prospecting*, **31**(3), 413–420.

Meles, Giovanni Angelo, Löer, Katrin, Ravasi, Matteo, Curtis, Andrew, & da Costa Filho, Carlos Alberto. 2014. Internal multiple prediction and removal using Marchenko autofocusing and seismic interferometry. *Geophysics*, **80**(1), A7–A11.

Mildner, Constantin, Becker, Theodor S, de Vos, Koos, Broggini, Filippo, & Robertsson, Johan OA. 2017. Source wavelet estimation using Marchenko focusing functions: Theory and laboratory data example. *Pages 5521–5525 of: SEG Technical Program Expanded Abstracts 2017*. Society of Exploration Geophysicists.

Operto, M Stephane, Xu, Sheng, & Lambaré, Gilles. 2000. Can we quantitatively image complex structures with rays? *Geophysics*, **65**(4), 1223–1238.

Ramírez, Adriana Citlali, & Weglein, Arthur B. 2009. Green's theorem as a comprehensive framework for data reconstruction, regularization, wavefield separation, seismic interferometry, and wavelet estimation: A tutorial. *Geophysics*, **74**(6), W35–W62.

Ravasi, Matteo. 2017. Rayleigh-Marchenko redatuming for target-oriented, true-amplitude imaging. *Geophysics*, **82**(6), S439–S452.

Ravasi, Matteo. 2019 (Apr. 4). *A method of redatuming geophysical data*. US Patent App. 16/084,660.

Ravasi, Matteo, Vasconcelos, Ivan, Kritski, Alexander, Curtis, Andrew, Filho, Carlos Alberto da Costa, & Meles, Giovanni Angelo. 2016. Target-oriented Marchenko imaging of a North Sea field. *Geophysical Journal International*, **205**(1), 99–104.

Rose, James H. 2001. 'Single-sided' focusing of the time-dependent Schrödinger equation. *Physical Review A*, **65**(1), 012707.

Rose, James H. 2002. 'Single-sided' autofocusing of sound in layered materials. *Inverse problems*, **18**(6), 1923–1934.

Sava, Paul, & Hill, Stephen J. 2009. Overview and classification of wavefield seismic imaging methods. *The Leading Edge*, **28**(2), 170–183.

Schneider, William A. 1978. Integral formulation for migration in two and three dimensions. *Geophysics*, **43**(1), 49–76.

Singh, Satyan. 2016. *An inverse scattering approach to imaging using Marchenko equations in the presence of a free surface*. Colorado School of Mines.

Singh, Satyan, & Snieder, Roel. 2017. Strategies for imaging with Marchenko-retrieved Green's functions. *Geophysics*, **82**(4), Q23–Q37.

Singh, Satyan, Snieder, Roel, Behura, Jyoti, van der Neut, Joost, Wapenaar, Kees, & Slob, Evert. 2015a. Marchenko imaging: Imaging with primaries, internal multiples, and free-surface multiples. *Geophysics*, **80**(5), S165–S174.

Singh, Satyan, Snieder, Roel, Behura, Jyoti, van der Neut, Joost, Wapenaar, Kees, & Slob, Evert. 2015b. Marchenko imaging: Imaging with primaries, internal multiples, and free-surface multiples. *Geophysics*, **80**(5), S165–S174.

Singh, Satyan, Snieder, Roel, van der Neut, Joost, Thorbecke, Jan, Slob, Evert, & Wapenaar, Kees. 2016a. Accounting for free-surface multiples in Marchenko imaging. *Geophysics*, **82**(1), R19–R30.

Singh, Satyan, Snieder, Roel, van der Neut, Joost, Thorbecke, Jan, Slob, Evert, & Wapenaar, Kees. 2016b. Accounting for free-surface multiples in Marchenko imaging. *Geophysics*, **82**(1), R19–R30.

Slob, EC, & Wapenaar, Kees. 2017. Theory for Marchenko imaging of marine seismic data with free surface multiple elimination. *In: 79th EAGE Conference and Exhibition 2017*.

Snieder, Roel, Wapenaar, Kees, & Larner, Ken. 2006. Spurious multiples in seismic interferometry of primaries. *Geophysics*, **71**(4), SI111–SI124.

Spetzler, J., & Snieder, R. 2004. The Fresnel volume and transmitted waves. *Geophysics*, **69**, 653–663.

Staring, Myrna, Pereira, Roberto, Douma, Huub, van der Neut, Joost, & Wapenaar, Cornelis. 2017. Adaptive double-focusing method for source-receiver Marchenko redatuming on field data. *Pages 4808–4812 of: SEG Technical Program Expanded Abstracts 2017*. Society of Exploration Geophysicists.

Tikhonov, Andrei Nikolaevich, Goncharsky, AV, Stepanov, VV, & Yagola, Anatoly G. 2013. *Numerical methods for the solution of ill-posed problems*. Vol. 328. Springer Science & Business Media.

Unser, Michael. 1999. Splines: A perfect fit for signal and image processing. *IEEE Signal processing magazine*, **16**(6), 22–38.

van der Neut, Joost, Thorbecke, Jan, Mehta, Kurang, Slob, Evert, & Wapenaar, Kees. 2011. Controlled-source interferometric redatuming by crosscorrelation and multidimensional deconvolution in elastic media. *Geophysics*, **76**(4), SA63–SA76.

van der Neut, Joost, Vasconcelos, Ivan, & Wapenaar, Kees. 2015a. On Green's function retrieval by iterative substitution of the coupled Marchenko equations. *Geophysical Journal International*, **203**(2), 792–813.

van der Neut, Joost, Wapenaar, Kees, Thorbecke, Jan, & Slob, Evert. 2015b. Practical challenges in adaptive Marchenko imaging. *Pages 4505–4509 of: SEG Technical Program Expanded Abstracts 2015*. Society of Exploration Geophysicists.

Vasconcelos, I, & van der Neut, J. 2016. Full-wavefield Redatuming of Perturbed Fields with the Marchenko Method. *In: 78th EAGE Conference and Exhibition 2016*.

Vasconcelos, Ivan, Snieder, Roel, & Douma, Huub. 2009. Representation theorems and Green's function retrieval for scattering in acoustic media. *Physical Review E*, **80**(3), 036605.

Vasconcelos, Ivan, Wapenaar, Kees, van der Neut, Joost, Thomson, Colin, & Ravasi, Matteo. 2015. Using inverse transmission matrices for Marchenko redatuming in highly complex media. *Pages 5081–5086 of: SEG Technical Program Expanded Abstracts 2015*. Society of Exploration Geophysicists.

Verschuur, Dirk Jacob. 1991. *Surface-related multiple elimination, an inversion approach*. Ph.D. thesis, Delft University of Technology.

Wapenaar, Cornelis, & Slob, Evert. 2017. Time-lapse data prediction by Marchenko-based reservoir transplantation. *Pages 5583–5587 of: SEG Technical Program Expanded Abstracts 2017*. Society of Exploration Geophysicists.

Wapenaar, CPA. 1996. Reciprocity theorems for two-way and one-way wave vectors: A comparison. *The Journal of the Acoustical Society of America*, **100**(6), 3508–3518.

Wapenaar, Kees. 2014. Single-sided Marchenko focusing of compressional and shear waves. *Physical Review E*, **90**(6), 063202.

Wapenaar, Kees, Thorbecke, Jan, & Draganov, Deyan. 2004. Relations between reflection and transmission responses of three-dimensional inhomogeneous media. *Geophysical Journal International*, **156**(2), 179–194.

Wapenaar, Kees, Thorbecke, Jan, van der Neut, Joost, Slob, Evert, Broggini, Filippo, Behura, Jyoti, Snieder, Roel, *et al.* . 2012. Integrated migration and internal multiple elimination. *In: 2012 SEG Annual Meeting*. Society of Exploration Geophysicists.

Wapenaar, Kees, Thorbecke, Jan, van der Neut, Joost, Broggini, Filippo, Slob, Evert, & Snieder, Roel. 2014a. Green's function retrieval from reflection data, in absence of a receiver at the virtual source position. *The Journal of the Acoustical Society of America*, **135**(5), 2847–2861.

Wapenaar, Kees, Thorbecke, Jan, van der Neut, Joost, Broggini, Filippo, Slob, Evert, & Snieder, Roel. 2014b. Marchenko imaging. *Geophysics*, **79**(3), WA39–WA57.

Wapenaar, Kees, van der Neut, Joost, & Slob, Evert. 2016. On the role of multiples in Marchenko imaging. *Geophysics*, **82**(1), A1–A5.

Whitmore, N Dan. 1983. Iterative depth migration by backward time propagation. *Pages 382–385 of: SEG Technical Program Expanded Abstracts 1983*. Society of Exploration Geophysicists.

Wilkinson, Keith, & Bale, Richard. 2014. Predicting Free Surface Multiples without the Water: SRME on Land. *GeoConvention, Expanded Abstracts*.

Zhang, Lele, & Staring, Myrna. 2018. Marchenko scheme based internal multiple reflection elimination in acoustic wavefield. *Journal of Applied Geophysics*, **159**, 429–433.

Zhang, Yu, Zhang, Guanquan, & Bleistein, Norman. 2005. Theory of true-amplitude one-way wave equations and true-amplitude common-shot migration. *Geophysics*, **70**(4), E1–E10.

Ziolkowski, Anton, Hanssen, Peter, Gatliff, Robert, Jakubowicz, Helmut, Dobson, Andrew, Hampson, Gary, Li, Xiang-Yang, & Liu, Enru. 2003. Use of low frequencies for sub-basalt imaging. *Geophysical Prospecting*, **51**(3), 169–182.